# Stability of an Australian inverse bay

ULF GRÄWE[1], JOACHIM RIBBE[2], JÖRG-OLAF WOLFF[1]

1. Institute for Chemistry and Biology of the Marine Environment,
Carl von Ossietzky University Oldenburg,
Carl-von-Ossietzky-Straße 9–11, 26111 Oldenburg, Germany
email: graewe@icbm.de, wolff@icbm.de

2. University of Southern Queensland, Toowoomba 4350, Queensland, Australia
email: joachim.ribbe@usq.edu.au

*Keywords: inverse estuary, hypersalinity, gravity currents, plumes*

## ABSTRACT

Hervey Bay, a large coastal embayment situated off the central eastern coast of Australia, is a shallow tidal area (average depth 15 m), close to the continental shelf. It shows features of an inverse estuary, due to the high evaporation rate (approximately 2 m $yr^{-1}$), low precipitation (less than 1 m $yr^{-1}$) and on average almost no freshwater inputs from the three rivers that drain into the bay.

We applied an ocean general circulation model to compute the temperature, density and salinity distribution within the bay and surroundings. The numerical studies are performed with the COupled Hydrodynamical Ecological model for REgioNal Shelf seas (COHERENS). A model validation and calibration was carried out after recent field campaigns.

The investigations showed that the bay is almost vertically well mixed throughout the year and that the horizontal distribution of properties follows the bathymetry. As in other inverse/negative estuaries, the year-round salinity increases toward the shore to form a nearly persistent salinity gradient. This leads especially in the transition from summer to autumn to the formation of dense water mass thereby establishing gravity currents. The high saline water can sink beyond 200 m, flow over the continental shelf to form a 'Hervey Bay' water mass that is advected with the East Australian Current. The investigation further showed that air temperature, wind direction and tidal regime are mainly responsible for the stability of the inverse circulation and strength of the salinity gradient across the bay.

## Introduction

In subtropical climates where evaporation is likely to exceed the supply of freshwater from precipitation and river run-off, large coastal bays, estuaries and near shore coastal environments are often characterized by inverse circulations and hypersalinity zones (Tomczak and Godfrey, 2003). An inverse circulation is characterized by sub-surface flow of saline water away from a zone of hypersalinity towards the open ocean. This flow takes place beneath a layer of inflowing oceanic water and leads to salt injections into the ocean (Brink and Shearman, 2006). Examples for such seas include the Gulf of California (Lavin et al., 1998), Spencer Gulf (Lennon et al., 1987) and the Ria of Pontevedra (deCastro et al., 2004). Due to high evaporation during summer, the accumulation of salt in the head water of these inverse bays/estuaries and atmospheric cooling in the transition to autumn/winter, these water masses can become gravitationally unstable and form gravity current flows.

In this study, we investigate how sub-surface flow of saline water is formed and how stable these inverse flows are in a subtropical east Australian coastal bay. The study utilizes recent hydrographic observations from Hervey Bay (Figure 1) and a coastal ocean general circulation model.

The coastal bay is shown to be dominated by an inverse circulation and recent changes in climate are associated with changes in the physical properties of the bay. Hypersalinity is a persistent feature and is more frequent in the last decade due to climate changes. Climate in the region is subtropical with most precipitation occurring during the southern hemisphere summer.

Hervey Bay is a large coastal bay off the subtropical east coast of eastern Australia and situated at the southern end of the Great Barrier Reef to the south of the geographic definition of the Tropic of Capricorn (23.5°S). Fraser Island separates the bay in the east from the Pacific Ocean. It covers an area of about 4000 km$^2$. Mean depth is about 15 m, with depths increasing northward to more than 40 m, where the bay is connected to the open ocean via an approximately 75-km wide gap. A narrow and shallow (<2 m) channel connects the bay to the ocean in the south. In the East/Northeast the continental shelf has an average width of 40 km. At the eastern shelf edge the East Australian Current (EAC) reattaches to the shelf to follow now the coastline to the south. In interesting feature of Hervey Bay is that its width to length ratio is nearly 1, whereas for example for Spencer Gulf, Gulf of California and Ria of Pontevedra this ratio is smaller than ⅓.

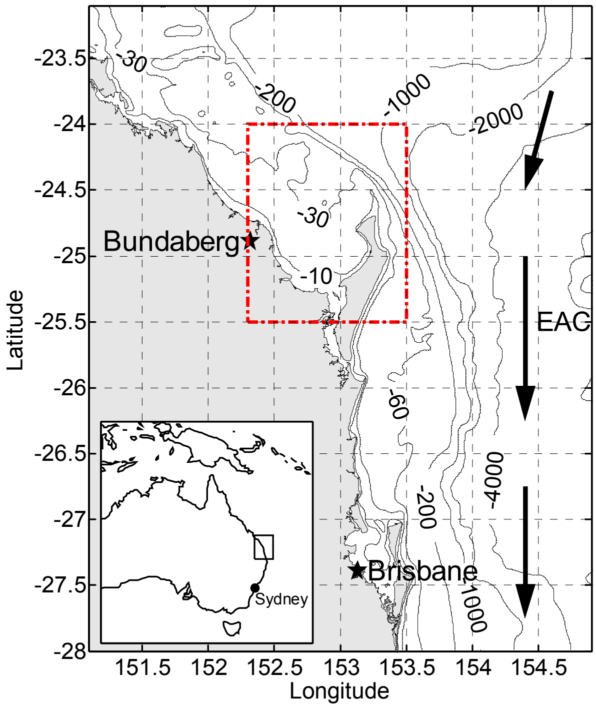


Figure 1. Topography of Hervey Bay. The region of interest is indicated by the red box. The position of the EAC is schematically given by the arrows.

## The model

This study utilizes the ocean model COHERENS (Luyten et al., 1999) which uses bottom following sigma coordinates and employs the hydrostatic version of the Navier-Stokes equations. The model is run in a prognostic mode with spherical coordinates and 18 vertical levels. The model domain is resolved with a rectangular grid of 90 × 140 grid points. The mesh size varies and increases from 2.5 km within Hervey Bay to 7 km near the boundaries of the model domain. The maximum depth within the model domain is limited to 900 m in order to increase the maximum allowable time step to 16 s and 420 s for the barotropic and baroclinic modes respectively. Three-hourly measurements of atmospheric variables and river flows are prescribed along the boundaries. A quadratic bulk formula is used to calculate surface frictional stresses with a wind-dependent formulation of the drag coefficient (Geernaert et al., 1986). Conventional bulk formulae are used to derive local evaporation rates and residual surface heat fluxes from shortwave and longwave radiation as well as sensible and latent heat fluxes. Turbulent exchange coefficients for latent and sensible heat are assumed to be functions of both wind speed and the air-sea temperature differences. The surface salt (freshwater) flux is a function of sea surface salinity, and the difference between evaporation and precipitation rates. Vertical turbulence is parameterized using the $k$-$\varepsilon$ closure scheme. The horizontal turbulent exchange coefficient is taken proportional to the product of lateral grid spacing and the shear velocity (the Smagorinsky-scheme). These are standard configurations provided with COHERENS. For further details of numerical techniques employed see Luyten et al. (1999). Amplitudes and phases of the five major tidal constituents ($M_2$, $S_2$, $N_2$, $K_1$ and $O_1$) are prescribed along the open boundaries. A quadratic bottom drag formula at the seafloor is used with a bottom roughness length of $z_0 = 0.001$ m. At the open-ocean boundary, we prescribe profiles of temperature and salinity that are derived from the one-dimensional model GOTM (General Ocean Turbulence Model, see e.g., Umlauf and Burchard, 2005, and references therein). GOTM is forced by observed meteorological conditions. The numerical calculations are then relaxed towards available hydrographic observations from automatic floats (ARGOS) or ships. The open ocean boundary conditions are updated every second day. The EAC is implemented by a simple sea surface gradient. To initialize the model we use a spin-up of two years (1988–1990), starting from rest with climatological profiles for salinity and temperature. The numerical experiments analyzed for this study cover the period 1990–2007.

## Results and discussion

Hydrographic observations, made during three one-week field trips into the bay in September 2004 (Ribbe, 2006), August and December 2007. The simulated temperature and salinity distribution within Hervey Bay is consistent with the observations during all three field surveys (Figure 2). The simulations reveal that the bay is in parts vertically well mixed throughout most of the year and therefore, only the depth averaged salinity distribution is considered here for model validation. The model reproduces the salinity gradient with salinity decreasing in all three field trips from the southwest coast towards the northern opening of the Bay (Figure 2).

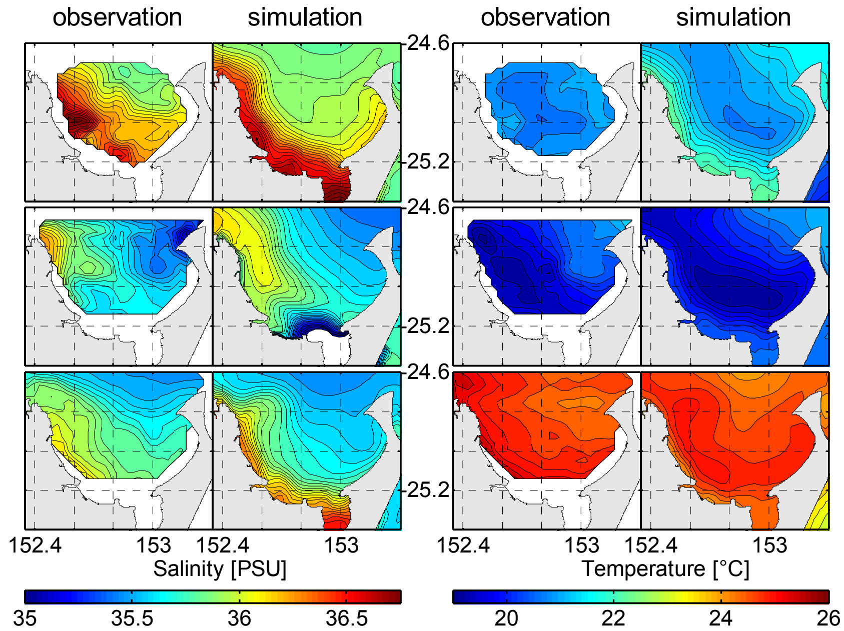


Figure 2. Comparison of the modeled and measured depth averaged salinity (left) and temperature (right) distribution during September 2004 (top), August 2007 (middle) and December 2007 (bottom).

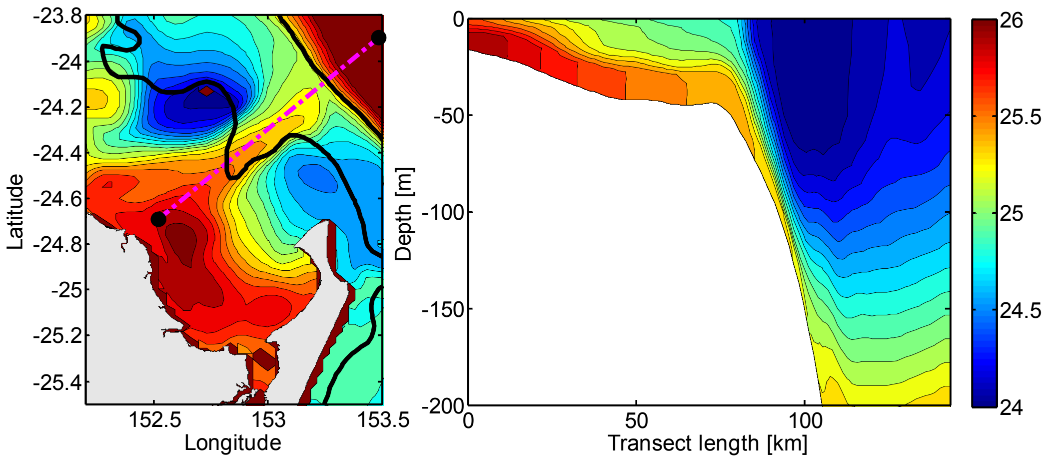


Figure 3. Bottom density $\sigma_t$ (left) at 1 August 2003, position of the cross section (magenta dashed line) and depth contours at 20 and 200 m. Right: Cross sections along the indicated transect.

The comparison with the first survey shows that the salinity gradient is less sharp than indicated by the model. But in general the agreement of the model output and the measurements from each of the field trips is quite well. The model confirms that the coastal region is occupied by a zone of hypersalinity with salinities well above 36 psu. The model seems to overestimate the temperature in the near shore region, but both observations and simulated data show a similar pattern. The distribution of temperature is well matched by the model for both subsequent field trips. For further validation of the model performance, we compute the daily bay averaged SST for both model and Advanced Very High Resolution Radiometer (AVHRR) sea surface temperature (SST) data from 1999–2005. The two indices are highly correlated with a correlation coefficient exceeding 0.9 and a nearly vanishing bias. Encouraged by the good model performance in simulating the physics and hydrodynamics of Hervey Bay we applied the model to investigate the stability of the hypersalinity zone and how gravity currents are formed.

As one can see in Figure 2 the temperature distribution, for all three field trips, is nearly homogeneous. The model also confirms that the bay is almost vertically well mixed throughout the year. This can be explained by the tidal regime of Hervey Bay. The tidal amplitude within the bay can be higher than 1.75 m. The tidally induced bottom Ekman boundary layer in the bay and on the northern shelf is most of the time larger than the water depth. Therefore the tidally induced mixing is quite efficient and stratification is suppressed. Only the salinity can establish nearly permanent frontal behavior due to high evaporation rates (approximately 2 m $yr^{-1}$). If one translates this into density, on the western shore of the bay the water is heavier (denser) than close to the open ocean and this can lead to the formation of gravity currents and bottom flow of dense water towards the ocean. A second factor that stabilizes the hypersalinity zone is the wind. The main wind direction is southeast (trade winds) with a strength of 7 m $s^{-1}$. The wind induced current flows along the western shore and advects the coastal water northwestwards (Ribbe et al., 2008). Because the wind induced currents are with strength of 0.25 m $s^{-1}$ a factor of 3–5 larger than possible gravity currents, there is a net transport of hypersaline water parallel to the shore. Even if the hypersalinity zone is gravitational unstable, this feature is persistent due to wind induced transport. Only during a fortnightly modulation of the tide by a spring/neap tidal cycle, where tidal amplitudes drop down to 0.4 m, stratification can be established. Secondly winds from the north/northeast (typical during late autumn) lead to a reversal in the wind induced currents. Now the water is advected southward close to the western shore and leaves Hervey Bay at the central part of the bay. And third during autumn the water cools down and increases the density gradient across the bay. Only the combination of these three factors can establish significant gravity currents. These happen nearly every year once or twice during late summer/autumn. Such an outflow event is shown in Figure 3 (left). One can see that the outflowing water reaches a depth of 200 m. Also visible is that after the water reached depths greater than 100 m, it leaves the friction dominated region and the Corriolis force becomes effective and deflects the plume towards the left. By looking onto the cross section one sees that the plume has in the upper part a thickness of 10–20 m and becomes thinner during its way down the slope. The gravity current can reach a maximum speed of 0.15 m $s^{-1}$. If one estimates the width of the plume with 20 km and the height with 15 m, some simple calculations, based on volume conservation, give a rough estimate of 20 days, in which Hervey Bay is completely flushed. The numerical experiments showed that these gravity currents have only duration of less than 10 days. But this is understandable because extrusion out of the plume, interfacial friction and also increasing tidal energy weakens the gravity current and also part of the dense water mass leaves the bay northwestwards on its western shore.

## Conclusions

The results presented here have shown how Hervey Bay, a large coastal embayment situated off the central eastern coast of Australia, that shows features of an inverse estuary, can loose its stability to form gravity currents. During summer, high evaporation rates lead to a hypersalinity zone close to the shore combined with a density higher than in the surrounding coastal area. The combination of accumulation of salt, atmospheric cooling and a strong spring/neap tidal cycle can trigger these flows. The gravity current speed is in the order of 0.1 m $s^{-1}$ and can lead to a complete flushing of Hervey Bay. These flushings occur nearly every autumn and have an average duration of 10 days. These gravitational instabilities lead to an exchange of water between Hervey Bay and the continental shelf.

## References


Brink, K.H., Shearman, R. K. (2006), Bottom boundary layer flow and salt injection from the continental shelf to slope, *Geophysical Research Letters*, 33, L13608.

deCastro, M., Gomez-Gesteira, M., Alvarez, I., Prego, R. (2004), Negative estuarine circulation in the Ria of Pontevedra (NW Spain), *Estuarine, Coastal and Shelf Science*, 60, 301–312.

Geernaert, G.L., Katsaros, K.B., Richter, K. (1986), Variation of the drag coefficient and its dependence on sea state, *Journal of Geophysical Research*, 91, 7667–7679.

Lavin, M.R., Godinez, V.M., Alvarez, L.G. (1998), Inverse-estuarine Features of the Upper Gulf of California, *Estuarine, Coastal and Shelf Science*, 47, 769–795.

Luyten, P.J., Jones, J.E., Proctor, R., Tabor, A., Tett, P., Wild-Allen, K. (1999), *COHERENS – A coupled hydrodynamical-ecological model for regional and shelf seas: user documentation*, MUMM Rep., Management Unit of the Mathematical Models of the North Sea.

Nunes Vaz, R.A., Lennon, G.W., Bowers, D.G. (1990), Physical behaviour of a large, negative or inverse estuary, *Continental Shelf Research*, 10, 277–304.

Ribbe, J. (2006), A study into the export of saline water from Hervey Bay, Australia, *Estuarine, Coastal and Shelf Science*, 66, 550–558.

Ribbe, J., Wolff, J.-O., Staneva, J., Gräwe, U. 2008, Assessing Water Renewal Time Scales for Marine Environments from Three-Dimensional Modelling: A Case Study for Hervey Bay, Australia, *Environmental Modelling and Software*. (In Press.)

Tomczak, M., Godfrey, S. (2003), *Regional Oceanography: an Introduction*. 2nd edition. Daya Publishing House, Delhi, 390pp.

Umlauf, L., Burchard, H. (2005), Second-order turbulence closure models for geophysical boundary layers. A review of recent work, *Continental Shelf Research*, 25, 795–827.

# Reconstruction of the hydrodynamics in a tropical mangrove estuary

PETER HOLTERMANN[1], HANS BURCHARD[1], TIM JENNERJAHN[2]

1. Baltic Sea Research Institute Warmemünde, Seestraße 15,
   18119 Rostock-Warnemünde, Germany
   email: peter.holtermann@io-warnemuende.de, hans.burchard@io-warnemuende.de

2. Leibniz Centre for Tropical Marine Ecology, Fahrenheitstraße 6,
   28359 Bremen, Germany
   email: tim.jennerjahn@zmt-bremen.de

*Keywords: mangroves, oceanic modeling, hydrodynamics, ADCP*

## ABSTRACT

The Segara Anakan Lagoon is situated at the southern coast of Central Java and is one of the last large mangrove fringed estuarine systems left on Java. During the past 25 years it was subject to strong anthropogenic transformations. The lagoon consists of a body of water in the west and a second in the east. Each of them let out into the ocean. Narrow and deep channels run through the mangrove flats creating a connection between the water bodies. The hydrodynamics of the lagoon are based upon the semi-diurnal tide and the freshwater discharge of several rivers entering the lagoon. The Citanduy River, located in the western part, is responsible for more than three quarters of the freshwater discharge. There are no recent studies of the lagoons hydrodynamics. This work aims to reconstruct the hydrodynamics based upon field measurements, satellite data and a three-dimensional numerical modeling study (GETM). The in situ data were collected in two field trips, one during the dry season and the second during the end of the rainy season.

The estuary is well-mixed. The model demonstrates that the exchange between the two basins is only a small fraction of the direct exchange with the ocean. This result is confirmed by ADCP water volume flux measurements. Net water volume transports between the two parts of the lagoon depend on the Citanduy River freshwater runoff. An implemented sea-water age tracer shows different flushing times between the monsoon seasons as well as spatial differences inside the lagoon. The mean salinity differences between the wet and dry seasons are in the order of 8 g kg$^{-1}$ for the western part and 4 g kg$^{-1}$ for the eastern part.

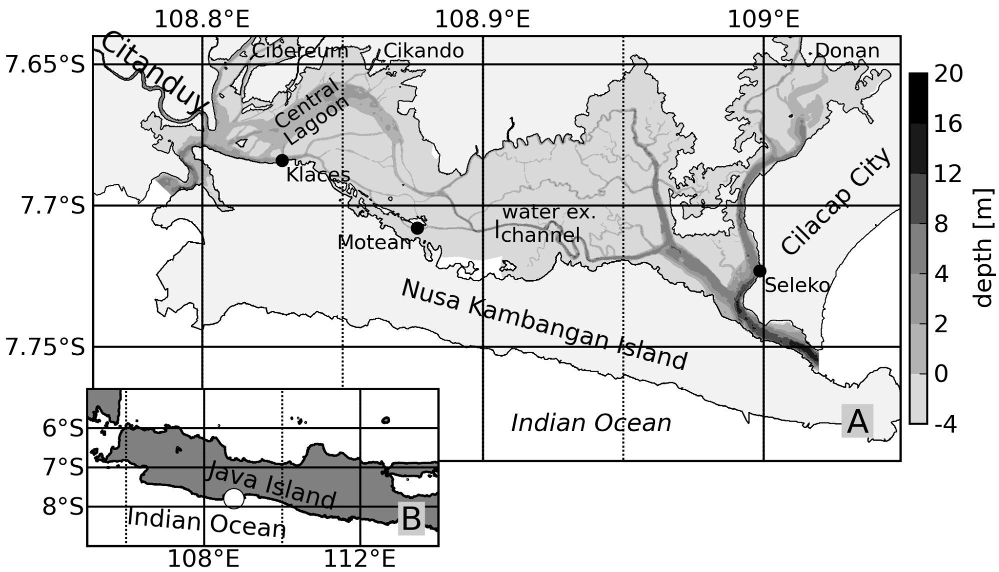


Figure 1. Bathymetry and location of the Segara Anakan lagoon (depths are referenced to the mean sea level). The central lagoon, the main water body of the western part, has a depth of 1–3 m. The western outlet is on average 5 m deep. The eastern part with the navigation channels has depths of more than 10 m near to the outlet. Three quarters of the lagoons area are mangroves (light gray).

## Introduction

The mangrove fringed Segara Anakan lagoon is semi-enclosed by the Nusa Kambangan Island with two outlets to the Indian Ocean, see Figure 1. It covers an overall area of about 120 $km^2$. Three quarters of the lagoons area are mangroves; the remaining quarter is covered by water. The ocean tide is semidiurnal with a spring tide range of 1.4 m and a neap tide range of 0.4 m. The lagoon can be divided into two major water bodies mainly connected via a single channel (water exchange channel). The first is the western part and central part with a substantial freshwater input from the Citanduy River. The second is the eastern water body having a freshwater input two orders of magnitude less than the Citanduy. Each of the parts has a direct connection to the ocean. The climate is tropical humid and governed by the monsoons with most of the rainfalls during November–March. In the last century inputs from sediment-laden rivers mainly the Citanduy caused a dramatic change of the land- and water-covered area. Furthermore, ongoing urbanization accompanied by an increased input of nutrients and pollutants harms the health of the ecosystem (Yuwono, 2007). The last the known study of the hydrodynamics was done by White et al. (1989) but substantial morphology changes between 1989 and 2005 together with a continuing trend of the land-water change motivated a new survey of the Segara Anakan lagoon hydrodynamics.

In this talk results of field measurements carried out in the years 2005 and 2006 and their reproduction with a three-dimensional numerical model of the lagoon are presented.

Two field trips were carried out in Segara Anakan with a focus onto the western and central parts. Dates were chosen to obtain data at different monsoon seasons.

August-September 2005 (dry season)
February-March 2006 (end of rainy season)

An RDI Workhorse-Sentinel 1200 kHz ADCP was used to quantify the water volume fluxes inside the lagoon and the exchange rates with the ocean. Furthermore a bathymetry survey was made at the beginning of the first field trip. Temperature and salinity measurements were taken manually with a WTW Multiline P4 multimeter. A Seabird SBE16 CT-recorder was available during the second field trip. Tide stations were installed in villages during both field trips. They were read hourly by local villagers for 13 hours a day.

The bathymetry of Segara Anakan was constructed by using the depth soundings of the ADCP with the shorelines of SPOT satellite pictures. The mangrove areas were extrapolated by the assumption that the spring tide has to reach 99% of the mangrove areas. Freshwater input was assessed by estimating the catchment area of the rivers entering Segara Anakan and correlating them in terms of catchment area to the measured discharge of the Citanduy River.

The Segara Anakan lagoon was modeled with the three-dimensional General Estuarine Transport Model (GETM, Burchard and Bolding, 2002, and www.getm.eu). Two additional tracers are implemented into the model: an age tracer which increases linear with time and mixes with zero age water at the boundaries, namely the ocean outlets, the rivers and the precipitation. Thus the age tracer represents the average residence time of water inside Segara Anakan. The second tracer is a completely passive tracer injected into the Citanduy River to follow the fate of the Citanduy water masses. Two runs were set up to model the lagoon at the field trip dates. A sensitivity study of the Citanduy discharge was done to assess the influence of the freshwater discharge onto the mean salinity and the water exchange flux between the eastern and the western parts.

## Results

The lagoon has a well mixed water body. Mean salinities of the two parts differ due to the larger freshwater input of the Citanduy into the western part (More than 80% of the overall catchment area belongs to the Citanduy River). The hydrodynamic of the western part is mainly driven by the tidal sea level changes and the freshwater runoff of the Citanduy River. During rising tide the Citanduy River plume is pushed into the central parts. It is followed by Indian Ocean water. The water masses mix on the way and inside the lagoon and leave the lagoon during falling tide. Long time salinity measurements in the Klaces village show this cycle. But during neap tide cycles in the rainy season the recordings did not show Indian Ocean water entering the lagoon. This happens because the high Citanduy water runoff during the rainy season is sufficient to fill the lagoon without Indian Ocean water entering through the western outlet. Then the concentration of Citanduy water inside the lagoon has its maximum value which also means high concentration of dissolved sediment. A sensitivity study of the Citanduy discharge shows a correlation of the east-west water volume transport with the Citanduy freshwater runoff. Low discharge rates mean a net westward transport. With higher discharges the net transport changes to the east (Figure 2). Differences of the mean salinities between the monsoon seasons are in the range of 8 g $kg^{-1}$ for the western part and 4 g $kg^{-1}$ in the eastern part. During dry season residence times of one to two weeks can be reached in the central parts of the lagoon. They decrease in the rainy season.

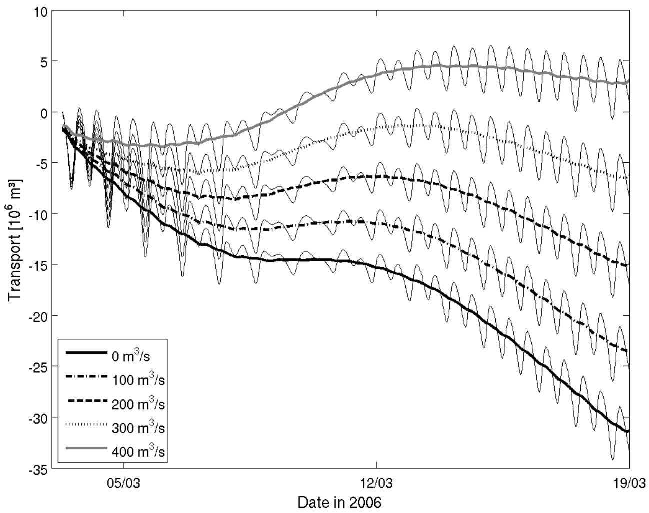


Figure 2: East-west water transport at the longitude of the water-exchange channel in Figure 1 depending on the Citanduy River runoff. A positive transport means to the east, a negative value to the west. The transports were filtered with a running mean filter having a 0.5 day time window. Discharges ranging from 0–200 m³ $s^{-1}$ result in a net eastward transport whereas a Citanduy discharge of 400 m³ $s^{-1}$ results in a net westward transport.

## Conclusions

Two field trips including a bathymetric survey, water volume flux measurements at key transects of the western lagoon, long time salinity measurements in the Klaces village and manual operated tide stations joined with a numerical simulation using the GETM model point out to be a good combination in an widely unknown area. The measured data can be well reproduced with the computer model. Especially the salinity measurements in the Klaces village and the absence of Indian Ocean water during neap tide cycles in the rainy season are reproduced. The absence is due to the high Citanduy discharge which has an over one tidal cycle accumulated volume sufficient to fill the western part. Different discharges of the Citanduy River strongly influence the mean salinities of the western and central parts and are mainly responsible for the salinity differences between the dry and the rainy season. They have furthermore a significant effect onto the water transports between the eastern and western parts of Segara Anakan.

## References


Burchard, H., Bolding, K. (2002), *GETM – a general estuarine transport model. Scientific documentation*, Tech. Rep. EUR 20253 EN, European Commission, 157pp.

White, A.T., Martosubroto, P., Sadorra, M.S.M. (1989), *The coastal environmental profile of Segara Anakan Cilacap, South Java, Indonesia*. ICLARM technical report 25.

Yuwono, E., Jennerjahn, T., Nordhaus, I., Riyanto, E.A., Sastranegara, M.H., Pribadi, R. (2007), Ecological status of Segara Anakan, Java, Indonesia, a mangrove-fringed lagoon affected by human activities, *Asian Journal of Water, Environment and Pollution*, 4, 61–70.

# The dynamics of Patos Lagoon coastal plume – a combination of numerical modeling and remote sensing techniques

WILIAN C. MARQUES, ELISA H.L. FERNANDES, IGOR O. MONTEIRO, BRUNO C. MORALES

Laboratório de Oceanografia Física, Fundação Universidade Federal do Rio Grande, Caixa Postal 474, CEP 96201-900 Rio Grande-RS, Brazil
email: wilian_marques@yahoo.com.br, e.fernandes@furg.br, igoromonteiro@yahoo.com.br, bcm_ocean@yahoo.com.br

*Keywords: freshwater discharge, plume, numerical modeling; Southern Brazilian Shelf*

## ABSTRACT

The Patos Lagoon, located in the southernmost part of Brazil, is connected to the Atlantic Ocean through a single narrow inlet, discharging continental water to the Southern Brazilian Shelf. The finite element model TELEMAC3D + SEDI3D (EDF, France) and the MODIS images are applied in this study to provide a description of the main features of the Patos Lagoon plume, as well as estimates of estuarine-shelf suspended sediment exchange. Results presented show that wind driven currents controls the behavior of the Patos Lagoon coastal plume. The plumes formed during the studied period present positive buoyancy indicating that brackish waters are lighter than ambient seawater. During the simulated period $6.5 \times 10^5$ tonnes of sediments are flushed to the coastal zone through the Patos Lagoon mouth forming coastal plumes with areas varying between 100 and 800 km$^2$. The quantitative calibration of that tool is necessary and the long term simulations will permit us to obtain annual estimates of estuarine-shelf suspended sediment exchange.

## Introduction

Continental shelves receive water and suspended matter transported via river discharge. The dynamic structure formed by this process is a buoyant low density water mass with high suspended matter concentration, namely a coastal plume. The input of materials and interaction between continental waters and coastal processes contribute to the maintenance of favorable environments for reproduction, development of species, sustainable deposition and transport patterns. Mann and Lazier (1991) present evidence of the fluvial discharge influence on the intensification of biological activities and maintenance of fishing stocks in estuaries and coastal zones.

The fate and behavior of coastal plumes is controlled by linear and nonlinear processes, and their study can be accomplished through field data analysis, remote sensing and analytical and numerical models. Most of the studies about the dynamics of plumes were developed in coastal regions of North America, involving field data (e.g., Hickey et al., 1998; Johnson et al., 2003) and numerical models (e.g., Kourafalou et al., 1996a, b; Fong and Geyer, 2001; 2002; Guo and Valle-Levinson, 2007). Among the studies based on remote sensing techniques, Miller and McKee (2004) present the successful use of the MODIS Terra 250 m imagery to map the concentration of total suspended matter of different sources in the Northern Gulf of Mexico.

Studies on the dynamics of plumes in the Southern Brazilian Shelf (Figure 1), on the other hand, are sparse. The SBS is located between 28°S and 35°S, and receives freshwater contributions from the La Plata River and the Patos Lagoon, which are advected by local coastal currents. At the southern boundary of the SBS, the La Plata River, the second main hydrographic basin of South America, discharges an annual mean of 22,000 m$^3$ s$^{-1}$ of freshwater in the coastal zone (Guerrero et al., 1997). Towards the north, the Patos Lagoon discharges on average ten times less water over the shelf and presents seasonal and inter-annual discharge variability. Numerical modeling studies of coastal plumes in the SBS, however, lack in space-time resolution and studies on the dynamics of the Patos Lagoon coastal plume considering the small scale process are even more limited. Zavialov et al. (2003) monitored the behavior of this plume under intense river runoff conditions using salinity and temperature observations. Recently, Marques et al. (submitted) studied the physical forcing controlling the formation and behavior of the Patos Lagoon plume based on a three-dimensional hydrodynamic numerical model. The aim of this study is to provide a description of the main features of the Patos Lagoon plume, as well as estimates of estuarine-shelf suspended sediment exchange based on 3D numerical modeling experiments and MODIS Aqua image analysis.

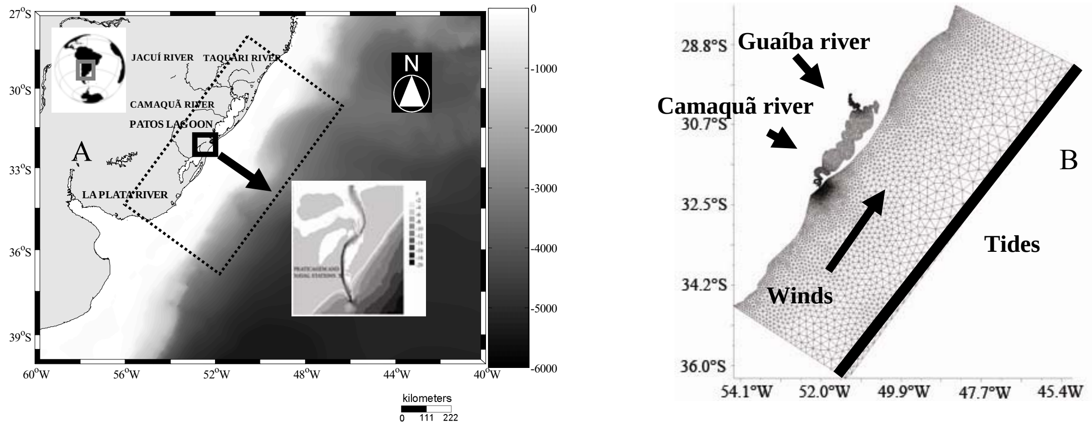


Figure 1. Southern Brazilian Shelf (dotted rectangle) showing the Patos Lagoon and principal tributaries and the estuarine region (A). The finite element mesh with positions of the liquid and surface boundaries (B).

## Methods

The TELEMAC3D+SEDI3D model was used to carry out three-dimensional simulations of the hydrodynamic and sediment transport for the study area. TELEMAC is a finite element flow model developed by ©EDF – Laboratoire National d'Hydraulique et Environnement of the Company Eletricité de France (EDF) to simulate the flow in estuaries and coastal zones. The study area was defined between 28°S and 34°S and the oceanic boundary was located at the 3600 m isobath. The resulting finite element mesh contains around 8974 nodes (Figure 1B). The simulations were performed during 56 days from 1 July to 25 August 2002. The model was forced at the top of the Patos Lagoon with time series of river discharge from the main tributaries, obtained from the Brazilian National Water Agency web site (www.ana.gov.br). The wind data was obtained from the Reanalysis web page (www.cdc.noaa.gov/cdc/reanalysis) and prescribed as a dynamic surface boundary condition. The main tidal components for the area ($M_2$, $N_2$, $O_1$, $S_2$ and $K_1$) were obtained from the FES95.2 model (Finite Element Solution V95.2) and prescribed along the oceanic boundary of the model. The location of the liquid, surface and boundary conditions are showed in the Figure 1B.
The hydrodynamic model ran with a 60 s time step and was initialized from rest with a surface elevation of 0.6 m and thermohaline fields obtained from the OCCAM project (Ocean Circulation and Climate Advanced Modelling Project – www.soc.soton.ac.uk/JRD/OCCAM/). The horizontal and vertical turbulence models used were the Smagorinsky and the mixing length jet, respectively. The calibration of the 3-D hydrodynamic model was accomplished by Marques et al. (submitted). The sediment model was initialized with null concentration of suspended and with consolidated sediments. The source of sediments was at the liquid boundaries with constant concentration of 0.25 kg m$^{-3}$.The mean grain diameter $d_{50}$ was considered 0.01 mm, relative to silt particles. The suspended sediment plumes calculated by the model were qualitatively compared with the information extracted from the MODIS – Aqua (MODerate-resolution Imaging Spectroradiometer, www.laadsweb.gov) sensor. Their images were processed to generate products with spatial resolution of 250 m. The energy reflectance in the 667 nm was used as a tracer of the suspended matter (Li et al., 2003).

## Results and discussion

The behavior of the Patos Lagoon sediment plume calculated by the numerical model for 21 August (day 45) and 26 August (day 50) was compared with MODIS images for the same period. The periods were chosen according to the cloud covering and the predominant wind conditions observed in the area: the first period represents northeasterly wind conditions (Figure 2A) and the second indicates southwesterly conditions (Figure 2B). Northeasterly winds favor upwelling conditions along the SBS, enhancing the southwestward transportation of the coastal plume (Figure 2C). On the other hand, southwesterly winds contribute to downwelling conditions, displacing the coastal plume northeastward along the shelf (Figure 2D). A qualitative comparison between modeling results (Figures 2C and D) and the product of the MODIS images (Figures 2E and F) indicate good agreement between the techniques, apart from the limitations associated with the initial and boundary conditions for suspended matter concentration in the Patos Lagoon used in the modeling experiments.

The relation between the series was quantified for the profiles presented in (Figure 2) through a correlation coefficient ($r$), resulting from the comparison between calculated suspended matter and reflectance of the superficial transects at 45 (A) and 50 (B) days of simulation, with values of 0.67 and 0.69, respectively. The vertical profiles of the same period (Figure 3) show upwelling conditions induced by the wind action for the

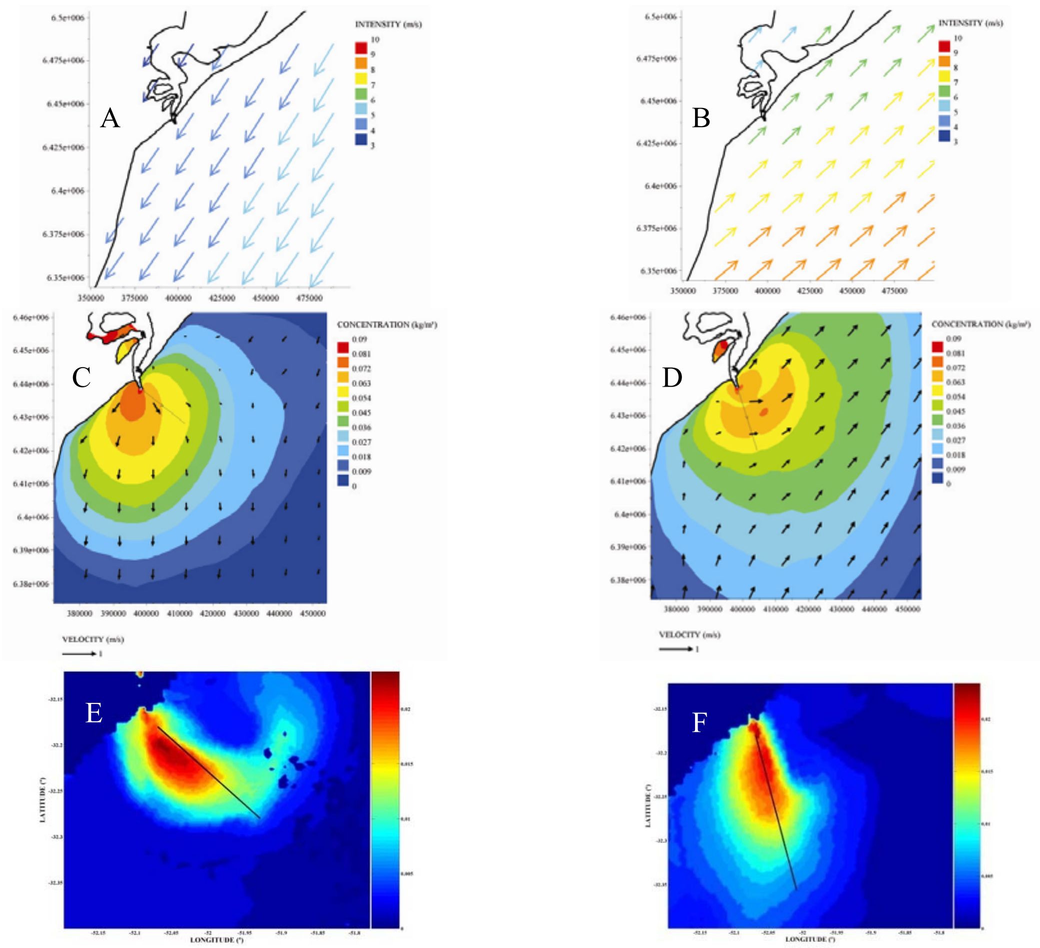


Figure 2. NE (A) and SW winds (B). Suspended matter calculated on superficial layer after 45 (C) and 50 (D) days of simulation. Reflectance images (667 nm) for Julian day 233 (day 45) (E) and Julian day 238 (day 50) (F).

first period (Figure 3A), and downwelling conditions for the second (Figure 3B). The transport of suspended matter along the coast occurs on the surface layer, resulting in positive buoyancy and indicating that waters from the coastal plume are lighter than seawater. This pattern of dispersion along the south Brazilian adjacent coast characterizes the formation of hypopycnal coastal plumes, corroborating previous observations on the SBS and the true color satellite images obtained. This condition is predominant around the world and the most prominent examples are the Amazon, the Yangtze and the Mississippi rivers (Wright and Friedrichs, 2006), with density of sediments around 0.14, 0.53 and 0.36 kg $m^{-3}$, respectively. Wright and Nittrouer (1995) considered that densities of sediments around 25 kg $m^{-3}$ as in the Yellow River are required to produce negative buoyancy (hyperpycnal) conditions.

The total mass flux (suspended sediment) to the adjacent coastal zone was estimated by integrating the suspended matter flux at each sigma level across the vertical section of the Patos Lagoon channel (Figure 4A). The result is a time series indicating that the mass flux to the coastal zone reached a maximum between 44 and 55 days of simulation, exporting more than $5 \times 10^4$ tonnes $d^{-1}$ (Figure 4B, blue line). Until this point of the simulation (56 days) the Patos Lagoon discharged ~$6.3 \times 10^5$ tonnes of fine sediment to the inner continental shelf. Wright and Friedrichs (2006) estimated that the Amazon, Yangtze and Mississippi rivers export around $1.2 \times 10^9$, $0.48 \times 10^9$ and $0.21 \times 10^9$ tonnes $yr^{-1}$. The plume area (Figure 4B, green line) was calculated for each day of the simulation taking 0.05 kg $m^{-3}$ as the front of the sediment plume. Results indicate that during the maximum flux of sediments (between 44 and 55 days of simulation) the coastal plume area can reach 800 $km^2$.

## Conclusions

Modeling results for the Patos Lagoon coastal plume are in agreement with MODIS remote sensing images. Wind driven currents control the behavior of the Patos Lagoon coastal plume. The coastal plumes formed during the study period have positive buoyancy (brackish waters are lighter than seawater). During the simulated period $6.5 \times 10^5$ tonnes of sediments are flushed to the coastal zone through the Patos Lagoon mouth, forming coastal plumes with areas varying between 100 and 800 $km^2$.

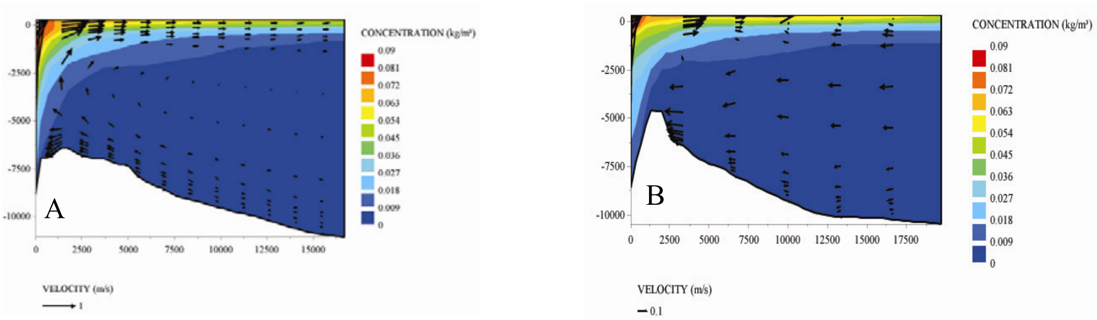


Figure 3. Suspended sediment vertical profiles after 45 (C), 50 (D) days' simulation, ×1000 vertical exaggeration.

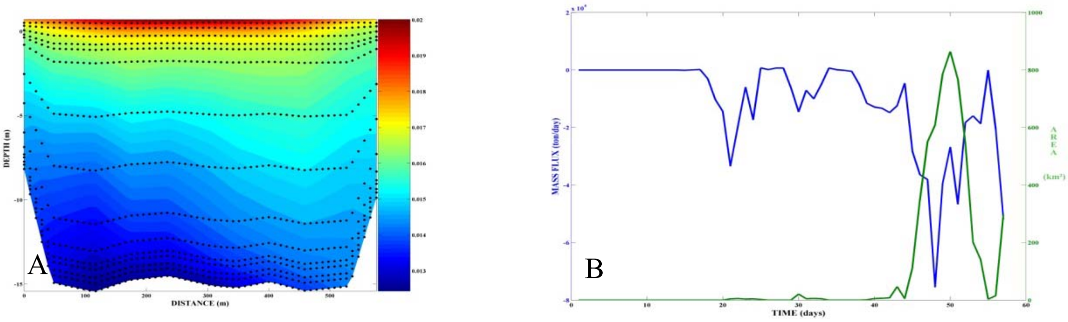


Figure 4. Vertical section of sediment concentration, 15 sigma levels near the Patos Lagoon mouth (A). Total mass flux time series for 56 days simulation (B) from 1 July–28 August. Green line represents the plume area.

## References


Fong, D.A., Geyer, W.R. (2001), Response of a river plume during an upwelling favorable wind event, *Journal of Geophysical Research*, 106(C1), 1067–1084.

Fong, D.A., Geyer, W.R. (2002), The Alongshore transport of freshwater in a surface-trapped river plume, *Journal of Physical Oceanography*, 32, 957–972.

Guerrero, R.A., Acha, E.M., Framiñan, M.B., Lasta, C.A. (1997), Physical oceanography of the Rio de La Plata estuary, Argentina, *Continental Shelf Research*, 17(7), 727–742.

Guo, X., Valle-Levinson, A. (2007), Tidal effects on estuarine circulation and outflow plume in the Chesapeake Bay, *Continental Shelf Research*, 27, 20–42.

Hickey, B.M., Pietrafesa, L.J., Jay, D.A., Boicourt, W.C. (1998), The Columbia River plume study: Subtidal variability in the velocity and salinity fields, *Journal of Geophysical Research*, 103(C5), 10339–10368.

Johnson, D.R., Miller, J. (2003), Dynamics and optics of the Hudson River outflow plume, *Journal of Geophysical Research*, 108(C10), 3323–3231.

Kourafalou, V.H., Oey, L.Y., Wang, J.D., Lee, T.N. (1996a), The fate of river discharge on the continental shelf 1. Modeling the river plume and the inner shelf coastal current, *Journal of Geophysical Research*, 101(C2), 3415–3434.

Kourafalou, V.H., Lee, T.N., Oey, L.Y., Wang, J.D. (1996b), The fate of river discharge on the continental shelf 2. Transport of coastal low-salinity waters under realistic wind and tidal forcing, *Journal of Geophysical Research*, 101(C2), 3435–3455.

Li, R.-R., Kaufman, Y.J., Gao, B.-C., Davis, C.O. (2003), Remote sensing of suspended sediments and shallow coastal waters, *IEEE Transactions on Geoscience and Remote Sensing*, 41(3), 559–566.

Mann, K.H., Lazier, J.R.N. (1991), *Dynamics of marine ecosystems: Biological-Physical interactions in the Oceans*. Blackwell Scientific Publications, Inc, Boston.

Marques, W.C., Fernandes, E.H., Monteiro, I.O., Möller, O.O. (2008), Numerical modeling of the Patos Lagoon coastal plume, Brazil, *Continental Shelf Research*. (Submitted.)

Miller, R.L, McKee, B.A. (2004), Using MODIS Terra 250 m imagery to map concentrations of total suspended matter in coastal waters, *Remote Sensing of Environment*, 93, 259–266.

Wright, I.D., Nittrouer, C.A. (1995), Dispersal of river sediments in coastal seas: six contrasting cases, *Estuaries*, 18, 494–508.

Wright, L.D., Friedrichs, C.T. (2006), Gravity-driven sediment transport on continental shelves: A status report, *Continental Shelf Research*, 26(2006), 2092–2107.

Zavialov, P.O., Kostinoy, A.G., Möller, O.O. (2003), Mapping river discharge effects on Southern Brazilian shelf, *Geophysical Research Letters*, 30(21), 2126, doi:10.1029/2003GL018265.

# Wind driven circulation in a semi-enclosed and well-mixed bay, Bahía Concepción

AURÉLIEN L. PONTE[1], GUILLERMO GUTIÉRREZ DE VELASCO[2], ARNOLDO VALLE-LEVINSON[3], CLINTON D. WINANT[1], KRAIG WINTERS[1]

1. Scripps Institution of Oceanography, University of California, San Diego, 9500 Gilman Drive, La Jolla CA 92093-0209, USA
email: aponte@ucsd.edu, cwinant@ucsd.edu, kraig@ucsd.edu

2. Unidad Foránea La Paz, CICESE, La Paz, Mexico
email: ggutierr@cicese.mx

3. Civil and Coastal Engineering, University of Florida, 365 Weil Hall, P.O. Box 116580, Gainesville FL 32611-6580, USA
email: arnoldo@ufl.edu

*Keywords: wind circulation, set up, currents, time dependence*

## ABSTRACT

Numerous models have described the expected response of a well-mixed coastal basin to steady winds (Csanady, 1982; Hunter and Hearn, 1987; Wong, 1994; Mathieu et al., 2002; Winant, 2004). A central feature is the rising of the sea surface elevation in the downwind direction in order to conserve mass through any vertical section. The lateral variability of the flow is controlled by bathymetry with downwind flow over shallow areas where the wind stress dominates and balances bottom friction, and upwind flow in deeper areas where the sea surface slope dominates. The effect of rotation is described by the non-dimensional Ekman depth $\delta_E$, defined as the ratio of the dimensional Ekman depth to the maximum depth of the basin, determines the importance of rotation (Winant, 2004, 2006; Sanay and Valle-Levinson, 2005). For small $\delta_E$, the axial (parallel to the wind) circulation is relatively similar than in the non-rotating case but the lateral circulation is now organized vertically around a surface and bottom Ekman layers of size $\delta_E$ and a geostrophic interior. In the surface Ekman layer, the flow is intensified and to the right of the wind, balanced in the interior by a weaker but vertically widespread return flow.

These recent developments motivated a one year long observational experiment (Fall 2004–Fall 2005), which focused on identifying the effect of the Coriolis acceleration on the wind driven circulation of a well-mixed bay. Here, we will use the observations gathered during this campaign and compare the wind driven response predicted by the above-mentioned models and the observed one.

### Experimental site and instrumentation

Bahía Concepción B.C.S., México, is located on the western side of the Gulf of California. The bay has been selected because of its regular bathymetry (Figure 1) reaching depth of 30 m, roughly three times the estimated local Ekman depth. In fall and winter, strong (>0.1 Pa) wind events directed toward the closed end of the bay blow for period few days and maintain well-mixed conditions. Two meteorological stations measured the wind speed at the closed and open end of bay, from which values of the wind stress were inferred. Two pressure sensors were moored close to the meteorological stations and lead to estimates of the sea surface elevation. Seven ADCPs were deployed and measured vertical profiles of currents. As far as the wind driven current response is concerned, we will focus here on the February–March time period when all ADCPs were aligned along a single cross-section going across the center of the bay (Figure 1).

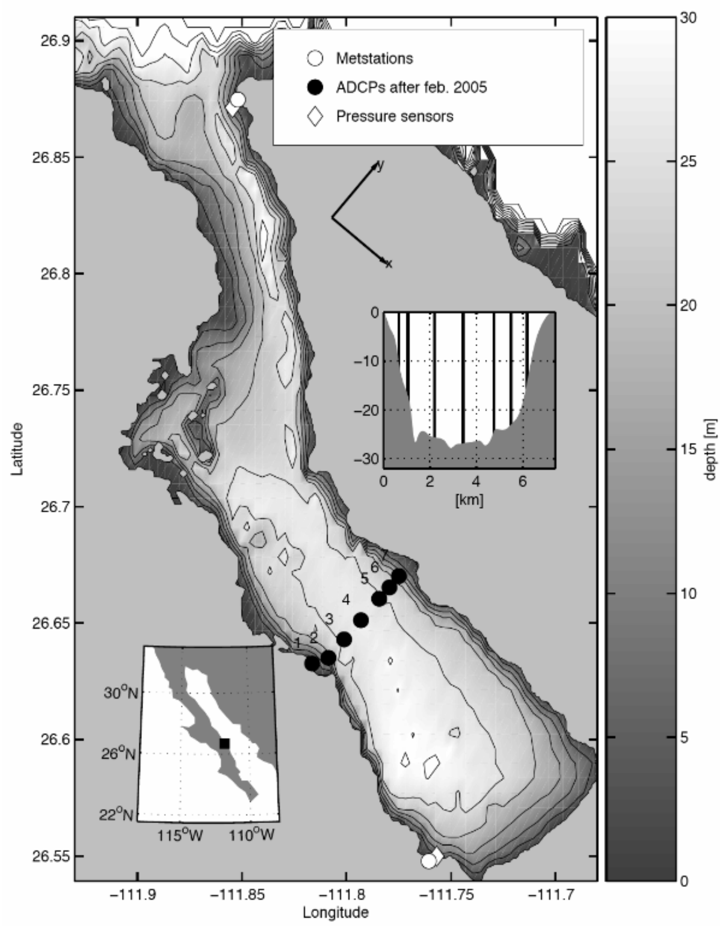


Figure 1. Bathymetric map of Bahía Concepción. Depth is indicated by the gray shading, instruments by the large symbols. The vertical section in the middle is along the ADCP line. The position of Bahía Concepción with respect to the Baja Peninsula is represented by the black square on the bottom left map. The arrows represent the chosen along ($x$) and across ($y$) bay directions.

## Pressure response

The one year long time series of bottom pressure is low pass filtered and compared with the wind stress observations. The low passed difference of sea surface elevation between closed and open end stations is well to wind stress in the sense that it is positive in the downwind direction. The amplitude of the set up is consistent with the scaling inferred from a 2D momentum balance between wind stress and bottom pressure.
An analysis in the frequency domain is carried in order to explore the response at higher frequencies. The challenge is then to separate the tidal signal, mostly diurnal here, from the wind response. The analysis is complicated by diurnal modulation of the wind and the proximity of the quarter wavelength resonance, estimated around 5 cpd.

## Current response

A lagged linear regression analysis shows that wind driven axial currents are downwind on the western shallow side of the bay with a return flow at depth. A strong lateral circulation, consistent with a Coriolis effect, is observed with currents at the right of the wind at the surface and in the opposite direction at depth.

Because the winds are diurnally modulated along with the tide and inertial frequency being near diurnal, an attempt is made to extract the current frequency response. This approach is motivated by the low correlation and variable lags produced by the linear regression with hourly averaged current observations.

A direct extension of the models described in the introduction to the time periodic case provided a basis for the interpretation of the spectral approach.

## Conclusions

Pressure, current and wind stress observations have been used in order to understand the response of a well-mixed bay to winds. It compares well with recent model developments and seems to confirm the role predicted by rotation. Because the winds are modulated at the diurnal/inertial frequency, attempts are made toward understanding the time dependent response. An extension of recent steady models to the time periodic case is compared to the observations.

## References

Csanady, G.T. (1982), *Circulation In The Coastal Ocean*. Environmental fluid mechanics, D. Reidel.

Hunter, J.R., Hearn, C.J. (1987), Lateral and vertical variations in the wind-driven circulation in long, shallow lakes, *Journal of Geophysical Research*, 92, 13106–13114.

Mathieu, P.P., Deleersnijder, E., Cushman-Roisin, B., Beckers, J.M., Bolding, K. (2002), The role of topography in small well-mixed bays, with application to the lagoon of Mururoa, *Continental Shelf Research*, 22, 1379–1395.

Sanay, R., Valle-Levinson, A. (2005), Wind-induced circulation in semi-enclosed homogeneous, rotating basins, *Journal of Physical Oceanography*, 35, 2520–2531.

Winant, C.D. (2004), Three dimensional wind-driven flow in a linear, constant density, rotating basin, *Journal of Physical Oceanography*, 34, 462–476.

Winant, C.D. (2006), Three-dimensional wind-driven coastal circulation past a headland, *Journal of Physical Oceanography*, 36, 1430–1438.

Wong, K.C. (1994), On the nature of transverse variability in a coastal plain estuary. *Journal of Geophysical Research*, 99, 14209–14222.

# Modulation of tidal residual flows in a North-Florida Inlet

AMY WATERHOUSE, ARNOLDO VALLE-LEVINSON

Civil and Coastal Engineering, University of Florida, P.O. Box 116580,
Gainesville FL 32611-6580, USA
email: awaterhouse@ufl.edu, arnoldo@ufl.edu

*Keywords: tidal residual circulation, modulation*

## ABSTRACT

The residual circulation in many estuaries is caused by a complex interaction among tides, winds and density gradients. Such an interaction conceals the separate influence that each agent exerts on the mean or residual flow. For instance, it is challenging to observe the tidal residual circulation in an estuary where the circulation is driven mainly by density gradients. There are estuaries in subtropical regions that have only sporadic freshwater influence and where the residual flow is typically driven by tides and winds. These are ideal sites to compare observations on the spatial structure of tidal residual flows to theoretical results. This spatial structure is different from short basins to long basins where the bathymetry consists of a channel flanked by shoals (Li and O'Donnell, 2005). In a short basin, the tide is a standing wave and the spatial structure of the tidal residual flows consists of net inflow in the channel and net outflow over shoals. The pattern is opposite in long basins where the tide is a progressive wave: inflow over shoals and outflow in channel. A long basin is one in which one quarter of the tidal wavelength is smaller than 1.4 to 1.7 times the length of the basin (Li and O'Donnell, 2005). Several examples of the lateral structure of tidal residual flows in long (e.g., Kjerfve and Proehl, 1979; Cáceres et al., 2003) and short (e.g., Valle-Levinson et al., submitted) basins have been presented. Little is known, however, on the temporal variability or modulation of the lateral structure of tidal residual flows in long basins. The purpose of this study is to document with observations the lateral structure of tidal residual flows in a basin where the tide is between progressive and standing. This study also seeks to determine whether the modulation of the tidal residual structure is produced by tides or winds.

### Methods

In order to characterize the lateral structure of tidal residual flows and the temporal variability of such lateral structure, underway current velocity profiles and water density profiles were combined with time series of current profiles at the entrance to a subtropical estuary, Ponce de Leon Inlet. This inlet is located on the central Florida Atlantic coast at a latitude of 29.07°N (Figure 1). The entrance to the inlet is ~350 m wide and ~12 m deep in a channel that is only ~100 m wide. At the inlet, the channel is flanked asymmetrically by shoals that are typically <2.5 m deep. The tide is predominantly semidiurnal with a mean tidal range of 0.7 m and typical tidal currents exceeding 1 m $s^{-1}$.

Surveys were carried out at the entrance to Ponce de Leon Inlet on 5 September 2007 and on 21 February 2008. Both surveys stretched for ~11 hrs during spring tides (in February) and between spring and neap tides (in September). During both surveys, a boat-mounted 1200 kHz ADCP with bottom-track capability was used to measure current profiles along three cross-channel transects. One of the transects crossed the entrance to the inlet and was used to characterize the spatial structure of net exchange flows (Transect 1 in Figure 1). The transects were sampled 15 and 17 times during the September and February surveys, respectively. The temporal coverage at each survey allowed separation of tidal from non-tidal signals through a least-squares fit to semidiurnal and sixthdiurnal harmonics. Also during the surveys, water density profiles were measured with a SeaBird SBE19-Plus CTD at the deepest part of each transect during every other transect repetition. This allowed for the estimation of mean horizontal density gradients and their influence on the mean flows.

Time series of current velocity profiles were obtained with bottom-mounted ADCPs, equipped with pressure sensors, deployed at three locations determined on the basis of the September survey results. Two instruments (Stations 1 and 3, Figure 1) were moored over the shoals flanking the channel, where the third instrument was installed (Station 2 in the channel, Figure 1). These instruments recorded data for ~75 days distributed in two periods, from 14 January 2008 to 25 February 2008 and from 25 February 2008 to 2 April

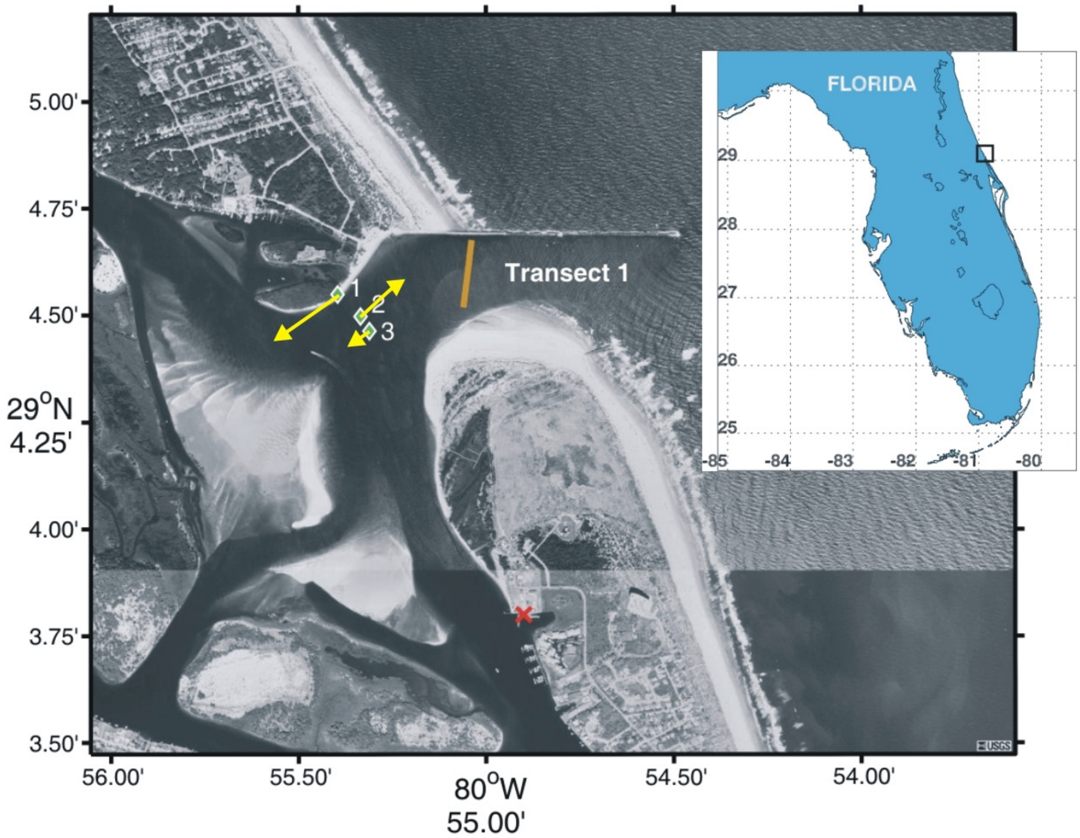


Figure 1. Study area on the east coast of Florida, USA. Transect 1 indicates the location of underway velocity profiles. Green diamonds show location of ADCP moorings and red cross denotes location of tide gauge used to distinguish spring and neap tide periods of Figure 2. The mean flows for the entire deployment period appear as yellow arrows (the longest yellow arrow is 7 cm s$^{-1}$).

2008. During the second period the instrument at Station 3 was damaged and the record is unavailable. Instruments recorded the average of 400 pings distributed over 10-minute intervals and at 0.5 m bins. The deployment-long average was calculated for each mooring to characterize the lateral structure of the mean flow. The subtidal variations of this structure were determined with the low-pass filtered time series of each bin at each mooring. The filter was a Lanczos-type with half-power of 34 h.

## Results

The CTD data obtained from the survey showed that the inlet is affected by waters of Gulf Stream origin (salinity of 36.2) during flood and by lower salinity water (34) during ebb. The water column was mixed during flood and weakly stratified during ebb. The tidally averaged horizontal density gradient $<\partial\rho/\partial x>$ estimated from the three CTD stations was of O($10^{-4}$) kg m$^{-4}$. However, the tidally averaged accelerations produced by the baroclinic pressure gradient $<(gH/\rho)\ \partial\rho/\partial x>$, where $g$ is acceleration due to gravity, $H$ is water depth and $\rho$ is a reference water density, were of O($10^{-6}$) m s$^{-2}$ because of the shallow mean depths ($H < 4$ m). These accelerations were two orders of magnitude smaller than those arising from the tidally averaged bottom stresses $<C_d u^2/H>$ ($C_d$ is an a dimensional drag coefficient (0.0025) and $u$ is the along-axis flow), which were at least of O($10^{-4}$) m s$^2$. Given these large tidally averaged bottom stresses, the pattern of net flows was most likely driven by tidal distortion. In fact, the mean flow pattern during the September survey consisted of outflow in the channel and inflow over the shoals. The net flow was laterally sheared with very weak vertical shear, consistent with theoretical results for a progressive tidal wave (Li and O'Donnell, 2005; Winant, 2008). The moored ADCP data were explored to determine the progressive nature of the tidal wave and to assess the consistency of the mean flows with the observed survey results.

The relationship between sea level and currents observed with the moored ADCPs indicated a phase lead of ~30° by both the semidiurnal and diurnal tidal currents relative to the tide. This indicated that the tide in Ponce de Leon Inlet is closer to progressive than standing. In this type of basin, the Stokes velocity will be

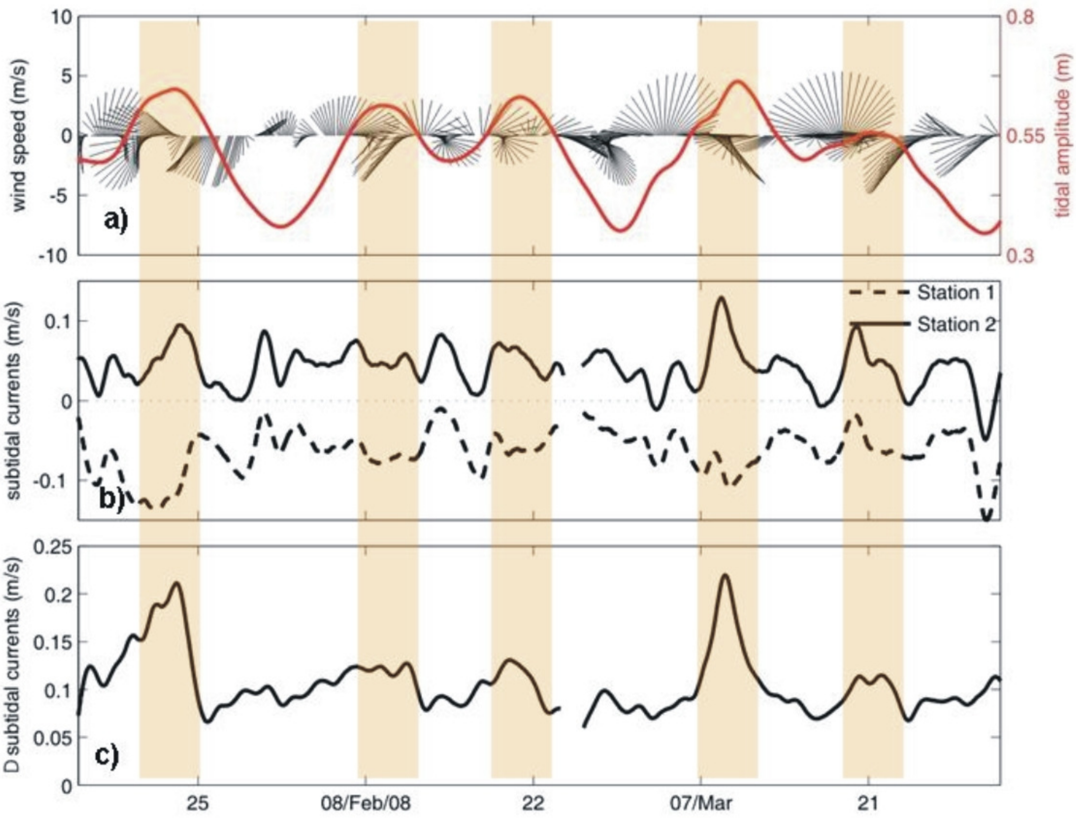


Figure 2. Time series data of tidal amplitude and wind velocity in oceanographic convention (a); low-pass filtered depth-averaged currents in the channel (Station 2) and over the shoal (Station 1) (b); and difference between the subtidal flow in the channel '2' and the subtidal flow over the shoal, denoting strength of subtidal water exchange (c). The colored periods indicate spring tides, when exchanges were strongest.

influential on the residual flow and will produce a pattern consistent with a progressive tidal wave (Li and O'Donnell, 2005). Indeed, the average flow at each of the three mooring stations indicated outflow in the channel and inflow over the shoals (Figure 1) with net horizontal flows almost uniform in the vertical. The low-pass filtered data showed that the pattern of outflow in the channel and inflow over shoals persists throughout the observation period (Figure 2). Such pattern displays variations that are related to wind forcing but that maintain the sign of the net flows at each station. Interestingly, when the outflow in the channel increases, the inflow over the shoals decreases. This is likely caused by net seaward transport of water throughout the entire cross-section of the inlet. The opposite response develops with a landward transport, suggesting the influence of remote effects in modulating the exchange. However, the strength of the net exchange flow, as determined by the difference between the inflow at Station 1 and the outflow at Station 2, is actually modulated by the fortnightly tidal cycle. The strongest exchange flows occurred during the largest spring tides of 23–24 January and 8 March. Also, large exchange flows developed during the spring tides of 8–9 February, 20–21 February and 21 March. Tidal forcing was therefore more influential in determining the strength of exchange flows than wind forcing. This is because tidal residuals represent bidirectional flows (inflow over shoals and outflow in the channel) and wind-driven flows seem to be unidirectional at the section sampled.

## Conclusions

The following conclusions may be drawn from this study. 1) The net exchange flows observed at Ponce de Leon Inlet were consistent with theoretical tidal residual flows for a progressive wave. 2) The pattern of net outflow in the channel and net inflow over the shoals persisted under different tidal amplitudes and wind forcing conditions. 3) The magnitude of the subtidal flow at each station was modified by wind forcing but the strength of the exchange flows across the entrance was modulated by tidal forcing. 4) The strongest exchange flows occurred during spring tides.

References


Cáceres, M., Valle-Levinson, A., Atkinson, L. (2003) Observations of cross-channel structure of flow in an energetic tidal channel, *Journal of Geophysical Research*, 108(C4), 3114, doi:10.1029/2001JC000968.

Kjerfve, B., Proehl, J.A. (1979), Velocity variability in a cross-section of a well mixed estuary, *Journal of Marine Research*, 37, 409–418.

Li, C.Y., O'Donnell, J. (2005), The effect of channel length on the residual circulation in tidally dominated channels, *Journal of Physical Oceanography*, 35, 1826–1840.

Valle-Levinson, A., Gutierrez de Velasco, G., Trasviña, A., Souza, A., Durazo, R., Mehta, A. (2008), Residual exchange flows in subtropical estuaries, *Estuaries and Coasts*. (Submitted.)

Winant, C.D. (2008), Three dimensional residual tidal circulation in an elongated, rotating, basin, *Journal of Physical Oceanography*. (In press.)

# Residual fluxes of suspended sediment in a tide-dominated tropical estuary

CARLOS A.F. SCHETTINI[1], MARÇAL D. PEREIRA[2], LUIZ B. DE MIRANDA[3], EDUARDO SIEGLE[3], MARIO P. SILVA[4], FERNANDO ANDUTTA[3]

1. Centro de Ciências Tecnológicas da Terra e do Mar, Universidade de Vale do Itajaí, R. Uruguai 458, Itajaí SC 88302-202, Brazil
   email: carlos.schettini@pq.cnpq.br, guto.schettini@gmail.com

2. Programa de Pós-Graduação em Geociências, Universidade Federal do Rio Grande do Sul, Av. Bento Gonçalves 9500, Porto Alegre RS 91509900, Brazil
   email: marcalpereira@pop.com.br

3. Instituto Oceanográfico, Universidade de São Paulo, Praça do Oceanográfico 191, São Paulo SP 05508120, Brazil
   email: miranda@io.usp.br, esiegle@io.usp.br, fernando_andutta@yahoo.com

4. Universidade Federal do Rio Grande do Norte, Campus Universitário, Caixa Postal 1524, Natal RN 59072970, Brazil
   email: mariop@ufrn.br

*Keywords: sediment transport, tidal asymmetry, ADCP, suspended particulate matter*

## ABSTRACT

This work assesses the fine sediment fluxes in the complex Caravelas estuarine system (Bahia, Brazil, Figure 1). The estuary reaches the ocean in front of the Abrolhos reef, the largest tropical reef habitat in the South Atlantic. The Caravelas estuarine system comprises several meandering channels which are connected to the ocean by a double inlet system. These two openings are interconnected by a narrow 30 km long channel. Although being the largest, due to its small drainage basin the Caravelas portion of the estuary receives an insignificant continental input. The southern portion of the estuary (Nova Viçosa) receives the contribution of the Peruíbe River, which drains an area of approximately 5000 km$^2$. This unique aspect, with the differential input at each portion of the estuary results in complex hydrodynamic and suspended sediment transport patterns.

With the aim of better understanding the dynamics of this estuarine system, two extensive field campaigns were conducted covering both the dry winter (August 2007) and wet summer (January 2008) conditions. Field campaigns include synoptical tidal surveys at three fixed stations (two close to the inlets and one at the connection channel), longitudinal surveys, and 20-day long ADCP moorings in the Caravelas channel. This paper focuses on the mooring data to asses the synodical modulation of the suspended sediment residual fluxes.

### Materials and methods

Two intensive field campaigns were carried out during dry winter (August 2007) and wet summer (January 2008). Each campaign covered a full synodical period, where spring and neap 13-hour tidal surveys were carried out at five sites. Three sites were surveyed synoptically, covering the two inlets and the interconnection channel (stations #A, #B and #C in Figure 1). During the next day sites #D and #E were surveyed; these are located at the mouth of the two main rivers that drains the region, the Itanhém River to the north (#D), and the Peruípe River to the south (#E). Longitudinal surveys were also carried out along the Caravelas estuary, at high tide for spring and neap conditions. Additionally, two ADCP were moored near sites #A (both campaigns) and #B (January 2008 campaign only) to obtain continuous records of sea level, currents, salinity and turbidity during the campaigns.

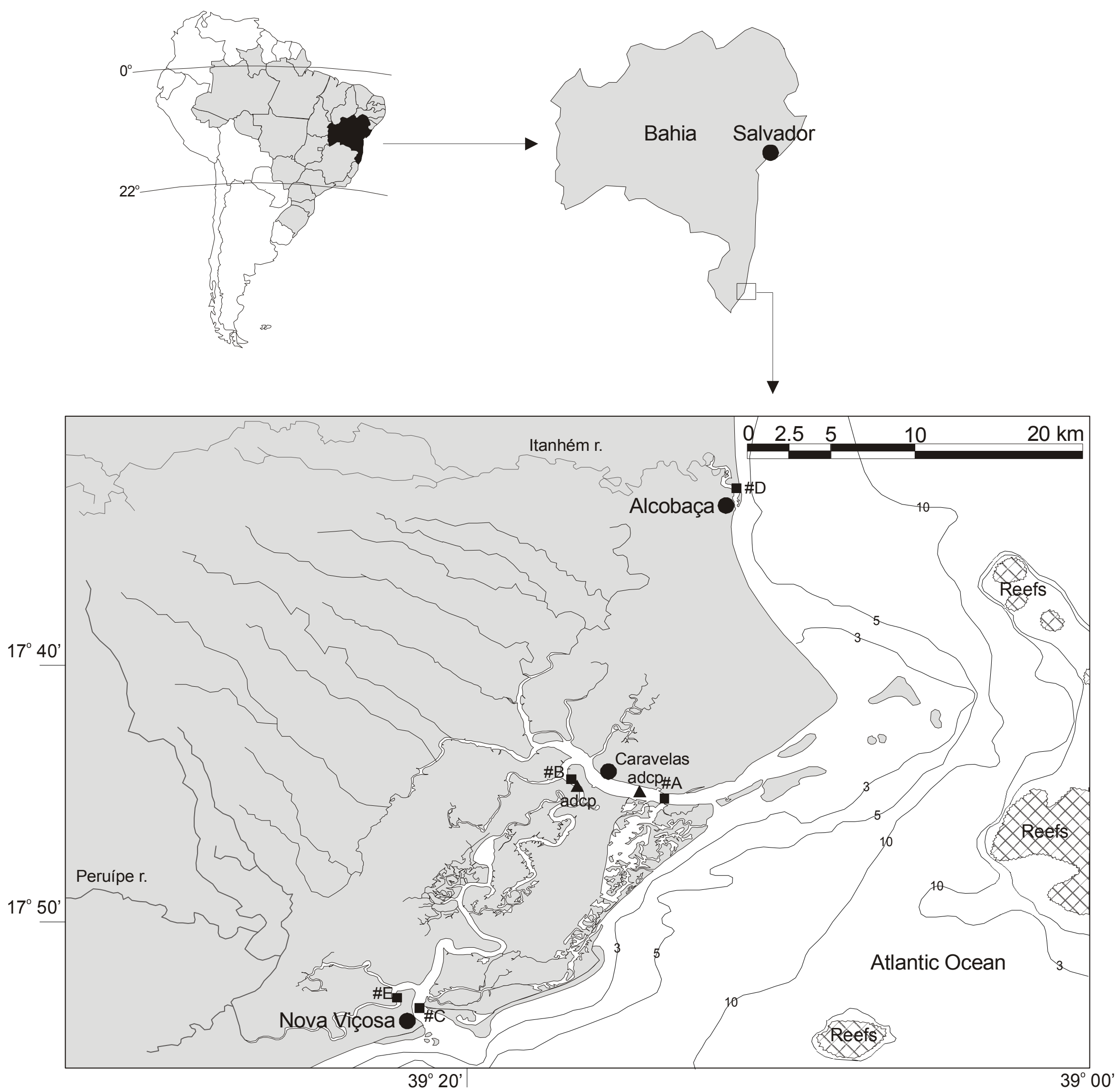


Figure 1. Location of the Caravelas Estuary, its drainage and the sampling stations. The triangle represents the ADCP mooring site; triangles represent the tidal surveys sites.

The tidal surveys were carried out using a variety of instruments. The main survey station #A included chemical and biological sampling. Currents were recorded using a down looking ADCP model ADP 1500 by Sontek. Salinity and temperature were recorded using a SD204 ctd probe by Saiv A/S and turbidity using a SeaPoint optical back scatter (OBS) probe, during the August 2007 campaign. During the January 2008 campaign, salinity and temperature were recorded with a ctd probe developed by Alec Eletronics, with an embedded OBS probe. The other stations were surveyed with a Valeport SK100 current-meter, with salinity and temperature probes, and turbidity was recorded with a SeaPoint OBS probe. All tidal survey stations were performed from anchored boats.

The mooring station nearby site #A consisted of an up looking Nortek ADCP Aquadopp Profiler of 1000 kHz, with CTD recorders at surface and bottom levels, one SD202 by Saiv A/S and another XR420 by RBR. The bottom CTD was attached to the ADCP frame and the surface CTD was suspended 1 m bellow a surface buoy. Unfortunately the ADCP frame was underweighted and tilted during the spring tide current peaks. The pressure transducer of the surface recorder indicated that during spring tide the buoy was dragged down to the bottom, in a 15 m deep area. During the second campaign the ballast of the ADCP frame was increased, and an Alec Electronics CT recorder was used inside the ADCP frame. Additionally, the surface CTD was not suspended by the marking buoys, being attached to a pile at the nearby margin. The mooring station nearby site #B consisted of an up looking ADCP Argonaut (Sontek), with an attached Alec Electronics CT recorder.

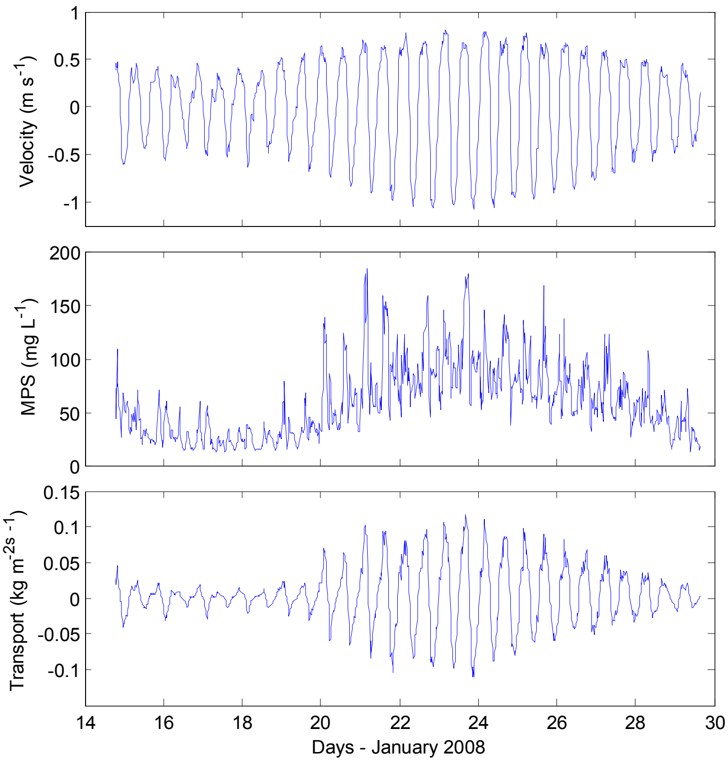


Figure 2. Time series of currents (+ means flood, - means ebb), SPM concentration and SPM transport.

The suspended particulate matter (SPM) concentration was derived from the OBS probes. The probes were calibrated in laboratory, where pairs of OBS readings and water samples were taken synoptically from a bucket. The concentration was gradually increased from a bulk solution produced with bottom sediments of the study area. The SPM concentration from the water samples were obtained by gravimetric procedure. Therefore, the OBS observations during the campaigns were limited in time to the tidal surveys. To build a wider view of SPM dynamics throughout the time, the acoustic backscatter recorded by the ADCP was used to estimate the vertical and temporal distribution of SPM. The use of Acoustic BackScatter (ABS) from current profilers has become a powerful tool in assessing the dynamics of fine sediments in coastal areas (Gartner, 2004; Schettini and Zaleski, 2006; Zaleski and Schettini, 2006). Using the sonar equation, the acoustic backscatter given in db is

$$ABS = TP + 20\log_{10}(R) - 2\alpha_W(R) + 20R\int \alpha_P dr \qquad (1)$$

where $TP$ is the transmitting acoustic pulse from the instrument. The second term on the right side is the geometrical correction for the conical shape of the acoustic beam, where $R$ is the distance from the transducer. The third term accounts for the water attenuation, and the last term accounts for the sound attenuation caused by the particles in the water (e.g., sediments). The last term, in relatively low sediment concentrations, presents a small role in the sound attenuation (Gartner, 2004). Thus, the ABS becomes mainly a function of the sound source, geometrical correction and water dissipation. Applying Equation 1 over the valid cells recorded by the ADCP produces a water column normalized acoustic behavior which can be related to the SPM.

The conversion of ABS to SPM was made using the OBS records which were later converted to SPM. The conversion curve has been defined using the OBS data acquired during the spring tidal survey at site #A. The OBS data is referenced to the surface; meanwhile the ABS records are referenced to the bed. In order to relate the OBS and ABS data, the matrixes were rescaled to produce equally time and vertical spaced observations. The equation that best fit the relationship is given by

$$NTU(ABS) = 0.072\, e^{(0.12 ABS)} \qquad (2)$$

with a correlation coefficient of $r^2 = 0.76$.

## Results and discussion

The time series of depth averaged currents, SPM concentration and SPM transport are presented in Figure 2. The flooding currents and transport were assigned as positive, and ebbing currents and transport were assigned as negative. The currents presented clear synodical modulation between neap and spring tide periods. The currents ranged from $-0.5$ to $+0.5$ m $s^{-1}$ during neap tide, and from $-1.0$ to $+0.8$ m $s^{-1}$ during spring tide. The increasing asymmetry from neap to spring is explained by the changing in the water storage in the intertidal areas, associated to the deeper channels morphology (Speer et al., 1990). The Caravelas estuary main channel along its first 10 km presents depths of around 10 m, and there are large mangrove forests in the entire systems, indicating the extensive intertidal areas. Residual currents were of the order of 0.04 m $s^{-1}$ during neap tide and $-0.02$ m $s^{-1}$ during spring tide. Taking into account that the system is interconnected to a second inlet which is also tide dominated, this change in residual currents seems to be related to non-linear behavior of tide as function of tidal height and/or harmonic interactions. Although, the results show that during neap tide the fluxes are to the Nova Viçosa inlet, while during spring tide the fluxes are directed to the Caravelas inlet.

The MPS concentration also presented clear synodical modulation, ranging from ~20 to ~100 mg $l^{-1}$ at neap and spring tide, respectively. During spring tides there are concentration peaks of up to 180 mg $l^{-1}$, which occurred only during flood periods. The instantaneous MPS transport, given by the product of MPS concentration and velocity, was also strongly modulated by the tidal period, being nearly symmetric. During neap tide the transport was of the order of 0.03 kg $m^{-2}$ $s^{-1}$, and during spring tide it was of the order of 0.1 kg $m^{-2}$ $s^{-1}$. On the other hand, residual transport was null during neap tide and consistently positive during spring tide. This result seems to contradict the currents results, which indicated ebb dominance at tidal frequency, and ebb residual at sub-tidal frequency. Therefore, the fine sediment dynamics must be interpreted under a wider view than only the estuary itself.

The synodical modulation of the MPS concentration can be firstly explained by the variation in yield shear stress. The increase of MPS concentration is a direct function of the increase of current intensity. On the other hand, the explanation for the higher concentration observed during the floods when the higher velocities occur during the ebbs can be attributed to the advection of MPS from the inner shelf. The distance of the site of measurements to the inner shelf is nearly 7 km. The tidal excursion, calculated by the integration of mean flood velocity ranges from 6 km during neap to 15 km during spring tide. Taking to account that the river supply of sediments to the Caravelas estuary is negligible, the main source of material will be the inner shelf. Additionally, the availability of SPM in the inner shelf waters will be a function of tides, but mainly to waves and indirectly to the wind regime, and the sub-tidal shelf currents. These factors may be the explanation for the peaks of SPM observed during flood periods, which occur when the tidal excursion is long enough to displace materials from the shore until the site of observation. The smaller concentrations and absence of peaks during the ebbs can be attributed to the sediment trapping on the intertidal areas.

## Conclusions

- Currents are symmetric during neap tide, and ebb dominant during spring tide.
- Residual currents are positive (flood) during neap tide, and negative (ebb) during spring tide, indicating changing of the exchanges between the inlets.
- MPS concentration is modulated by synodical cycle, and residual MPS transport is landwards during spring tides.
- The main source of SPM is the inner shelf.

## References


Gartner, J.W. (2004), Estimating suspended solids concentration from backscatter intensity measured by acoustic Döppler current profiler in San Francisco Bay, California, *Marine Geology*, 211, 169–187.

Schettini, C.A.F., Zaleski, A.R. (2006), A utilização de perfiladores acústicos de corrente por efeito Doppler na determinação do material particulado em suspensão na água: aplicações, *Revista Brasileira de Recursos Hídricos*, 11(3), 201–208.

Speer, P.E., Aubrey, D.G., Friedrichs, C.T. (1990), Nonlinear hydrodynamics of shallow tidal inlet/bay systems. In: Parker, B.B. (Ed.) *Tidal hydrodynamics*. New York, John Wiley & Sons, p321–339.

Zaleski, A.R., Schettini, C.A.F. (2006), Procedimentos para calibração de perfiladores acústicos de corrente por efeito Doppler para a determinação da concentração do material particulado em suspensão na água, *Revista Brasileira de Recursos Hídricos*, 11(3), 191–200.

# Frontogenesis in a highly stratified estuary

W. ROCKWELL GEYER[1], DAVID K. RALSTON[1], MALCOLM SCULLY[1, 2], JAMES A. LERCZAK[3]

1. Woods Hole Oceanographic Institute, 266 Woods Hole Road,
Woods Hole MA 02543-1050, USA
email: rgeyer@whoi.edu, dralston@whoi.edu, mscully@whoi.edu

2. Center for Coastal Physical Oceanography, Old Dominion University,
Norfolk VA 23529-0001, USA

3. College of Oceanic and Atmospheric Sciences, Oregon State University,
104 COAS Administration Building, Corvallis OR 97331-5503, USA
email: jlerczak@coas.oregonstate.edu

*Keywords: estuarine fronts, frontogenesis; Merrimack River, USA*

## ABSTRACT

Observations and modeling of the Merrimack River provide vivid illustration of frontogenesis and its consequences for estuarine dynamics. Although flood-tide fronts have dramatic surface manifestations, ebb-tide fronts are more important for dynamics and mixing. Ebb-tide fronts preferentially occur at distinct locations in the estuary, just upstream of the major expansions. Multiple fronts occur through the course of the ebb, first at the landward limit of the salt intrusion, with new fronts developing at more seaward locations through the course of the ebb. If the outflow is strong enough, the only front remaining at the end of the ebb is the 'lift-off' front at the mouth of the estuary. The fronts typically persist for several hours, with a quasi-steady momentum balance roughly consistent with Armi-Farmer theory. Mixing driven by baroclinically driven shear within the frontal zone is found to be a major fraction of the total estuarine mixing. In the late stage of the frontal evolution, the baroclinic pressure gradient is weakened, boundary mixing takes over, and the density structure is wiped out at one frontal location, reinforcing the gradients at the next downstream frontal location.

## Introduction

Estuarine fronts have been recognized and documented in a number of studies (see Largier, 1993 and O'Donnell, 1993 for reviews). Armi and Farmer (1986) provide a quasi-steady theory for fronts in two-layer exchange flows, with particular relevance to estuaries, as elucidated by Largier (1992). A number of studies have examined mixing associated with fronts, with particular emphasis on hydraulic transitions (Partch and Smith, 1978; Farmer, 1985). The actual process of creating fronts, or 'frontogenesis', has received far less attention, however. Simpson and Linden (1989) used the term in reference to tidally modulated exchange flow, but they did not consider spatial variability. The problem of particular relevance to estuaries and fjords is frontogenesis that occurs in regions of topographic variations. That is the focus of this paper.

The Merrimack River estuary provides a clear example of frontogenesis in regions of topographic variation. Observations as well as numerical model results provide the basis for the analysis of the frontogenesis process and the subsequent evolution of the frontal regime, including the associated mixing processes and ultimate erosion and demise of the frontal structure.

## Methods

Measurements of the estuarine salinity structure and velocity in the Merrimack River were obtained during different discharge conditions in 2005. The salinity was measured with a continuously profiling, towed conductivity-temperature-depth (CTD) sensor. Velocity was measured with a 1.2 MHz shipboard acoustic Doppler current profiler (ADCP). These measurements were used to identify fronts and to quantify their temporal evolution. Turbulence measurements were obtained within selected frontal features during high-flow conditions in May 2007. These measurements included micro-conductivity measurements and high-frequency velocity measurements using acoustic Doppler velocimeters. The turbulence-resolving instruments were mounted on a 10-m-long mast deployed from the side of the research vessel.

Numerical simulations of the Merrimack River were conducted using the FVCOM model (Chen and et al., 2003). The unstructured grid allowed detailed resolution of the complex bathymetry. The simulations used realistic forcing corresponding to the observation periods. Both the observations and model results were used to quantify the dynamics of frontogenesis and the associated mixing processes.

## Results

The field observations from the Merrimack reveal a highly time-dependent salt-wedge structure, with a general similarity to the Fraser River (Geyer and Farmer, 1989) but with stronger and more numerous frontal features (Figure 1). A pronounced surface front occurs during the flooding tide just landward of the mouth. This is a tidal intrusion front, as described by Nunes and Simpson (1980). It persists through the flood and is advected out of the estuary during the early ebb. Although the tidal intrusion front has a distinct surface expression (typically accumulating foam and flotsam), it does not have a strong dynamical influence, due to its limited vertical penetration.

At the landward end of the salt intrusion is the salt-wedge front, which extends through a significant fraction of the water column and makes a significant contribution to the pressure gradient. This front propagates into the estuary during the flood, maintaining a sharp leading edge but spreading out and weakening due to entrainment into the bottom boundary layer (Chant et al., 2007).

During the early ebb (Figure 1, 3rd panel), the salt wedge no longer advances, but neither does it retreat. Rather, it evolves into a sequence of fronts, each of which forms at a location of abrupt lateral expansion. There are three prominent expansions in the Merrimack estuary, one at −8 km, one at −5 km, and the most pronounced expansion occurring at the mouth. Early in the ebb, the most intense front is at the most landward location, and as the ebb progresses, the downstream fronts become more prominent, and the landward fronts get mixed out. At the end of the ebb, the only remaining front is the one at the mouth, which MacDonald and Geyer (2005) call the 'lift-off' front that forms the landward limit of the river plume.

## Discussion

*Dynamics of frontogenesis*

The transition that occurs in the early ebb from a relatively continuous salinity intrusion to a sequence of fronts provides an interesting case study in frontogenesis. As in Armi and Farmer (1996), the regime can be described using the framework of two-layer hydraulics. Unlike Armi and Farmer's analysis however, the time-dependent evolution of the density structure and mixing across the salinity interface are essential ingredients to the frontogenesis problem.

At the beginning of the ebb, there is a relatively uniform tilt to the interface, but as the ebb velocity increases, the slope of the interface increases in the expansions due to the convergence of the barotropic outflow

$$\frac{\partial}{\partial t}\frac{\partial h_i}{\partial x} = -\frac{\partial \bar{u}}{\partial x}\frac{\partial h_i}{\partial x}\,. \tag{1}$$

This barotropic convergence is a linear process, so it in itself does not lead to amplification of the gradient (i.e., frontogenesis). However, the increased interfacial slope contributes a baroclinic pressure gradient that retards the flow in the lower layer, which augments the convergence and steepening of the interface. This baroclinic process is nonlinear, so there is an amplification of the slope as the baroclinic gradient intensifies. The steepening is ultimately limited by the energetics of the upper layer: the thinning of the upper layer requires an acceleration, which leads to a hydraulic transition and supercritical flow within the expansion. Thus the flow evolves into the hydraulic transition described by Armi and Farmer (1986) for the flow through a constriction.

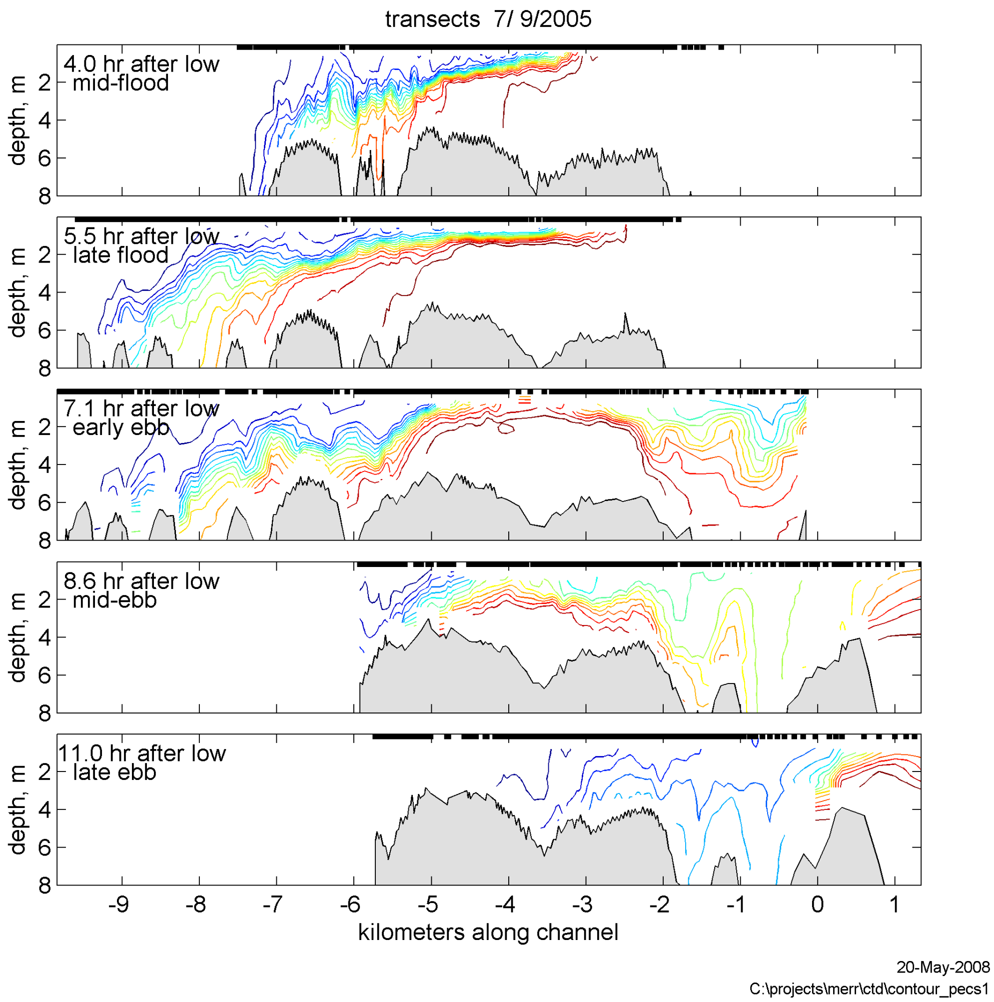


Figure 1. A sequence of salinity sections along the Merrimack during different tidal conditions, indicating different types of fronts. The green ovals indicate the tidal intrusion front. The red circles indicate the salt-wedge front. The black circles indicate ebb-tide fronts, each associated with a lateral expansion of the channel. The salinity contour interval is 1 psu.

A quasi-steady hydraulic transition is maintained for a portion of the ebb (e.g., Figure 1, 3rd panel, around 5 km), but as the ebb flow increases, the flow upstream of the expansion becomes supercritical. This flow is unstable both with respect to shear instabilities and with respect to long-wave disturbances, and the stratified flow landward of the front gets mixed away. The front thus becomes the leading edge of the salt wedge.

The final phase of the frontal evolution occurs when the barotropic flow becomes so strong that the front collapses and migrates seaward. It keeps moving seaward until it reaches a zone of increasing depth, at which it re-establishes a quasi-steady frontal regime. In this regime, the baroclinicity is not important to the maintenance of the front, as the isopycnals are nearly horizontal. Rather, the front is maintained as a flow-separation due to the sloping bathymetry, stabilized by the strong stratification. This regime eventually decays due to shear-induced mixing across the pycnocline. As each front along the estuary is mixed out, the density gradient of the next downstream front is reinforced. The last remaining front is the plume lift-off front, residing just seaward of the mouth bar.

*Influence of fronts on mixing*

The rate of mixing by different processes was quantified through the use of the FVCOM model, confirmed by local turbulence measurements. This analysis indicates that the frontal zones result in a disproportionate fraction of the mixing within the estuary. Most of the mixing occurs during the ebb, and it mainly associated with shear instability within the highly sheared interfacial zone. During the early and middle phases of the frontal zone evolution, the shear is mainly generated by the baroclinicity of the tilting interface. During the late phase, the shear is mainly associated with the wake dynamics of the separated flow, with little contribution from baroclinicity. Very high dissipation rates occur in the frontal zone due to the combination of moderate stresses and high shears. Buoyancy fluxes are commensurate, with flux Richardson numbers of about 0.15, consistent with Osborn (1980).

## References


Armi, L. Farmer, D.M. (1986), Maximal two-layer exchange through a contraction with barotropic net flow, *Journal of Fluid Mechanics*, 164, 27–51.

Chant, R.J., Geyer, W.R., Houghton, R., Hunter, E., Lerczak, J. (2007), Estuarine boundary layer mixing processes: insights from dye experiments, *Journal of Physical Oceanography*, 37, 1859–1877.

Chen, C., Liu, H., Beardsley, R.C. (2003), An unstructured grid, finite-volume, three-dimensional, primitive equations ocean model, *Journal of Atmospheric and Oceanic Technology*, 20, 159–186.

Farmer, D.M. (1985), Hydraulic control of flow over the sill in Observatory Inlet, *Journal of Geophysical Research*, 90, 9051–9068.

Largier, J.L. (1992), Tidal intrusion fronts, *Estuaries*, 15, 26–39.

Largier, J.L. (1993), Estuarine fronts: How important are they? *Estuaries*, 16, 1–11.

MacDonald, D.G., Geyer, W.R. (2005), Hydraulic control of a highly stratified estuarine front, *Journal of Physical Oceanography*, 35, 374–387.

O'Donnell, J. (1993), Surface fronts in estuaries: A review, *Estuaries*, 16, 12–39.

Osborn, T.R.J. (1980), Estimates of the local rate of vertical diffusion from dissipation measurements, *Journal of Physical Oceanography*, 10, 83–89.

Partch, E.N., Smith, J.D. (1978), Time dependent mixing in a salt wedge estuary, *Estuarine and Coastal Marine Science*, 6, 3–19.

Simpson, J.H., Nunes, R.A. (1981), The tidal intrusion front: An estuarine convergence zone, *Estuarine, Coastal and Shelf Science*, 13, 257–266.

Simpson, J.E., Linden, P.F. (1989), Frontogenesis in a fluid with horizontal density gradients, *Journal of Fluid Mechanics*, 202, 1–16.

# Frontogenesis at the shoal/channel interface in a macro and mesotidal estuary

SARAH N. GIDDINGS[1], DEREK A. FONG[1], STEPHEN G. MONISMITH[1], MARK T. STACEY[2]

1. Environmental Fluid Mechanics Laboratory, Civil and Environmental Engineering, Stanford University, Stanford CA 94305-4020, USA
email: sarahgid@stanford.edu, dfong@stanford.edu, monismith@stanford.edu

2. Civil and Environmental Engineering, University of California Berkeley, 665 Davis Hall, Berkeley CA 94720-1710, USA
email: mstacey@berkeley.edu

*Keywords: fronts, frontogenesis, shoal, convergence, secondary circulation*

## ABSTRACT

The hydrodynamic interactions between shoals and channels in estuarine systems are critical to overall system dynamics driving physical processes that impact biological and chemical transport such as the evolution of phytoplankton blooms. Fronts caused by and interacting with shoal/channel exchanges play an important role in these processes. Mechanisms of shoal/channel interaction induced frontogenesis are examined utilizing field data collected in two different estuaries, the Snohomish River Estuary, in Everett, WA and South San Francisco Bay, near Redwood City, CA. The Snohomish River Estuary is a shallow, macrotidal, salt-wedge estuary with extensive intertidal mudflats. South San Francisco Bay is a mesotidal, well-mixed estuary with a deeper channel flanked by more uniform intertidal mudflats. Several moorings with bottom mounted acoustic Doppler current profilers (ADCP); acoustic Doppler velocimeters (ADV); pressure sensors; and conductivity, temperature, depth (CTD) sensors at varying depths were deployed for over 20 days in both the Snohomish River and South San Francisco Bay Estuaries. The mooring information was augmented with high resolution 30-hour ADCP and CTD transecting surveys during representative spring and neap tidal periods as well as continuous infrared and visual remote sensing. Frontogenesis mechanisms at the shoal/channel interface are compared in these two systems. Different mechanisms appear to be acting in each system particular to the type of estuary; however lateral baroclinic forcing is important in both systems. Based on our observations, we hypothesize that frontogenesis and shoal/channel interactions influence transport and mixing and residual circulations in these systems.

## Introduction

Intertidal and shoal regions are prevalent in estuarine systems. The importance of these regions from a biological/ecological perspective has been studied extensively. Less well studied is their role in the overall system dynamics and the physical interactions that occur at shoal/channel boundaries. In this study, we focus on transverse circulations and frontogenesis at the shoal/channel interface. Fronts have been associated with the transport and aggregation of pollutants, floating material (debris, larvae, etc.), phytoplankton, and higher trophic level organisms (e.g., Largier, 1993). Fronts formed at the shoal/channel interface will modulate exchange between the shoals and channels.

Previous research in South San Francisco Bay has shown that the hydrodynamic connectivity between shoals and channels may play a critical role in phytoplankton dynamics as phytoplankton grows preferentially over the shallow regions (Lucas et al., 1999; Lucas et al., 2007). Understanding mechanisms for shoal/channel exchange and frontogenesis will allow us to better understand how phytoplankton may be transported to the main channel and the rest of the San Francisco Bay system. Understanding these interactions in estuarine systems is critical to understanding transport of phytoplankton, sediment, and pollutants.

Past research has examined the role of complex geometry in creating transverse circulations, frontogenesis, and altering mixing (e.g., Li and O'Donnell, 1997; Valle-Levinson et al., 2000). This work aims to further explore frontogenesis mechanisms in two disparate estuarine systems and explore the importance of shoal/channel induced frontogenesis on transport between shallow and deep regions in estuaries.

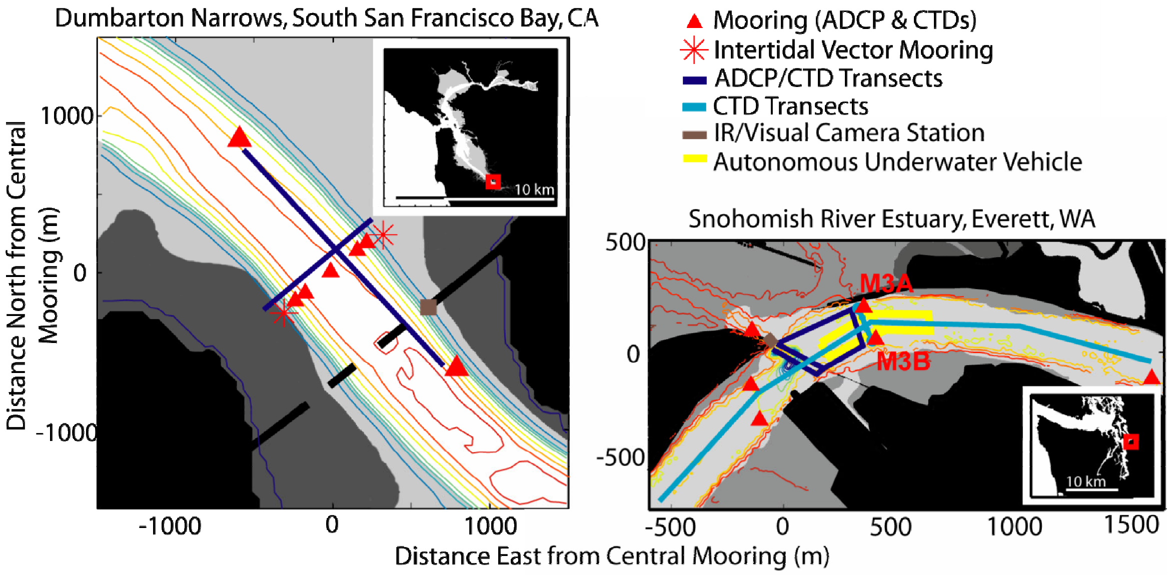


Figure 1. Experimental layouts for South San Francisco Bay January 2008 deployment (left) and Snohomish River Estuary June 2006 deployment (right). Dark and intermediate gray areas are intertidal and shallow while white is greater than 5 m below mean lower low water. Contours are drawn every 2 m.

## Methods

Mechanisms of shoal/channel interaction induced frontogenesis are examined utilizing field data collected in two different estuaries, the Snohomish River Estuary, in Everett, WA and South San Francisco Bay, near Redwood City, CA. The Snohomish River Estuary is a shallow (3 m below mean lower low water), macrotidal, salt-wedge estuary with extensive intertidal mudflats. South San Francisco Bay is a mesotidal, well mixed estuary with a deeper channel (15 m below mean lower low water) flanked by more uniform intertidal mudflats. In 2006, six moorings with bottom mounted acoustic Doppler current profilers (ADCP); acoustic Doppler velocimeters (ADV); pressure sensors; and conductivity, temperature, depth (CTD) sensors at several depths were deployed for over twenty days in the Snohomish River Estuary (see Figure 1 below). In February 2008, nine similar moorings were deployed in Far South San Francisco Bay for 30 days (Figure 1). During both experiments, the mooring information was augmented with high resolution 30-hour ADCP and CTD transecting surveys during representative spring and neap tidal periods as well as continuous infrared (Snohomish River Estuary only) and visual remote sensing.

Using principle axis analysis to define the along and across channel coordinates, transverse circulations can be examined with both the mooring and transect data. Combining this information with density derived from the CTDs, we can start to identify fronts and explore frontogenesis mechanisms in these systems. The visual remote sensing helps corroborate the presence of fronts via visible surface signatures. Analyzing terms in the transverse momentum equation and general circulation patterns, frontogenesis mechanisms at the shoal/channel interface are compared in these two systems.

## Results

Visual and Infrared observations confirm the development of a strong convergence front during flood tide after lower low water during all tides except the smallest neap tide in the Snohomish River Estuary. The infrared imagery shows warmer (lighter color) water coming from the mudflats converging with colder water coming upstream from the main channel (see Figure 2). The front is visible as a foam/debris line emanating from the tip of Jetty Island along the channel upstream to mooring M3B. Over the course of the flood tide, it moves across the channel towards mooring M3B. Transverse currents computed from the ADCP transects between moorings M3A and M3B show the development of two surface convergent circulation cells and their movement across the channel (Figure 2). The frontal surface convergence during the Spring tide survey is computed from the transect data $\delta v/\delta y = 0.019\ s^{-1}$ and a density difference across the front of 8 kg $m^{-3}$ over 5 meters ($\delta\rho/\delta y = 1.6$ kg $m^{-2}$) is observed (computed from transects with an underwater autonomous vehicle equipped with a CTD.)

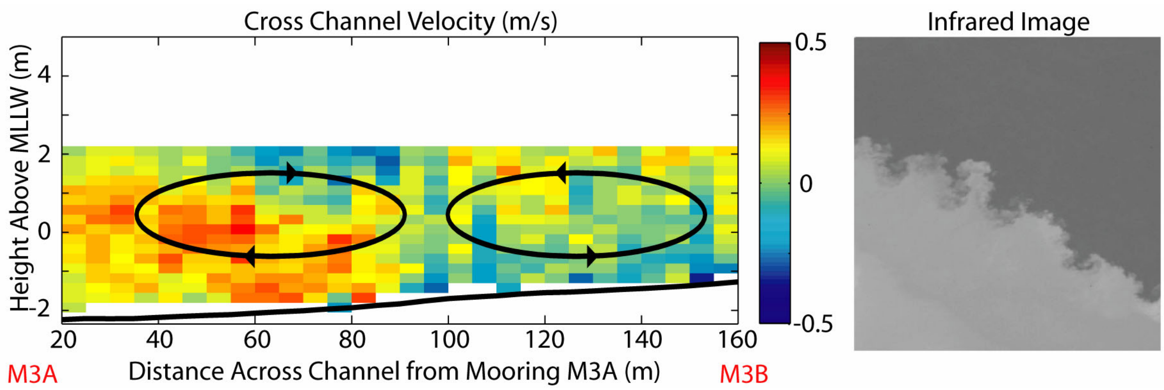


Figure 2. Cross channel velocity currents computed from cross channel ADCP transects during peak flood in the Snohomish spring survey. The infrared image (courtesy of Andy Jessup, personal communication) is taken at the same time corroborating the frontal presence and the strong thermal gradient across the front.

Observed fronts in South San Francisco Bay are more intermittent occurring both along the channel center and at the shoal/channel interface during varying tidal phases. The most repetitive frontal formation is a meandering convergence front along the Eastern shoal/channel interface developing at peak ebb and continuing through ebb until slack water. This front is associated with convergence at the surface at the shoal/channel interface as more dense water on the shoals converges and dives beneath less dense water in the main channel setting up a strong transverse circulation cell within the channel. Surface convergence during the frontal presence is $\delta v/\delta y = 0.002\ \mathrm{s}^{-1}$ and the density difference across the front reaches up to $2\ \mathrm{kg\ m}^{-3}$ over about 10 meters ($\delta\rho/\delta y = 0.2\ \mathrm{kg\ m}^{-2}$). The frontal strength (convergence and density gradient) is highest during two anomalous events that may potentially be due to wind driven circulation.

Scaling the transverse momentum equation (below) using data from the moorings and transects to estimate the maximum contribution of each term, the dominant terms $O(10^{-3})$ in the Snohomish are the baroclinic, centrifugal, barotropic and friction terms in decreasing magnitude. In South San Francisco Bay on the other hand, the barotropic and baroclinic terms dominate.

$$\underbrace{\frac{\partial u_n}{\partial t}}_{\text{acceleration}} + \underbrace{u_s\frac{\partial u_n}{\partial s}}_{\text{advection}} - \underbrace{\frac{u_s^2}{R_s}}_{\substack{\text{centrifugal}\\\text{(curvature)}}} + \underbrace{fu_s}_{\substack{\text{Coriolis}\\\text{(rotation)}}} + \underbrace{g\frac{\partial \eta}{\partial n}}_{\text{barotropic}} + \underbrace{\frac{g}{\rho_o}\left(\frac{\partial}{\partial n}\int_z^0 \rho(z')dz'\right)}_{\text{baroclinic}} - \underbrace{\frac{\partial}{\partial z}\left(A_z\frac{\partial u_n}{\partial z}\right)}_{\text{friction}} = 0. \tag{1}$$

In a purely curvature driven system without stratification, the centrifugal term is expected to be balanced by the barotropic pressure gradient and friction (Falcon, 1984; Kalkwijk and Booij, 1986). The Snohomish River Estuary has a small radius of curvature, $R_s$ ~800 m, such that we can expect curvature driven circulation to be important. However, despite the large centrifugal contributions, the lateral baroclinic term is strong enough that it can dominate the force balance. In South San Francisco Bay the channel is relatively straight so the centrifugal acceleration is not as important but again the lateral baroclinic forcing appears important.

Time series of ADCP and CTD transects confirm that the Snohomish River Estuary frontogenesis occurs via a trapping mechanism. Mid-density water trapped over the mudflats and later released into the flooding dense main channel water leads to a lateral baroclinic force that competes with curvature to form a consistent front along the center of the channel during flood tides after lower low water. As the flood tide decreases, the lateral baroclinic term dominates and the baroclinically driven circulation cell dominates as the front slumps across the inside bank. Similar to observations by Lacy et al. (2003) we observe that as the baroclinic force becomes dominant, the fresher water can propagate across the channel leading to enhanced vertical stratification at the inner bank and decreased vertical mixing. The stratification and vertical mixing along with the curvature induced circulation modulate the propagation of this front across the channel such that the propagation speed does not match that of a purely baroclinic front.

The frontogenesis mechanism in South San Francisco Bay is less clear. It appears to be caused by reversed differential advection during the ebb tide in which the along channel density gradient is advected downstream further in the channel than over the shoals leading to a density distribution with higher density over the shoals and lower density in the channel. Further analysis of CTD transects will aid to confirm this hypothesis. It is clear that curvature plays a much more minor role than in the Snohomish and we hypothesize that trapping is also less important. Additionally the larger scales of this system and weaker energetics allow for modulation via wind and precipitation events.

## Conclusions

The frontogenesis mechanisms observed in the Snohomish River Estuary and South San Francisco Bay are different as we expected for such different systems, yet there were several similarities. In both systems, the shoal/channel bathymetry interacts with the overall circulation patterns to create fronts. In both systems, the baroclinic force is important in driving transverse circulations and frontogenesis.

It appears that the type of estuary (well-mixed versus salt-wedge and macro versus mesotidal) plays an important role in creating transverse circulations and fronts. The salt-wedge nature of the Snohomish combined with the fact that its tidal range exceeds the mean depth allows for trapping and later convergence of two very different water masses. In South Bay, we hypothesize that the well-mixed nature of the system may play a role in modulating the lateral density gradients via a mechanism similar to differential advection. With decreased energetics and a larger system, South Bay is more susceptible to anomalous events such as wind driven circulation that can enhance frontogenesis and frontal persistence.

Overall, the front in the Snohomish River Estuary is more persistent and stronger than those in South San Francisco Bay however both clearly have important implications for transport in each system. In our future research, we will explore the interaction of this frontogenesis with transport. Suspended sediment and chlorophyll a concentrations were significantly higher on the shoalward side of the front in South San Francisco Bay and the front appears to modulate their transport into the channel. In the Snohomish, we found the trapping mechanism affects the residual circulation and longitudinal dispersion in the system therefore affecting transport of pollutants and other scalars. Further analysis of these data sets will illuminate these mechanisms further and help understand the different mechanisms that may occur in different systems and how they may modulate transverse mixing and the overall system dynamics.

## References


Falcon, M. (1984), Secondary flow in curved open channels, *Annual Review of Fluid Mechanics*, 16(1), 179–193.

Kalkwijk, J.P.T., Booij, R. (1986), Adaptation of secondary flow in nearly-horizontal flow, *Journal of Hydraulic Research*, 24(1), 19–37.

Lacy, J.R., Stacey, M.T., Burau, J.R., Monismith, S.G. (2003), Interaction of lateral baroclinic forcing and turbulence in an estuary, *Journal of Geophysical Research*, 108(C3), 3089–3103.

Largier, J.L. (1993), Estuarine fronts: How important are they? *Estuaries*, 16(1), 1–11.

Li, C., O'Donnell, J. (1997), Tidally driven residual circulation in shallow estuaries with lateral depth variation, *Journal of Geophysical Research*, 102(C13), 27915–27929.

Lucas, L.V., Koseff, J.R., Monismith, S.G., Cloern, J.E., Thompson, J.K. (1999), Processes governing phytoplankton blooms in estuaries. II. The role of horizontal transport, *Marine Ecology Progress Series*, 187, 17–30.

Lucas, L.V., Koseff, J.R., Monismith, S.G., Thompson, J.K. (2007), *Shallow water processes govern system-wide bloom dynamics: A modeling study*. (Manuscript in preparation.)

Valle-Levinson, A., Li, C., Wong, K., Lwiza, K.M.M. (2000), Convergence of lateral flow along a coastal plain estuary, *Journal of Geophysical Research*, 105(C7), 17045–17061.

# Density-driven circulation and the associated fluxes in a semi-enclosed shelf sea (the Seto Inland Sea, Japan)

SHIHO KOBAYASHI[1], HIROMU ZENITANI[2], TATEKI FUJIWARA[1]

1. Kyoto University, Kitashirakawaoiwake, Sakyo, Kyoto 606-8502, Japan
   email: shihok@kais.kyoto-u.ac.jp, fujiwara@kais.kyoto-u.ac.jp

2. National Research Institute of Fisheries and Environment of Inland Sea (FEIS), 2-17-5 Maruishi, Hatsukaichi, Hiroshima 739-0452, Japan
   email: zenitani@fra.affrc.go.jp

*Keywords: freshwater influence, density-driven circulation, Earth's rotation*

## ABSTRACT

In Regions of Freshwater Influence (ROFI; Simpson, 1997), lateral input of freshwater from coastal rivers often drives basin-scale circulations. The Seto Inland Sea, Japan, represents a semi-enclosed shelf sea connected to the ocean through two openings (Figure 1b). About 5 billion $m^3$ of freshwater per year flows into the sea and induces along-channel horizontal gradients of salinity and hence of density (Figure 1c). They may drive circulations and play an important role in shelf-ocean exchange. The structures of the circulations and their roles on dispersion, however, have not been fully elucidated.

In a basin located mid-channel in the Seto Inland Sea, Hiuchi-Nada, hydrographical surveys have been conducted from April to August since 2002 to present (Figure 2). In this study, the three-dimensional structure of the density-driven circulations and their dynamical properties are investigated using the results of the surveys and a diagnostic model.

## Methods

The source of freshwater to Hiuchi Nada is located at the eastern end of the basin (the locations of rivers are indicated by arrows with squares labeled with the number '1-1' and '1-2' in Figure 1b). Hourly river discharge and water-level data have been observed by the Ministry of Land, Infrastructure and Transport, and published annually.

From spring to summer since 2002, monthly hydrographic surveys have been carried out at 28 stations in and around Hiuchi Nada, using a conductivity-temperature-depth (CTD) profiler. The locations of the stations are plotted in Figure 2 and the dates of observation and stations are listed in Table 1. We also measured the flow field using a ship-mounted Acoustic Doppler Current Profiler (ADCP) in August 2006 by repeatedly profiling velocity for 25 hours on the section along line 'A' indicated in Figure 2.

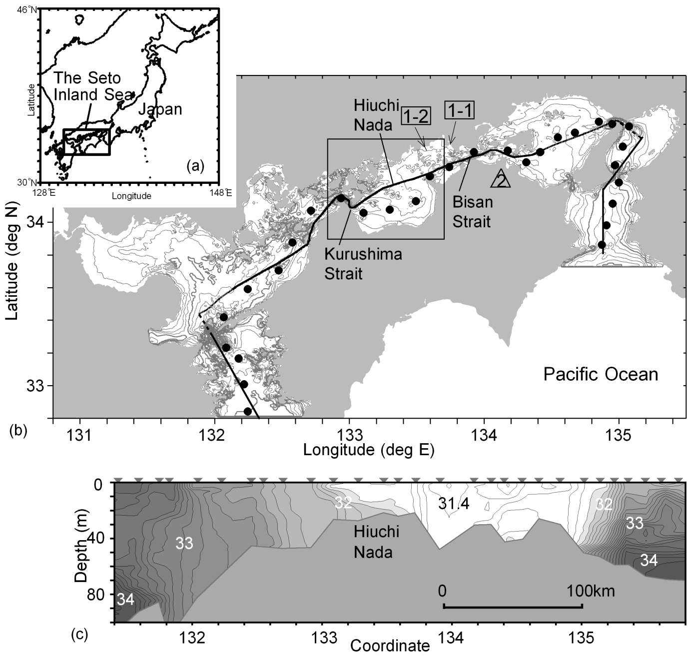


Figure 1. (a) Map of Japan. (b) Map of the Seto Inland Sea. The contours indicate water depth in meters (contour interval is 10 m). The points indicated by black circles are reflected on the axial line used for Figure 1c. (c) Axial section of salinity (psu) observed in August 2002.

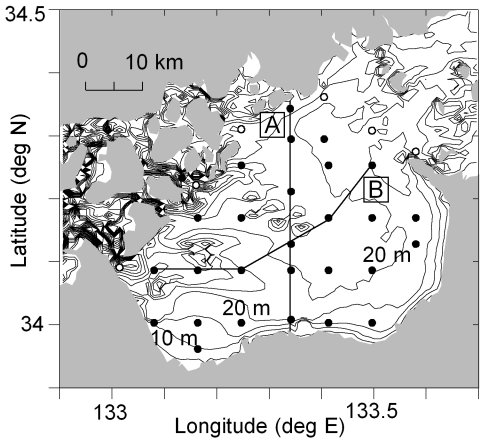


Figure 2. Bathymetry of the Hiuchi Nada study area. Circles show the location of CTD measurements and line 'B' indicates the axial section used in Figure 4. Line 'A' indicates the location of the cross-channel section surveyed by ADCP measurements used in Figure 6.

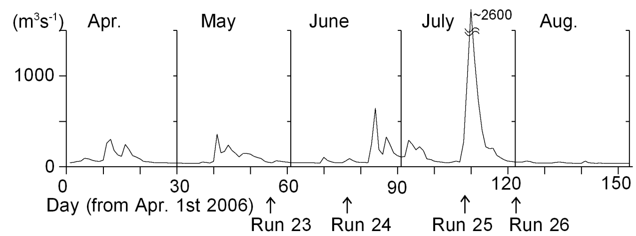


Figure 3. River discharge (m$^3$ s$^{-1}$) into Hiuchi Nada from 1 April to 31 August 2006.

Table 1. Dates of observations

| Run | Year | Date |
|---|---|---|
| Run 1 | 2002 | 15 - 19th April |
| Run 2 | 2002 | 7 - 11th May |
| Run 3 | 2002 | 27 - 31st May |
| Run 4 | 2002 | 13 - 17th June |
| Run 5 | 2002 | 28th June - 2nd July |
| Run 6 | 2002 | 15 - 19th July |
| Run 7 | 2002 | 5 - 9th August |
| Run 8 | 2003 | 17 - 21st April |
| Run 9 | 2003 | 7 - 11th May |
| Run 10 | 2003 | 21 - 25th May |
| Run 11 | 2003 | 11 - 18th June |
| Run 12 | 2003 | 27th June - 1st July |
| Run 13 | 2003 | 22 - 26th July |
| Run 14 | 2004 | 6 - 9th May |
| Run 15 | 2004 | 18 - 21st May |
| Run 16 | 2004 | 6 - 12th June |
| Run 17 | 2004 | 1 - 7th July |
| Run 18 | 2004 | 13 - 16th July |
| Run 19 | 2005 | 18 - 21st April |
| Run 20 | 2005 | 9 - 12th May |
| Run 21 | 2005 | 19 - 22nd May |
| Run 22 | 2005 | 6 - 9th June |
| Run 23 | 2006 | 25 - 27th May |
| Run 24 | 2006 | 15 - 17th June |
| Run 25 | 2006 | 17 - 19th July |
| Run 26 | 2006 | 1st - 2nd August |

A robust diagnostic method (Guo et al., 2004), which is appropriate for the calculation of residual currents in coastal waters on the basis of observed density, is used in this study. The model used here is a three-dimensional multi-level model developed by Fujihara and Kawachi (1995) and validated by several studies (e.g., Fujiwara, 2003). Based on the results, fluxes through the central section (the location is indicated as line 'A' in Figure 2) are calculated. Here, flux through each layer, $F$ (m$^2$ s$^{-1}$), and volume flux, $Q$ (m$^3$ s$^{-1}$), are defined as the following

$$F = \int_0^L u\,dy \qquad , \qquad Q = \int_{z_0}^{z_1} u\,dydz \tag{1}$$

where $u$ is velocity perpendicular to the section (m s$^{-1}$), is the direction along the section $y$ (m), is the depth coordinate $z$ (m) and $L$ is the width of the section at each layer (m). The range of integration for volume flux represented by $z_0$ and $z_1$ is defined as the depth-range where $F$ has positive value.

## Results and discussion

The river discharge from May to August in 2006 peaked on three occasions and with gradually increasing magnitude (Figure 3). A relatively large peak appeared before the observations in August. The axial sections of water temperature, salinity and density observed from May to August in 2006 along line 'B' (indicated in Figure 2) are shown in Figure 4. Stratification already existed in May, and increased toward August. A more substantial freshwater was supplied in the end of July, and in the beginning of August, horizontal gradients were intensified, with both salinity and density increasing westward and the corresponding isohalines and isopycnals sloped upward toward the west. On the horizontal plane, the relatively heavy water at the station located on the westernmost end, adjacent to the Kurushima Strait, expanded eastward along the southern coast (Figure 5).

Figure 6 shows the vertical distributions of the observed and modeled residual velocities. Those observed include tide- and wind- induced components and show more complicated structures than those modeled. The velocities indicated by 'ii' and 'iii' in Figure 6a are considered to be the components of anti-cyclonic circulation often observed in this region and of tidal residual currents around islands, respectively. Those modeled only express the components induced by density gradients, but the velocities indicated by 'i', 'ii' and 'iv' in Figure 6a are also shown in Figure 6b. The velocities along the southern coast ('i') are considered to indicate the intrusion of heavy water from Kurushima Strait toward east shown in Figures 4 and 5. It is

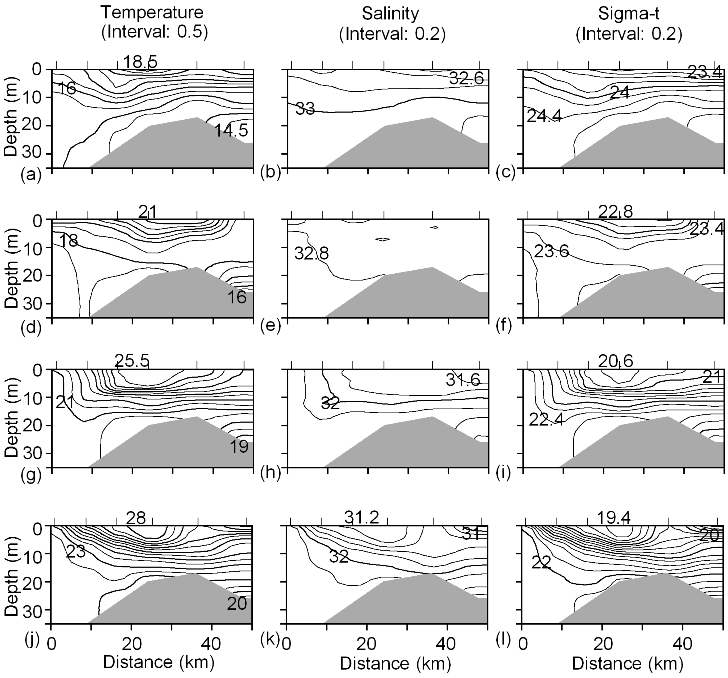


Figure 4. Axial sections along line 'B' (shown in Figure 2) of temperature (°C), salinity (psu) and sigma-t observed in May (a–c), June (d–f), July (g–i) and August (j–l) in 2006.

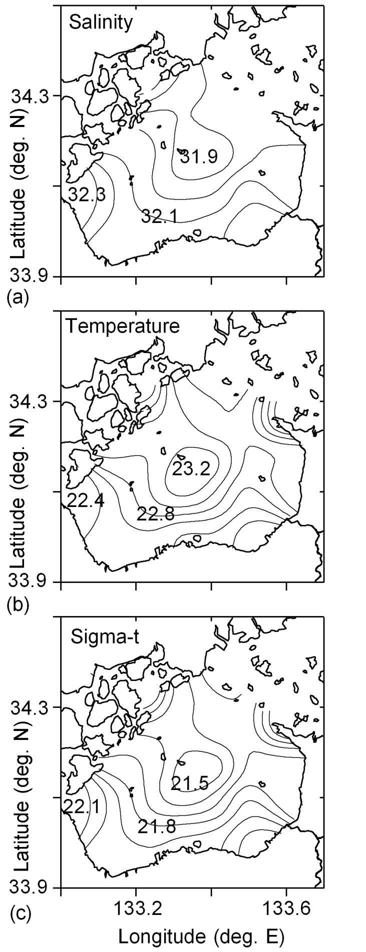


Figure 5. Horizontal distributions of (a) salinity (psu), (b) temperature (°C) and (c) sigma-t at 14 m depth observed in August 2006.

accompanied by the west-ward flow along the southern coast in the upper layer. The velocities along the northern coast ('iv') are also considered to indicate the intrusion of light water from Bisan Seto toward west through the upper layer. The fluxes through each layer (F) were estimated by averaging those residual velocities in transverse direction. Velocities associated with the horizontal circulations were cancelled out, but the transports above approximately 10 m were directed westward, while those below this depth were directed eastward (Figure 7).

The relationship between these fluxes ($Q$ m$^3$ s$^{-1}$) and mean river discharge ($R$ m$^3$ s$^{-1}$) (the locations of rivers are indicated by arrows with squares labeled with the number '1-1' and '1-2' in Figure 1b) is shown in Figure 8. The plots are the results from similar estimations described above, which were applied to the dataset from 2002 to 2005 in addition to that from 2006. The river discharge was averaged in the period from the 20 days before the observation date to the first day of the observation. The increase in the volume fluxes closely corresponded to the increase in freshwater supply. The relationship between the volume fluxes and river discharge was the following

$$Q = 438 + 31.4 \times R^{2/3}. \qquad (2)$$

The determination coefficient was 0.56 and P-value was 0.004 (< 0.01), indicating that the relationship was significant.

## Conclusions

From the results of the observations in the mid-channel in the Seto Inland Sea, the volume fluxes associated with two-

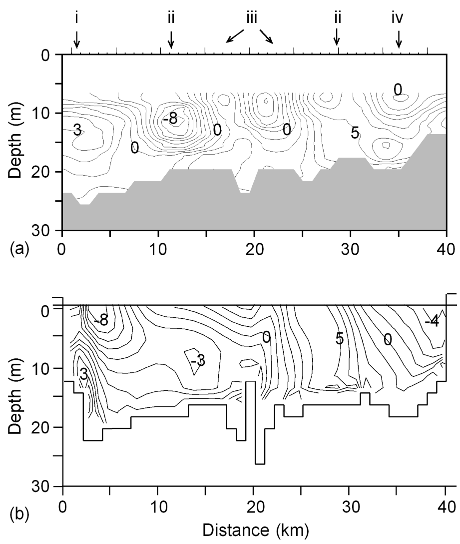


Figure 6. Vertical sections of residual velocities derived from (a) the temporal variation of currents observed on 1–2 August 2006; and (b) the results of the diagnostic model. The location of the section is indicated by line 'A' in Figure 2. Values are positive eastwards and negative westwards.

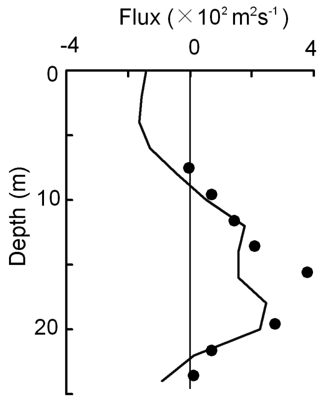


Figure 7. Vertical profiles of the fluxes through each layer along the line 'A' (shown in Figure 2) in August 2006. Values are positive eastwards and negative westwards.

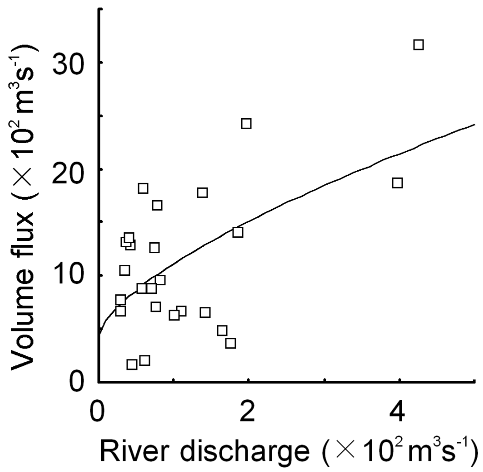


Figure 8. The relationship between river discharge ($R$) and volume fluxes ($Q$) which are estimated using the data of each observation from 2002 to 2006 listed in Table 1. $R$ and $Q$ are defined in the text.

layered exchange flow which varies as the ⅔-power of the river discharge into one end of the basin were obtained. The regions of salinity and density anomaly associated with the dense or light water inflow were found along the coast. It is considered that flows like a plume are driven by horizontal density gradient and they evolve into a coastal current which flow along the coast to the right by the influence of the earth's rotation.

## Acknowledgements

ADCP observations on the 1–2 August 2006 were conducted in collaboration with Yuge National College of Marine Technology. We are indebted to Dr. Mitsuo Tada, Dr. Hideshi Tsukamoto and the captain and crews of the Training Vessel Yugemaru for their support. Monthly hydrographic observations from 2002 to 2006 were conducted by Research Institute of Fisheries and Environment of Inland Sea (FEIS). The authors are indebted to Dr. Naoaki Kono, Dr. Youichi Tsukamoto and the captain and crews of the R.V. Shirafujimaru for their support.

## References

Fujihara, M., Kawachi, T. (1995), An adaptation of diagnostic numerical model of residual current to Bungo Channel, Japan, *The Japanese Society of Irrigation, Drainage and Reclamation Engineering*, 180, 75–84.

Fujiwara, T. (2003), Buoyancy-driven current during cooling periods, *Journal of Geophysical Research*, 108(C8), 3276, doi:10.1029/2002JC001521.

Guo, X., Futamura, A., Takeoka, H. (2004), Residual current in a semi-enclosed bay of the Seto Inland Sea, Japan, *Journal of Geophysical Research*, 109, C12008, doi:10.1029/2003JC002203.

Simpson, J.H. (1997), Physical processes in the ROFI regime, *Journal of Marine Systems*, 12, 3–15.

# Influence of freshwater runoff on salinity and suspended particulate matter dynamics in the Elbe Estuary, Germany

JENS KAPPENBERG

Institute for Coastal Research, GKSS Research Centre, Max-Planck-Straße 1,
21502 Geesthacht, Germany
email: jens.kappenberg@gkss.de

*Keywords: estuarine turbidity maximum, sediment dynamics, mixing processes*

## ABSTRACT

The effects of freshwater runoff on the distribution of salinity and suspended particulate matter (SPM) in the Elbe Estuary are analyzed on the basis of measurements from 1979 to 2007.

### Database and instrumentation

The measurements comprise of longitudinal transects of 28 near surface samples taken at full ebb current (ARGE Elbe) from a helicopter. Between 1980 and 1990 these transects were performed monthly, but today the frequency has been reduced to six per year.

A second source of data are 5-minute interval time-series of current, temperature and salinity measurements at six stations (Figure 1) in operation since 1997 to monitor the effects of the last deepening of the navigation channel (Portal Tideelbe). Since 2006 these Aanderaa current meters have been equipped with turbidity sensors.

### Results

All available data show a clear response of the mixing zone between saltwater and freshwater and the SPM in the estuarine turbidity maximum (ETM) to river floods. The mixing zone and the ETM located in the low salinity region of the mixing zone are almost instantaneously swept down-estuary as soon as the runoff exceeds a critical level of some 1000 m$^3$ s$^{-1}$ (long-term average of the Elbe runoff: 720 m$^3$ s$^{-1}$). From the transect data before and after the river flood estimates of the loss of material from the ETM can be derived which amount up to 80% of the pre-flood inventory.

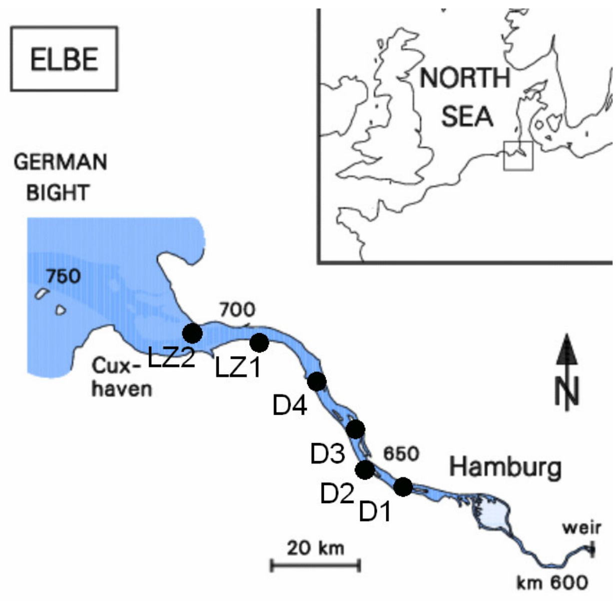


Figure 1. Positions of long-term measurement stations along the Elbe Estuary. Numbers (650, 700, 750) denote river kilometers

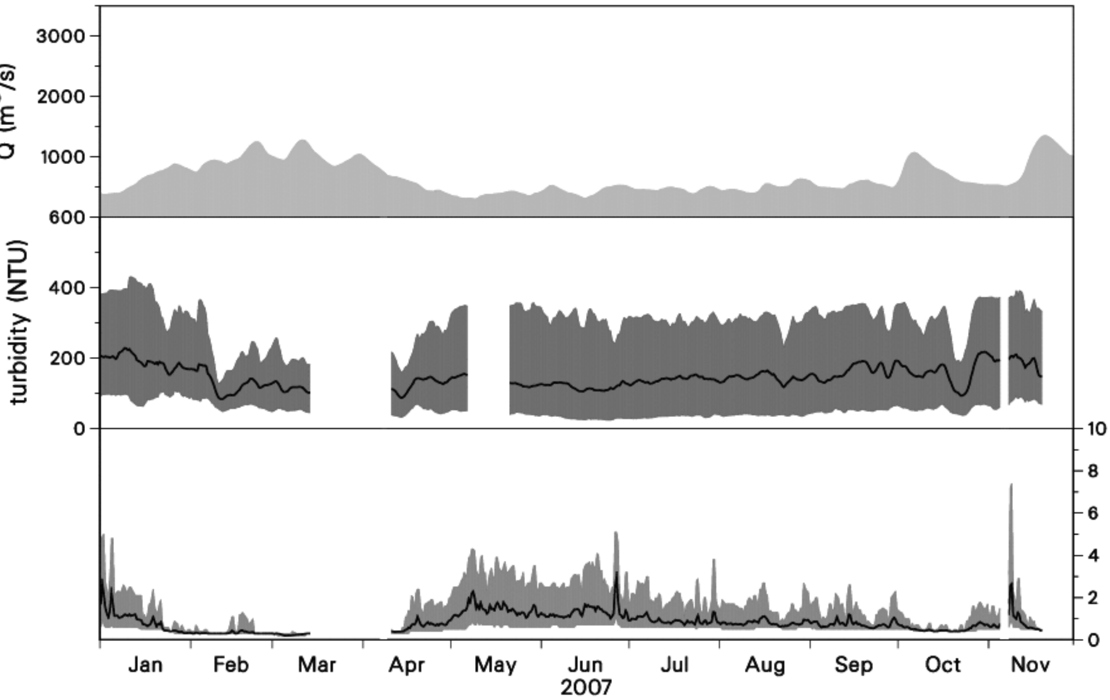


Figure 2. Annual variations of runoff $Q$ (daily values), near bottom turbidity and salinity $S$ at station D4 (shaded areas: intratidal variation, solid lines: tidal means).

After river flood in Summer 2002 (duration 28 days, freshwater inflow to the estuary: $4.8 \times 10^9$ m$^3$, peak runoff: 3410 m$^3$ s$^{-1}$) a pronounced ETM could still be observed while in Spring 2006 a runoff event (duration 48 days, freshwater inflow to the estuary: $8.2 \times 10^9$ m$^3$, peak runoff: 3602 m$^3$ s$^{-1}$) flushed the ETM inventory into the sea. Since in 2002 no turbidity measurements were available and due instrument failures at most of the stations in Spring 2006 changes in the intratidal SPM variation during the flood could only be analyzed at station D1 during the 2006 event. In 2007 and 2008 only comparatively weak runoff events with peak values below 2000 m$^3$ s$^{-1}$ occurred which could be observed at all stations and show the influence of the runoff on turbidity and salinity (Figure 2).

While the reaction of both the mixing zone and the ETM to a rising river flood is fast, the restoration of the ETM to its pre-flood position and the refilling of its inventory can take several months. In contrast the time for re-establishment of the mixing zone at its former position is much shorter.

## References


ARGE Elbe (1979–2006), Wassergütedaten der Elbe von Schnackenburg bis zur See, www.arge-elbe.de/wge/Download/Ddaten.php.

Portal Tideelbe (1997–2007), Wasser- und Schifffahrtsverwaltung des Bundes, www.bs-elbe.de/html/Main-Seite/.

# 2, 4, 7, 8 and $F = 1$: The role of internal hydraulics and geomorphology in shaping an estuarine superfund site

ROBERT J. CHANT

Institute of Marine and Coastal Sciences, Rutgers University, 71 Dudley Road,
New Brunswick NJ 08901-8521, USA
email: chant@imcs.rutgers.edu

*Keywords: tides, river flow, estuarine circulation; Passaic River, USA*

## ABSTRACT

The most contaminated and depositional system in the New York / New Jersey Harbor is the Passaic River (Figure 1). The intense industrial history in the Passaic's watershed is particularly intact in the lower 12 miles due to remarkably high sediment deposition rates in the past 60 years. The Harbor and its tributaries have been highly engineered to develop Port Elizabeth/Newark which lies just downstream of the Passaic River in Newark Bay (Figure 1). Prior to this engineering Newark Bay was a broad shallow system with depths generally less that 2–3 m deep with a deeper channel 3–4 m deep leading into the Hackensack River and a 5–8 m deep channel at its mouth leading into the Kill van Kull. The Harrison reach of the Passaic River, which is the focus of this paper, is shown on the 1845 NOAA chart to have mean low water depths of approximately three meters. River discharge in the Passaic has an annual mean of ~50 $m^3 s^{-1}$.

The engineering of this system commenced in the late 19th century and by 1940 the lowest 3–4 km of the Passaic River had been deepened to approximately 10 m and to 6–7 m up to river km 20. However, with the construction of Port Elizabeth in 1940 dredging on the Passaic River ceased as port activities became focused downstream. Today the mean low water depths of the channel are approximately 3–4 m. Both historical charts and geochemical evidence (Huntley et al., 1995) indicate a sedimentation rate of 5–10 cm $yr^{-1}$ over the past 60 years. During this highly depositional phase there has been intense industrial inputs along the Passaic River and many of the contaminants associated with these industries are contained in the sediment record.

Perhaps most notable among these contaminants are extremely high levels of 2,4,7,8-Tetracholrodibenzo-p-dioxin (2,3,7,8 TCDD) associated with the manufacturing of Agent Orange that occurred in the lower Passaic between 1948–1974 (Bopp et al., 1991) approximately 3 km from the mouth. Today a peak in dioxin levels lies 1–2 m below the sediment surface and this horizon is distributed evenly throughout the lower 20 km of the River. Inventories indicate that ~40 kg of TCDD are contained in this lower reach and Bopp et al. (1991) suggests that only 4–8 kg have been released to Newark Bay. Thus the high deposition rates allowed the Passaic to retain over 80% of the dioxins released into the river despite the fact that the release of dioxins occurred a mere 3 km from the mouth. Nevertheless a harbor-wide budget suggests the major contributor of 2,4,7,8 TCDD to the Harbor may be the remobilization of the Passaic River sediments (Powers et al., 2006) and thus this is a serious environmental issue and motivated this study of sediment transport processes in this system.

This study focuses on the exchange of water and sediments between the Passaic River and Newark Bay. In particular the study quantifies the role that tidal forcing, river flow and estuarine circulation have on sediment transport processes. The main results of this paper describe the relationship of the salt field to river discharge and channel morphology and to characterize and quantify sediment transport mechanisms. Results place these recent hydrographic and suspended sediment measurements in context with the historically high depositional rates in the Passaic. Measurements include a six-month record of moored ADCP and CT measurements along the estuarine reach of the Passaic and a series of along channel CTD surveys. The CTD data was used to characterize the salt intrusion length which was related to river discharge ($Q$) and channel morphology. The moored data was used to characterize and quantify sediment transport mechanisms by calibration of ADCP backscatter data against TSS samples. Results found that the salt intrusion length in the Passaic was largely consistent with the Hansen and Rattray scaling with river discharge, i.e., salt intrusion $Q^{-1/3}$. This result, however, is somewhat surprising because salt flux is dominated by tidal pumping, particularly for moderate to high river discharge. On the other hand the salt front position during moderate to high river flows also appears to be topographically controlled suggestive of a strong morphological feedback in this highly depositional channel. For discharge over twice the annual mean the salt front is advected out of

the river during the ebb tide. This morphological feedback is apparent in the historical bathymetric data showing that the region of high deposition has gradually moved seaward and now is located in the most seaward reaches of the river.

Sediment transport processes in the river were characterized by decomposing along channel sediment fluxes into a mean advective flux (river discharge), tidal pumping and shear mode (estuarine circulation). During low to moderate discharge net sediment transport is up river with both tidal pumping and estuarine circulation sediment transport processes directed upstream and the mean advective flux down stream. In contrast, during high river discharge the sign of the tidal pumping term reverses and net sediment transport is down stream. Results also emphasize that sediment transport processes are overwhelmingly dominated by high discharge events and our estimate of the net sediment flux at the mooring site is approximately equal to the estimates of the sediment loadings to the river. These results imply that the river is rapidly approaching a geomorphological balance and that the effectiveness of the river to trap sediment is rapidly diminishing as the salt intrusion length and overall vertical stratification diminishes with the infilling.

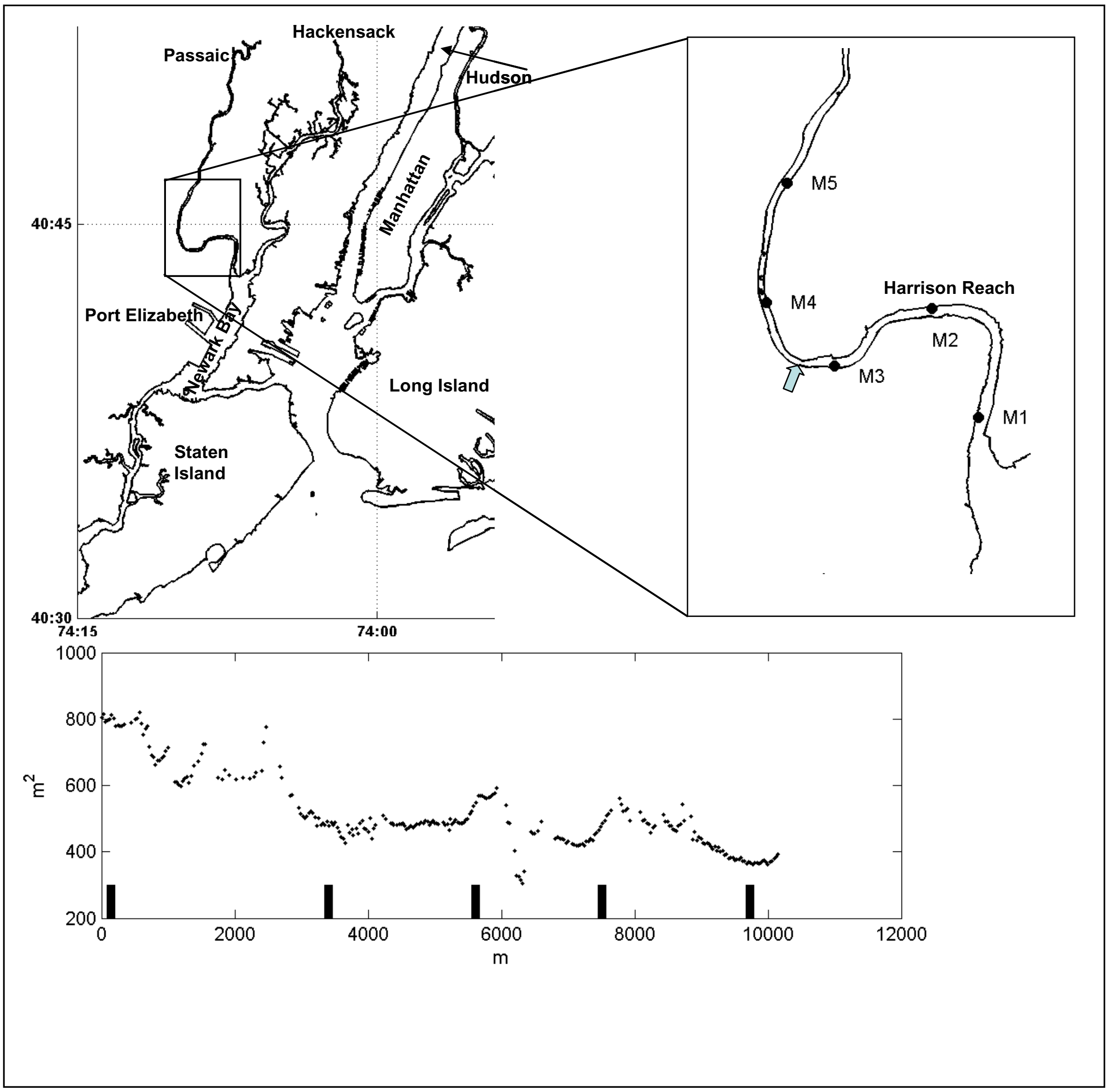


Figure 1. Upper panels show study site and mooring locations. Lower panel shows river cross-sectional area and locations of moorings.

Finally, estuarine stratification has been shown to be controlled by the horizontal Richardson number $Ri_x = \frac{N_x^2 H^2}{C_D U_T^2}$, where $N_x = \frac{g}{\rho}\frac{\partial\rho}{\partial x}$ is the along channel baroclinic forcing, $H$ is channel depth, $U_T$ is the tidal current velocity and $C_D$ a coefficient of quadratic friction. Monismith suggested a threshold of $Ri_x \sim 0.5$ above which stratification increases rapidly. In the case of the Passaic as the channel depth decreases tidal current velocities increase approximately with 1/H and thus there is a powerful tendency for $Ri_x$ to scale with $H^4$. While this will be buffered by an inverse response of $N_x$ this indicates that $Ri_x$ in the Passaic must have dropped considerably over the past 60 years and with it vertical stratification and its ability to trap sediment.

## References

Bopp, R.F., Gross, M.L., Tong, H., Simpson, H.J., Monson, S.J., Deck, B.L., Moser, F.C. (1991), A major incident of dioxin contamination: sediments of New Jersey estuaries, *Environmental Science and Technology*, 25, 951–956.

Hansen, D.V., Rattray, M. (1966), New dimensions in estuary classification, *Limnology and Oceanography*, 11, 319–326.

Huntley, S.L., Wenning, R.J., Su, S.H., Bonnevie, N.L., Paustenbach, D.J. (1995), Geochronology and sedimentology of the lower Passaic River, New Jersey, *Estuaries*,18(2), 351–361.

Monismith, S.G., Kimmerer, W., Burau, J.R., Stacey, M.T. (2002), Structure and flow-induced variability of the subtidal salinity field in northern San Francisco Bay, *Journal of Physical Oceanography*, 32, 3019–3032.

Powers, C.W., Munoz, G.R., Panero, R.A. (2006), *Pollution prevention and management strategies for dioxins in the New York/New Jersey Harbor*, edited by N.Y.A.O. Science, New York. pp259.

# The effect of deepening the Ems estuary on tidal dynamics and residual circulation patterns

ALEX S. CHERNETSKY[1], HENK M. SCHUTTELAARS[1], STEFAN A. TALKE[2]

1. Delft Institute of Applied Mathematics, Delft University of Technology, Mekelweg 4, 2624 CD Delft, Netherlands
   email: a.chernetsky@tudelft.nl, h.m.schuttelaars@tudelf.nl

2. Department of Civil and Environmental Engineering, University of Washington, P.O. Box 352700, Seattle WA 98195-2700, USA
   email: stalke@u.washington.edu

*Keywords: tidal dynamics, residual circulation, gravitational circulation; Ems estuary*

## ABSTRACT

The Ems estuary has changed over the past decades both from anthropogenic and natural influences. These changes of the estuary altered the flow patterns of water, the tidal characteristics and the patterns of sediment deposition. Many numerical models have been applied to the Ems estuary to estimate tidal range, sediment transport, mixing, etc. Reasonable results are found but the basic physical mechanisms resulting in these changes cannot be explained using this type of models. To fill this gap, an analytical model of the Ems estuary is developed and analyzed.

### Introduction

Over the past 20 years, successive deepening of the Ems estuary from 4–5 m to 7.3 m in the brackish water zone has significantly altered the tidal dynamics. Between 1980 (Figure 1a) and 2005 (Figure 1b), the tidal range has increased by 1.5 in the upstream reaches. Moreover, the propagating tidal wave shows more asymmetric shape in 2005 compared to the 1980 case. Furthermore, the surface sediment concentration has locally increased from 400 mg $l^{-1}$ to as much as 4–5 g $l^{-1}$. The position of the turbidity zone has shifted upstream as far as the tidal weir.

To investigate the observed changes, an analytical 2DV model approach is employed. Two distinctive bathymetries are considered which represent the 1980 and 2005 situation, respectively. Model results are calibrated to water level and velocity data for both the 1980 and 2005 case. Changes in the residual and $M_4$ flow and sensitivity of the model to different parameterization are investigated.

### Model description and method

The geometry of the estuary under consideration (see Figure 2) is funnel-shaped. The width of the estuary is prescribed as $B(x) = B_0\, e^{-x/L_b}$, with $L_b$ the so-called exponential convergence length and $x$ the location in the

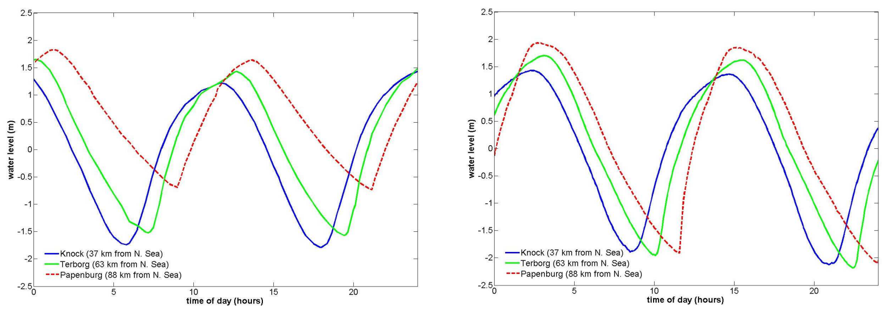


(a) Tidal curve in 1980 (b) Tidal curve in 2005

Figure 1. Tidal gauges at three locations along the Ems estuary.

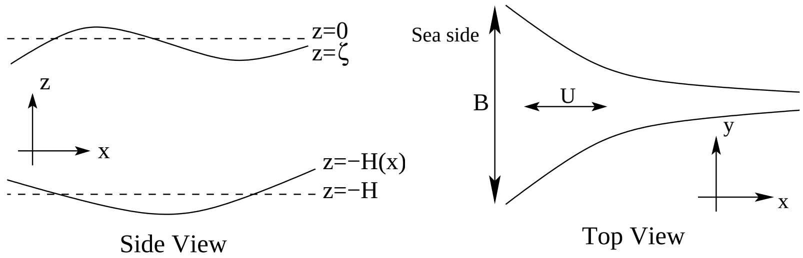


Figure 2. Geometry of the estuary.

estuary. The width of the estuary is considered to be larger than the water depth but much smaller than the typical horizontal length scale of the channel. The estuary is constrained by a weir. The undisturbed water depth H can be either a constant or a function of $x$.

The water motion of the estuary is described by the 2DV width-averaged shallow water equations.

$$\frac{\partial}{\partial x}u + \frac{\partial}{\partial z}w - \frac{u}{L_b} = 0 \tag{1}$$

$$u_t + uu_x + wu_z + g\zeta_x + \frac{g}{\rho_*}\int_z^{\zeta} \rho_x\, dz - (A_v u_z)_z = 0 \tag{2}$$

Here $x$ and $z$ are along-channel and vertical coordinates, $u$ and $w$ denote the width-averaged along-channel and vertical velocity components, $t$ time, $A_v$ a constant vertical eddy viscosity, and $g$ the gravitational acceleration.

At the seaward side, the system is forced by a prescribed tidal elevation $\zeta = A\cos\sigma t$ with $A$ the amplitude of tidal elevation and $\zeta$ the frequency of the main tidal constituent. At the riverine side the cross-sectionally integrated velocity equals the river discharge $Q$. Hence at $x = x_{\text{discharge}}$ the cross-sectionally averaged time-independent contribution is equal to $Q/HB$ and the time-dependent cross-sectionally averaged horizontal velocity is zero.

At the surface $z = \zeta$ we assume that the water motion is stress free and satisfies the kinematic boundary condition:

$$\begin{aligned} u_z &= 0, \\ w &= \frac{\partial \zeta}{\partial t} + u\frac{\partial \zeta}{\partial x}. \end{aligned} \tag{3}$$

At the bottom $z = -H + h$, a so-called partial slip condition is used for the tangential velocity component. Furthermore, we require the bottom to be impermeable. Those conditions read

$$\begin{aligned} A_v u_z &= \frac{\tau_b}{\rho}, \\ w &= -u\frac{\partial H}{\partial x}. \end{aligned} \tag{4}$$

Generally the bottom stress $\tau_b$ is proportional to the friction velocity squared. By linearizing the quadratic friction law, $\tau_b$ can be related to the velocity at the bed and reads $\tau_b = \rho r u$. Thence, the partial slip condition can be rewritten as $A_v u_z = ru$ (see Schramkowski, 2002). Here the parameter $r$ is the so-called stress parameter. By varying it from $r = 0$ to $r \to \infty$, the boundary condition is varied between a stress-free and no-slip bottom condition. First, to obtain a solution, the water motion Equations (1), (2) and the appropriate boundary conditions are made dimensionless. After scaling, the ratio of the tidal amplitude over the water depth appears as a dimensionless parameter in the shallow water equation and the boundary conditions. Usually this parameter is much smaller than 1. Hence one can approximate the solution of the shallow water equations and the boundary conditions by expanding the physical variables in power series of this small parameter. After collecting terms of equal powers of the small parameter the equations and the boundary conditions are solved analytically.

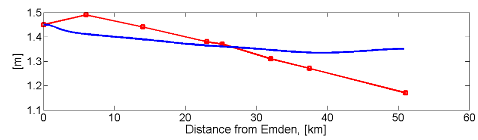


(a) Tidal amplitude in 1980

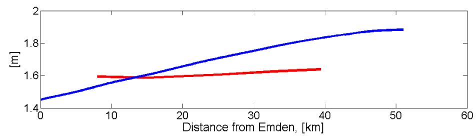


(b) Tidal amplitude in 2005

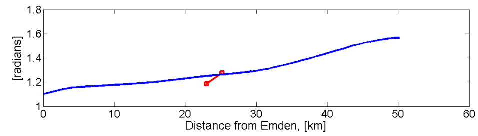


(c) Relative phase shift in 1980

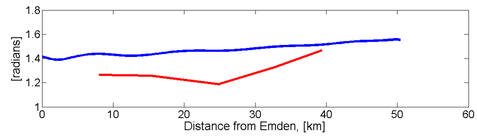


(d) Relative phase shift in 2005

Figure 3. Calibration of the model. The red curve represents the data measured in 1980 and 2005 respectively, the blue curve is the model result.

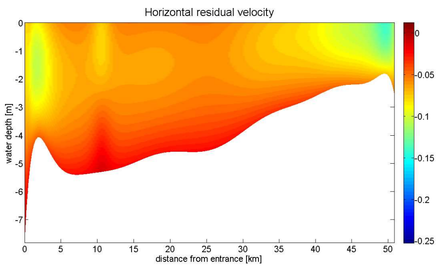


(a) 1980 case

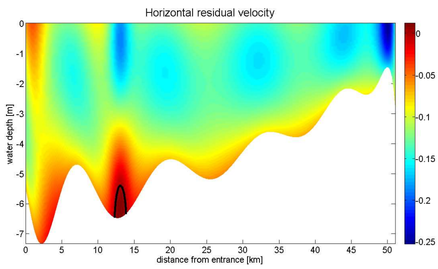


(b) 2005 case

Figure 4. Residual flow case representative for 1980 and 2005 year cases.

Table 1: Parameters used in the model for 1980 and 2005 cases.

| | 1980 | 2005 |
|---|---|---|
| Mixing | 0.0127 $m^2\ s^{-1}$ | 0.0043 $m\ s^{-1}$ |
| Friction | 0.0128 $m^2\ s^{-1}$ | 0.0033 $m\ s^{-1}$ |

## Results and discussion

Most model parameters can be directly obtained from observations. However, the vertical mixing coefficient $A_v$ and bed friction parameter $r$ have to be obtained by calibrating the model to the data. This is done using the least squares method. Data for the$M_2$ relative tidal phase and amplitude is used to fit the model. The mixing and friction parameters that minimize the sum of the squared residuals are used as optimal parameters. Here, a residual is the difference between an observed value and the value given by the model. Two sets of parameters are determined, one using data obtained in 1980 and one for 2005. In Figure 3 the results of the calibration process are shown.

The resulting set of parameters is presented in Table 1. As one can see there is a factor of three difference in magnitude between the corresponding parameters. This large difference can be explained by the observation that in 1980 the bottom was much more sandy than in 2005.

Using these parameters, the residual and $M_4$ water motion is calculated. Figure 4 shows the horizontal residual velocity distribution. The increased depth and the decrease of the friction and mixing have changed the general pattern of residual currents: there is an increase in the velocity magnitude by a factor of two.
Since an analytical model is used, it is possible to separately calculate the various components of the residual velocity, such as gravitational circulation, river inflow, etc. In this way, it can be seen that the residual current patterns have mainly changed due to changes in gravitational circulation and tidal return flow from 1980 to 2005. Those components are presented on Figure 5.

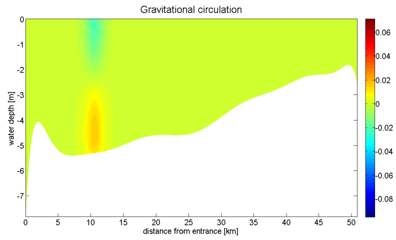


(a) Gravitational circulation 1980

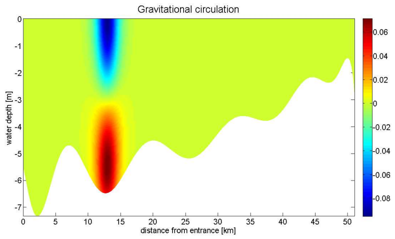


(b) Gravitational circulation 2005

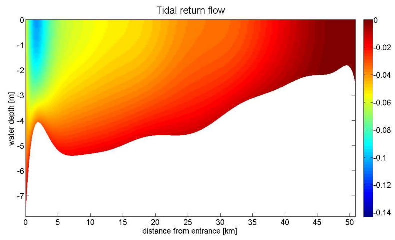


(c) Tidal return flow 1980

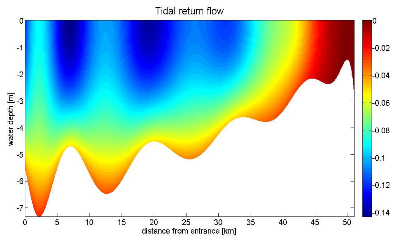


(d) Tidal return flow 2005

Figure 5. Residual flow components: gravitational circulation and tidal return flow.

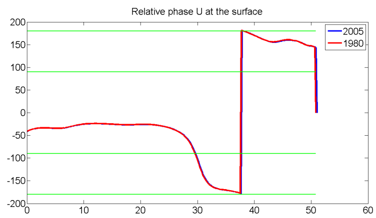


(a) $M_4$ relative phase of along-channel velocity at the surface representative of 1980 and 2005 cases

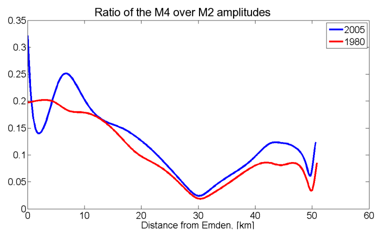


(b) Ratio of the $M_4$ over $M_2$ amplitudes representative of 1980 and 2005 cases

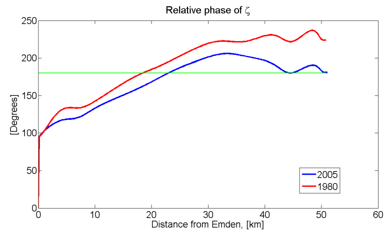


(c) $M_4$ relative phase of sea surface elevation representative of 1980 and 2005 cases

Figure 6. Relative phases and amplitudes for the $M_4$ flow.

In Figure 6a, one can see that despite the changes in the residual flow in the estuary there has not been a change in ebb or flood dominance. However, the ratio of the $M_4$ and $M_2$ amplitudes increased, see Figure 6b. On the other hand, the durations of the rise and fall have changed (see Figure 6c).

## Conclusions

Model results suggest that changes to tidal magnitude and asymmetry between 1980 and 2005 are mainly caused by a factor 3× decrease in hydraulic roughness. From the $M_2$ calibration, friction and mixing parameters are found to show a decrease by a factor of 3 between the two years. Residual flow has increased by a factor of 2 mainly due to changes in gravitational circulation and tidal return flow. Ebb and flood dominance has not changed, only the ratio of the $M_2$ and $M_4$ amplitudes has increased. No correspondence between changes in durations of rise and fall of sea surface elevation and changes in ebb and flood dominance are observed.

## References


Schramkowski, G., Schuttelaars, H., de Swart, H. (2002), The effect of geometry and bottom friction on local bed forms in a tidal embayment, *Continental Shelf Research*, 22, 1821–1833.

# Modeling estuarine and coastal small scale processes in the Northern Adriatic Sea

DEBORAH BELLAFIORE[1, 2], GEORG UMGIESSER[1]

1. Institute of Marine Science, ISMAR-CNR, 1364/a Castello, Venice, Italy
   email: deborah.bellafiore@ismar.cnr.it, georg.umgiesser@ismar.cnr.it

2. Consorzio Venezia Ricerche – Centro Euromediterraneo per i Cambiamenti Climatici, CVR-CMCC, 5/12 Via Della Libertà, Marghera, Venice, Italy

*Keywords: hydrodynamic modeling, finite elements, baroclinic forcing, turbulence, vorticity, coastal currents*

## ABSTRACT

A 3D shallow water hydrodynamic finite element model has been developed to investigate the small scale processes around the inlets that connect the Venice lagoon with the Northern Adriatic Sea. The coastal and the interaction processes between the main basin and one of the biggest lagoons in Europe raises great interest because of the different forcings acting such as wind, tides, river outflow, turbulence produced in the inlet dynamics, and the varying scales to describe its interaction phenomena. To apply a model able to describe all these processes is a challenge in coupled basins and in the coastal areas.

The model has been run for the test year 2004 and the impact of each forcing has been studied. The attention is focused on the dynamics near the three inlets of the Venice Lagoon. Maps of vorticity have been produced, considering the influence of tidal flows and wind stress in the same area. Turbulence effects have also been analyzed.

Finally a comparison with real data measurements, surface velocity data from HF Radar near the Venice inlets, has been performed, which allows for a better understanding of the processes and their dynamics. The next step will be the operational application in the area to monitor changes and evolutions in the hydrodynamics due to anthropogenic and climatic variations in the morphology.

### Model and methods

A 3D finite element model, SHYFEM (Shallow water Hydrodynamic Finite Element Model), created at the Institute of Marine Science ISMAR-CNR in Venice has been applied to investigate the small scale coastal and interaction processes in the Northern Adriatic Sea.

The model is based on the primitive equations, in the shallow water formulation. The hydrostatic approximation is applied. The equations are solved integrating transports on each layer and computing the advection, the horizontal diffusion, the Coriolis term and, separately, the barotropic and baroclinic pressure gradient terms. Even if the computation of baroclinic terms can be considered secondary for the internal area of the Venice Lagoon (Umgiesser et al., 2004), their influence starts to become important in the reproduction of coastal patterns, because of the presence of several rivers in the Northern Adriatic coastline.

The SHYFEM model applies an Arakawa B type finite element grid for the horizontal discretization and *z*-layers vertically. The barotropic pressure gradient and Coriolis terms are semi-implicitly discretized, using the Crank-Nicholson scheme, while the baroclinic, the advective and the horizontal diffusion terms are explicitly discretized.

Vertically, vector and scalar variables are computed in the center of each layer while stresses are computed at the interfaces. For this reason, and in order to solve in a more stable way the bottom layer of each element, the stress terms (together with the bottom stress term) are treated implicitly. At the surface layer wind stresses are computed introducing a drag coefficient, while the bottom friction is discretized with a quadratic bottom drag in the Adriatic Sea and using the Chezy formula to compute the depth dependent friction coefficient inside the lagoon.

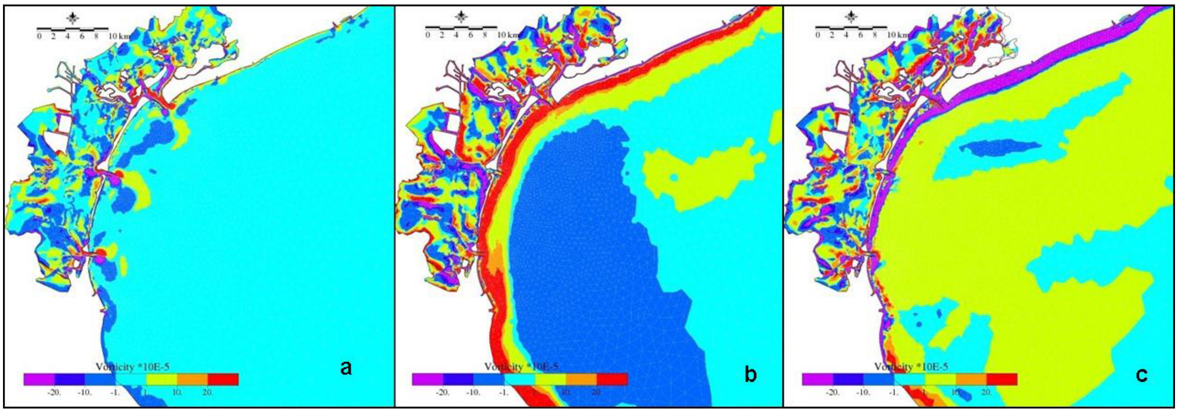


Figure 1. Surface layer averaged vorticity maps for three idealized simulations for the Northern Adriatic Sea. Tidal forcing is considered in the first one (a), two different wind fields, Scirocco (b) and Bora (c), are imposed in the others. All of them included river runoff forcing.

The model contains a *k-ε* turbulence closure scheme which is taken from the General Ocean Turbulence Model, GOTM (Burchard, 2002). This allows for the evaluation of the importance of vertical turbulence on the inlet dynamics.

## Ideal simulations and impact of forcing

The main forcings acting in the North Adriatic coastal areas are tides, wind and freshwater coming from rivers. To investigate the impact of tides and winds, three simulations have been performed applying the model to the Adriatic Sea. The first one imposes (a) an ideal sinusoidal semi-diurnal water levels signal at the open boundary at the Otranto Strait without wind. The other two simulations do not consider tidal forcing but introduce (b) an idealized Scirocco wind field, wind from SE, and (c) an idealized Bora wind field, wind coming from NE. In each run river runoff forcing has been kept constant.

The three simulations run for 16 days in order to eliminate transient effects and to reach a steady state. The last day is used for the analysis. The results from the first simulation have been averaged over 12 hours. This choice is driven by the intent to filter the tides, being able to analyze only the tidal induced patterns, not the direct ones. The other two simulations have been daily averaged. In Figure 1 the corresponding surface layer vorticity maps are shown.

A fourth run, using realistic forcings for the year 2004, has been carried out. To produce maps filtered from the tidal signal, a monthly average has been applied. This allows elimination of the main tides, which are diurnal and semi-diurnal. Comparing results of the realistic and the idealized runs some hydrodynamical patterns can be ascribed to the impact of each forcing. The two spots of inverse vorticity, which are present near each inlet, are due to the advection of the residual tidal signals (Figures 1 and 2). The wind from NE enhances negative vorticity along the coast, which means that Bora wind creates higher currents close to the coast. On the other side the wind from SE increases the positive vorticity (circles in Figure 2).

An interesting pattern can be seen south of the Chioggia Inlet (square and zoom in Figure 2). In the average surface vorticity map that area is characterized by an alternation of littoral positive and negative vorticity spots. It is not yet clear if these vorticity spots are caused by a node to node numerical oscillation, maybe enhanced by bathymetry, or if there is a physical explanation. Perhaps this phenomenon can be connected with the interaction between the tidal currents, typical of the area in proximity of inlets, and the river freshwater runoff coming from the two southernmost rivers, Brenta and Adige. The thermohaline currents, the tidal secondary effects and boundary effects could participate in producing these patterns. In the next future, the connections with sediment transport in the same area will be studied.

Two more simulations have been run to obtain information on the turbulence impact near the Venetian Inlets, switching the turbulence closure module on and off. As seen in Figure 3 the main effect can be seen in the coastal area: the computation of turbulence effects seems to influence the general circulation pattern and near the inlets the changes can be noted in the spreading of plume and in enhancing the southern recirculation cell.

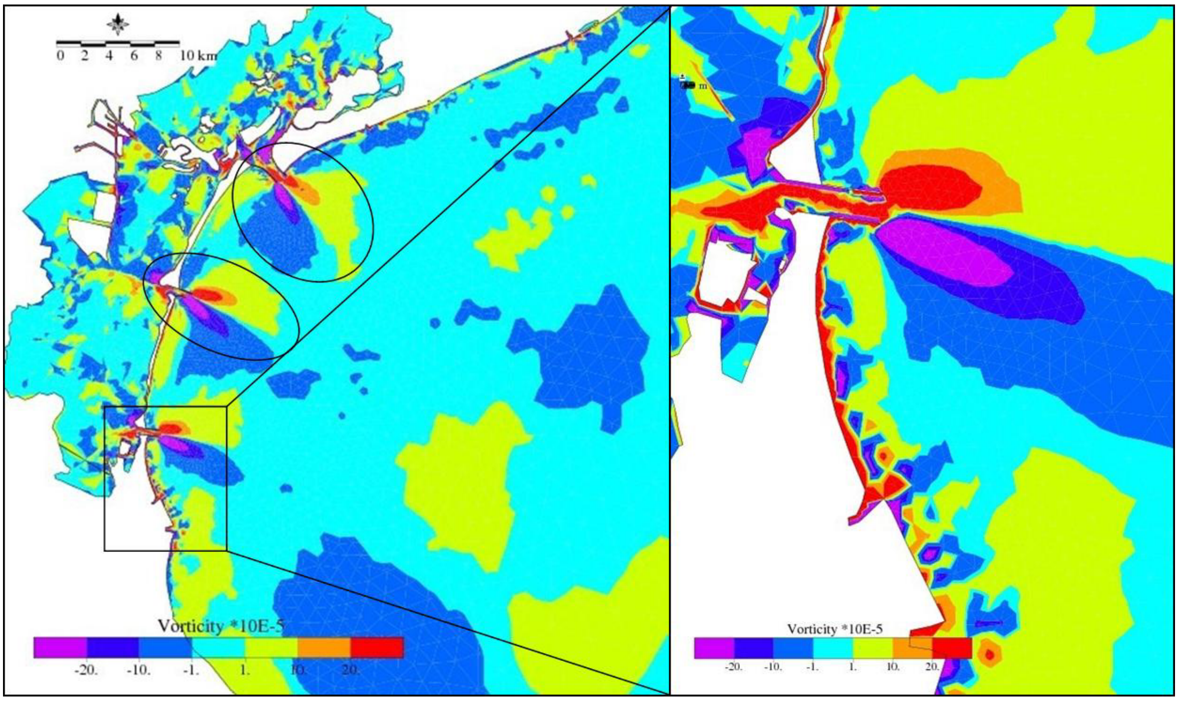


Figure 2. Surface layer averaged vorticity map for a realistic run for the Northern Adriatic Sea, May 2004, and zoom on the Chioggia Inlet.

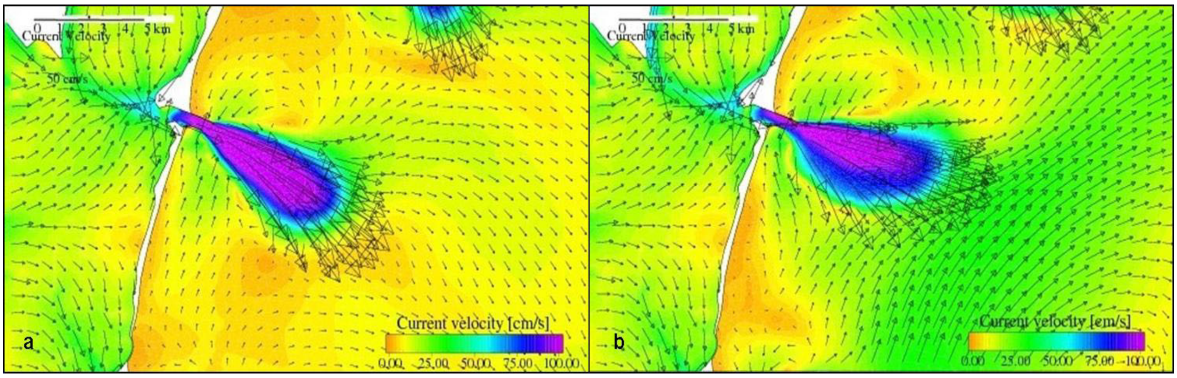


Figure 3. Snapshot of surface currents maps of two twin simulations without (a) and with (b) the *k-ε* turbulence closure scheme. Turbulence produces a higher horizontal spreading of the plume.

## Comparison with measurements

Finally, model results from the realistic simulation of year 2004 have been compared with measurements from three HF Radars that covers the study area. A harmonic analysis has been done and the de-tided signals have been compared. As an example in Figure 4 an average of all surface currents in condition of calm wind is shown. Both measured and modeled data register a vortical persistent structure between Malamocco and Chioggia Inlets (the central and southern inlets of the Venice Lagoon). The model is able to reproduce structures already seen in the measurements, as explained in Mancero Mosquera et al. (2007) even if it seems that the model reproduces an outflowing plume from the three inlets that is too strong. A first explanation could be that the preliminary comparison has been done with a simulation that does not take into account the turbulence closure module.

## Conclusions

The SHYFEM model has been applied to study the dynamics in the coastal zone and interaction areas between the Venice Lagoon and the Northern Adriatic Sea. The modeling tool permitted to discriminate the action of each of the main forcings in this area, e.g., tides and wind. Moreover, turbulence has been identified

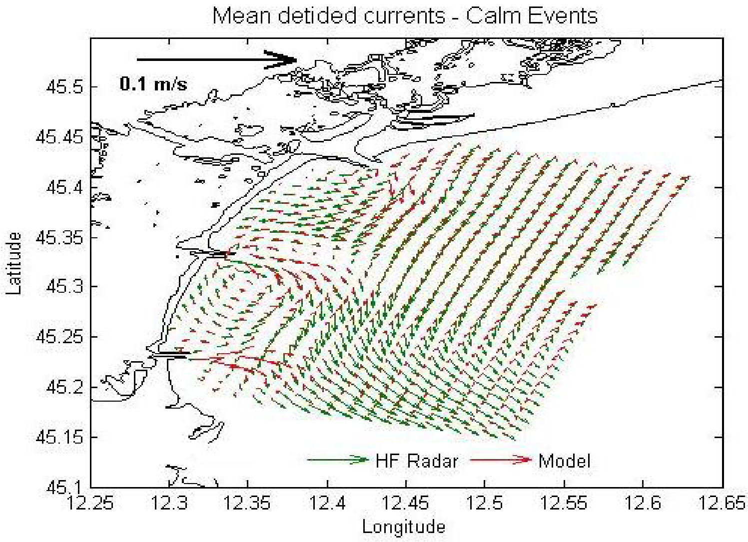


Figure 4. Map of averaged values of non tidal currents in calm wind events. Comparison between values from HF Radar (green) and model (red).

as an impacting factor in the coastal zone and particularly near the inlets. The model is reproducing correctly the dynamics of the area and the comparison with measurements from HF Radar is successful. The aim has been to reproduce some coastal patterns as the sub-mesoscale vortices which can be noted in the southern part of each inlet. The process study, from the evidence of model results, leads to a hypothetical influence of advection terms and border effects to explain this persistence. In the next future the hydrodynamic patterns identified in the study area will be connected to changes in the morphology along the littoral, in order to identify connections, causes and consequences.

## References

Burchard, H. (2002), *Applied turbulence modeling in marine waters*, Lecture Notes in Earth Science, Springer.

Mancero Mosquera, Gačić, M., Kovačević, V., Mazzoldi, A., Cosoli, S., Paduan, J.D., Sadegh, Y. (2007), *Surface current pattern in front of the Venetian Lagoon and their variability at different wind regimes*, Scientific Research and Safeguarding of Venice – Research Programme 2004–2006, Vol. 3. (Submitted.)

Umgiesser, G., Bergamasco, A. (1995), *Outline of a primitive equation finite element model*. In: Rapporto e Studi, Vol. 12, pp291–320. Venice, Italy: Istituto Veneto di Scienze, Lettere ed Arti.

Umgiesser, G., Melaku-Canu, D., Cucco, A., Solidoro, C. (2004), A finite element model for the Venice Lagoon. Development, set-up, calibration and validation. *Journal of Marine Systems*, 51, 123–145.

# Numerical simulations of overmixing in an idealized estuary

ROBERT D. HETLAND

Department of Oceanography, Texas A&M University,
College Station TX 77843-3146, USA
email: hetland@tamu.edu

*Keywords: salinity intrusion, hydraulic control, ROMS*

## ABSTRACT

Stommel and Farmer (1953) derived a theory for the maximal exchange between an estuary and the ocean based on a combination of mass and salt conservation (i.e., Knudsen's relation) and hydraulic control theory at the estuary mouth. This upper limit on estuarine exchange is termed 'overmixing', as there is more than enough mixing in the estuary to maintain the density difference at the mouth. This seminal work inspired a number of papers on hydraulic control of baroclinic flow through constrictions (e.g., Armi and Farmer, 1986). However, none of these papers returned to the idea that the limitations on the exchange imposed by hydraulic control could in turn modify the water properties at the mouth; that is, that the mass and salt flux at the mouth must obey Knudsen's relation. Numerical simulations of an idealized estuary with artificially enhanced mixing show that the estuary never quite reaches the theoretical overmixing limit, although many of the qualitative features of the overmixing solution are reproduced. In particular, it is possible to locate the point in parameter space where the advective terms begin to limit the exchange flow at the constriction in a way that is similar to overmixing.

## Introduction

Overmixing theory results from combining the salt balance constraints of Knudsen's relation with the limits of hydraulic control at a constricted estuary mouth. In the limit of no mixing, the solution is simply that fresh water leaves the estuary. As mixing is increased, the exchange at the mouth becomes greater. Salt balance places no bound on the exchange, so as the mixing within the estuary increases, the salinity of the upper layer outflow asymptotically approaches the oceanic inflow salinity. Hydraulic control places an upper bound on this exchange.

Hetland and Geyer (2004) showed that both steady, partially-mixed estuaries [such as described by Hansen and Rattray (1965) and Chatwin (1976)] and the overmixed estuary solution predict the same estuarine salt flux. That is, in both cases salt flux is a function of river discharge alone, and independent of the strength of vertical mixing, a proxy for tidal stirring. Thus, even in very idealized estuaries, it is difficult to determine what controls the salt flux in an estuary: vertical mixing or hydraulic control?

Overmixing theory is based on steady, inviscid, two-layer dynamics whereas in real estuaries the salinity and velocity have three-dimensional structure, interior mixing is necessary to export salt from the estuary, and bottom drag can influence the point of hydraulic control (e.g., Nielsen et al., 2004). Thus, a technical problem in examining overmixing is that properties derived for two layer models, like the internal Froude number, are difficult to estimate in a three-dimensional flow. It is not obvious what definition to use for the internal interface, and there are at least two possible methods that could be used for averaging the layer quantities.

Another, more general problem is how can you tell if a real estuary is overmixed? One functional definition is that when the constriction that defines the point of hydraulic control narrows, the salt content of the estuary upstream is reduced. It is straightforward to perform such an experiment numerically, but, it is not easy to perform such an experiment in nature.

It is also possible to examine the importance of the advection terms in a numerical model. Hydraulic control requires the lateral advective term balances the pressure gradient term in the along-channel momentum balance. For partially-mixed estuaries (e.g., Hansen and Rattray, 1965), the pressure gradient term is balanced by vertical mixing of momentum.

The balance between mixing and advection within a constriction was examined by Hogg et al. (2001). They noted that the flow through a constriction varied from the viscous-advective-diffusive limit to the hydraulic control limit based on a non-dimensional number $Gr\,\alpha^2$, where $Gr = g'H^3/K_v^2$ is the Grasshof number and $\alpha = H/L$ is the aspect ratio of the water depth, $H$ to the along-channel length scale of the constriction, $L$. This non-dimensional number may be written in terms of two timescales

$$Gr\,\alpha^2 = \frac{g'\,H^3}{K_v^2}\,\frac{H}{L} = \frac{H^4}{K_v^2} \Big/ \frac{L^2}{g'\,H} = \frac{\text{Mixing timescale}^2}{\text{Advective timescale}^2} \tag{1}$$

The basis for overmixing theory is that the mixing is spatially separated from the otherwise inviscid flow at the constriction – the mixing occurs only within the estuary. In real estuaries it is not necessarily clear how this could occur.

The importance of the advective timescale, $L(g'\,H)^{-1/2}$, was also noted by Helfrich (1995) with his parameter

$$\gamma = \frac{(g'H)^{1/2}}{L}\,T = \frac{\text{Forcing timescale}}{\text{Advective timescale}} \tag{2}$$

a measure of the dynamic length of the constriction. It should be noted that, in the hydraulic control limit, the Froude number is near one, so $(g'\,H)^{-1/2}$ is also related to the magnitude of the exchange flow.

For a steady flow, a decrease in salt flux must also be associated with a decrease in the mean salinity by the global salt balance $u'\,s' = u_R\,\overline{s}$. Thus, it is possible to investigate overmixing using the depth averaged salinity structure along the length of the estuary. This method is examined further below.

## Review of overmixing theory

Stommel and Farmer (1953) derived a criterion for control of salinity in an estuary by a constriction. They named this 'overmixing,' as the net mixing on the upstream side of the constriction was more than enough to have the integrated vertical salt flux in the bay balance the lateral salt flux at the constriction. The primary assumption is that the flow at the constriction is critical

$$\frac{u_{out}^2}{g'h} + \frac{u_{in}^2}{g'(H-h)} = 1 \tag{3}$$

where $g' = g\,\Delta\rho/\rho_0$, $u_{\text{out}}$ and $u_{\text{in}}$ are the outflowing (seaward, or downstream) and inflowing (upstream) velocities of the upper and lower layer respectively, $h$ is the thickness of the upper layer, and $H$ is the thickness of the entire water column. The reference density, $\rho_0$, is defined here as the density of the lower layer water.

The net volume of water is conserved within the estuary, so that the volume fluxes in and out of the estuary must balance as

$$u_{out}\,h - u_{in}\,(H-h) = u_f\,H \tag{4}$$

where $u_{\text{f}}$ is the average flow rate fresh water from the upstream river would have at the constriction. Thus, $u_f = Q_f/H\,W$, where $Q_f$ is the volume transport of the river, and $W$ is the width at the constriction. Mass is also conserved within the estuary

$$\Delta\rho_f\,u_f\,H = \Delta\rho u_{out}\,h \tag{5}$$

where $\Delta\rho = \rho_{\text{in}} - \rho_{\text{out}}$, $\Delta\rho_f = \rho_{\text{in}} - \rho_{\text{river}}$ is the density of the upper layer. The densities $\rho_{\text{in}}$, $\rho_{\text{out}}$, $\rho_{\text{river}}$ are the densities of the inflow, outflow, and river respectively. Note, the mass balance is equivalent to a salt balance if a linearized equation of state, $\rho = \rho_0 + \beta\,s$, is used.

Using Equations (3–5), Stommel and Farmer obtain

$$\phi(\eta,\nu;Fr_f) \equiv -Fr^{-2}\eta^3(1-\eta)^3\nu(1-\eta)^3 + \eta^3(1-\nu)^2 = 0 \tag{6}$$

where $\eta = h/H$, $\nu = (1 - \Delta\rho/\Delta\rho_f)$, $Fr_{\text{f}} = u_f/\sqrt{(g'_f H)}$, and $g'_f = g\,\Delta\rho_f/\rho_0$. The freshwater Froude number, $Fr_f$, may be thought of as the lower limit of Froude numbers the system can support. Equation (6) describes a suite of possible solutions for exchange flow, not necessarily maximal exchange. To find the point of maximal exchange, an $\eta$-derivative of Equation (6) is used to find the point where the outflow is thickest

$$Fr_f^{-1}(1-\nu)^3\eta^4 = 1. \tag{7}$$

Assuming that $Fr_f << 1$, Stommel and Farmer simplify this equation as

$$\varepsilon = \eta - 1/2 = (32\, Fr_f^{-1})^{-1/3}\,. \tag{8}$$

Where Equation (7) needs to be solved numerically, Equation (8) may be solved analytically. The two solutions are very similar for $\nu > 0.5$, but diverge as $\nu \to 0$. In both cases, the structure of the flow at the constriction, specified by $\eta$ and $\nu$, is defined by the river discharge, the geometry of the constriction, and a reference salinity (typically the oceanic salinity).

Equation (7) may also be solved in reverse – that is, given a value for $Fr_f$, the corresponding $\eta$ and $\nu$ for an overmixed solution may be found. From $\eta$ and $\nu$, the depth averaged salinity may be found

$$\bar{s}_{\mathrm{om}} = s_{\mathrm{ref}}\,(1 - \eta + \eta\nu) \tag{9}$$

where $s_{\mathrm{ref}}$ is a reference salinity. In the overmixing solution, this would be the salinity of the lower layer. However, it is also possible to simply take the bottom salinity as an approximation with very similar results. Of course, this equation is only valid at the point of hydraulic control, the point where the exchange is limited at the constriction. The overmixing limit for the vertical mean salinity is everywhere greater than the actual mean salinity, $\bar{s}$. However, near the constriction, $\bar{s}_{\mathrm{om}}$ has a local minimum and $\bar{s}$ has a local maximum; in the overmixing limit, the ratio $\bar{s}/\bar{s}_{\mathrm{om}}$ will approach a local maximum of one. The largest value of $\bar{s}/\bar{s}_{\mathrm{om}}$ will determine the extent to which hydraulic control affects the estuarine salt flux at the constriction.

## Numerical results

The Regional Ocean Modeling System was configured for a long, flat-bottomed estuary with a constriction. Within the estuary, the depth is 10 m and the channel width away from the constriction is 500 m. The bathymetry is deeper toward the oceanic end. In order to promote overmixing, vertical mixing is artificially enhanced beginning 50 km upstream of the constriction. The primary parameters in the simulation are the river discharge and the width of the constriction.

There are some fundamental differences in the numerical simulations as compared to theoretical solutions of hydraulic exchange flow through a constriction. Notably, inviscid, two-layer theory predicts that the combined internal Froude number is at a minimum value (and critical) at the constriction point, and supercritical on either side; numerical simulations show a maximum in the combined Froude number slightly seaward of the constriction.

As the width of the constriction decreases, the salt content of the estuary upstream of the constriction also decreases. Figure 1 shows that the salt content of the estuary upstream of the constriction as a function of constriction width. The salt content decreases by about 15% when the constriction is half of the channel width. Note that the response would be stronger if the estuarine length scale was not determined by the location of the elevated mixing. In the present simulation, the salinity never penetrates much into this high-mixing region, so the change in integrated salinity is primarily a function of the mean salinity upstream of the constriction, and is not a change in salt wedge penetration.

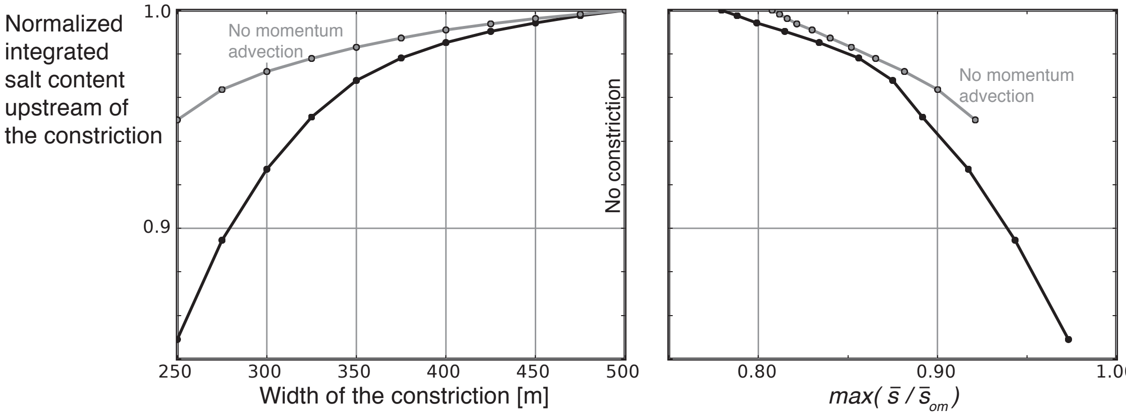


Figure 1. The integrated salt content upstream of the constriction, normalized to the case with no constriction, is shown as a function of width of the constriction (left), and overmixed to simulated $\bar{s}$.

In order for hydraulic control to influence the upstream lateral salt flux, the advective terms in the momentum balance must be the principal term balancing the pressure gradient. However, Hansen and Rattray style estuaries with no horizontal advection of momentum will also show a reduction in integrated salinity with decreasing constriction width. This is because the length scale of the estuary decreases within the constriction, or in other words, longitudinal depth-averaged salinity gradients are increased. So, given the same mean salinity downstream of the constriction, the upstream mean salinity will be lower for a tighter constriction.

To test the importance of the advective terms in reducing the lateral salt flux through the constriction, the advective terms in the momentum equation were turned off in the model. The results are shown by the gray lines in Figure 1. For the no-advection cases, there is a decrease in upstream integrated salt, however, the decrease is much less marked, only 5% compared to 15%, in the cases with the complete momentum equation.

The right panel of Figure 1 shows the integrated salt seaward of the constriction as a function of the maximum value of $\overline{s}/\overline{s}_{\mathrm{om}}$. This ratio shows how close the estuary is to overmixed at a given cross-section (given the bottom salinity and the river flow), and is maximum at the point where advection limits the lateral salt flux. There is a break in the slope near $\max(\overline{s}/\overline{s}_{\mathrm{om}}) = 0.85$ that marks the transition between a linear (Hansen and Rattray style) reduction in integrated salt upstream of the constriction and a non-linear reduction similar to hydraulic control.

## Conclusions

Within the numerical solutions, the estuary is never actually overmixed in that it matches the Stommel and Farmer (1953) solution. However, the solution demonstrates that a constriction may cause the lateral salt flux to be limited by hydraulic control, in that the advective terms are responsible for reducing the salt flux. Given that these numerical solutions were explicitly designed to create a scenario favorable to overmixing, it seems unlikely that any real estuary is overmixed in the strict sense. However, it is possible in the more general sense that estuarine salt flux may be limited by hydraulic processes, here defined as the relative importance of the lateral momentum advection terms compared to vertical mixing, both at and upstream of the constriction.

## References

Armi, L., Farmer, D.M. (1986), Maximal two-layer exchange through a contraction with barotropic net flow, *Journal of Fluid Mechanics*, 164, 27–51.

Chatwin, P.C. (1976), Some Remarks on the Maintenance of the Salinity Distribution in Estuaries, *Estuarine and Coastal Marine Science*, 4, 555–566.

Hansen, D.V., Rattray, M. (1965), Gravitational circulation in straits and estuaries, *Journal of Marine Research*, 23, 104–122.

Helfrich, K.R. (1995), Time-dependent two-layer hydraulic exchange flows, *Journal of Physical Oceanography*, 25, 359–373.

Hetland, R.D., Geyer, W.R. (2004), An idealized study of long, partially mixed estuaries, *Journal of Physical Oceanography*, 34(12), 2677–2691.

Hogg, A.M., Ivey, G.N., Winters, K.B. (2001), Hydraulics and mixing in controlled exchange flows, *Journal of Geophysical Research*, 106(C1), 959–972.

Nielsen, M.H., Pratt, L., Helfrich, K. (2004), Mixing and entrainment in hydraulically driven stratified sill flows, *Journal of Fluid Mechanics*, 515, 415–443.

Stommel, H., Farmer, H.G. (1953), Control of salinity in an estuary by a transition, *Journal of Marine Research*, 12(1), 12–20.

# Parameterization of sediment-induced buoyancy destruction and drag reduction in estuaries

JOHAN C. WINTERWERP[1, 2], MARIEKE LELY[1]

1. Environmental Fluid Mechanics Section,
Faculty of Civil Engineering and Geosciences, Delft University of Technology,
P.O. Box 5048, 2600 GA Delft, Netherlands
email: j.c.winterwerp@tudelft.nl

2. Deltares, Rotterdamseweg 185, P.O. Box 177, 2600 MH Delft, Netherlands

*Keywords: fine sediment, drag reduction, Monin-Obukhov length scale*

## ABSTRACT

Many observations have been reported in the literature on drag reduction by suspended fine sediments in rivers and estuaries. For instance, Dong et al. (1997) and Guan et al. (1998) reported decreases in bed friction by about 15% in the JiaoJiang estuary, China; Wang et al. (1998) found drag reductions of 15–30% in the Yellow River; Beardsley et al. (1995) found drag reductions in the Amazon mouth in the range of 25%, similar to values reported in the Yangtze River (PDC, 1996). Also in Europe, comparable reductions were found in the Ems estuary, Germany/The Netherlands (Weilbeer, 2005), in the Loire estuary, France (LeHir et al., 1994, 2002) and in the Severn estuary, UK (Odd and Cooper, 1988), to name a few.

From theoretical considerations, drag reduction by fine sediments can be explained by three different processes:

1. buoyancy destruction induced by vertical gradients in the concentration of fine suspended sediment,
2. reduction in bed forms; hence reduction in form drag,
3. thickening of the viscous sub-layer through viscous damping induced by mud flocs.

The latter was studied experimentally by Gust (1976) in a small flume with dilute clay suspensions (solids fractions < 1%). At hydraulically smooth conditions he observed drag reductions of about 40%, which he attributed to a thickening of the viscous sub-layer by a factor 2–5; he did not measure any changes in the velocity profile or turbulence characteristics further away from the wall. In fact, the logarithmic law appears still applicable, with the common values of the von Kármán constant (i.e., $\kappa = 0.4$). Gust hypothesized that this drag reduction is caused by the streamlining of deformable mud flocs, similar to drag reduction by polymers (Lumley, 1969).

The generation of bed forms is generally attributed to bed load transport; in fact all bed form models use bed load formulae to predict bed form dimensions (e.g., van Rijn, 1993). As bed load transport is not likely in fine sediment suspensions (apart form special features such as fluid mud, which are beyond the subject of the current paper), one would expect general absence of bed forms in flows laden with fine sediment. However, it is known that bed forms in muddy environments can develop, such as the ridges and runnels developing in streamwise direction in the Bay of Marenne (Dyer, 1997).

At present, it is not known whether all three mechanisms contribute to drag reduction in fine sediment laden flows, or whether under specific conditions one or the other is dominant. In the current paper, we analyze the contribution of sediment-induced buoyancy destruction on drag reduction. This analysis is carried out through sensitivity analyses with a numerical model, assessing hydraulic drag through simulations with and without suspended fine sediment. Currently, the effects of buoyancy destruction are well understood, and may be modeled properly in three-dimensional numerical models with a $k$-$\varepsilon$ turbulence closure scheme (e.g., Winterwerp, 2001). However, as such models still require considerable computational efforts, we first parameterize the effects of buoyancy destruction through a formal integration of Barenblatt's (1953) log-linear velocity profile. The two coefficients that emerge in this model are established with a 1DV POINT MODEL (1DV model, e.g., Winterwerp, 2001) which was developed through stripping all horizontal gradients, except the horizontal pressure gradient, from the three-dimensional numerical Delft3D code. This model accounts for buoyancy destruction in the $k$-$\varepsilon$ turbulence closure equation through inclusion of the suspended sediment concentration in the equation of state.

This approach has an additional advantage in deriving an explicit formulation of the effect of buoyancy destruction on hydraulic drag. This formulation can be used for analysis of laboratory of field data, and/or in depth-averaged numerical models, which, of course, cannot account for these effects.

In our parameterization we propose an explicit algebraic correction of the friction parameter as a function of water depth, suspended sediment concentration and sediment's settling velocity. We start from Barenblatt's (1953) log-linear velocity profile, based on the Monin-Obkhov length scale, which was derived for the atmospheric boundary layer. This method does not account for the effects of free surface, as in open channel water flows, which cause a decrease in mixing length, hence eddy diffusivity towards the water surface. As a result, sediment-induced stratification effects in open water flows are initiated near the water surface, as was shown conclusively by Soulsby and Wainwright (1987). Therefore, Barenlblatt's profile is slightly modified, yielding:

$$\frac{u}{u_*} = \frac{1}{\kappa}\left[\ln\left(\frac{z}{z_0}\right) + \alpha_1\left(\frac{z}{\ell}\right)^m\right] \tag{1}$$

where $u(z)$ = flow velocity, $u_*$ = shear velocity, $\kappa$ = von Kármán constant, $z$ = vertical coordinate and $z_0$ = roughness height in neutral conditions. In this analysis we study stationary, uniform flows only. The Monin-Obukhov length scale $\ell \equiv \rho_b u_*^3 / \kappa g \overline{\rho' w'}$ can be regarded as a measure for the turbulent mixing length in stratified flow. Equation (1) can be integrated analytically over the water depth $h$:

$$\frac{\bar{u}}{u_*} = \frac{C_{eff}}{\sqrt{g}} = \frac{1}{\kappa}\left[\ln\left\{\frac{h}{z_0}\right\} - 1\right] + K_1 h\left(\frac{gh(\rho_b - \rho_w)}{\rho_b u_*^2}\frac{\sigma_T W_s}{\kappa u_*}\right)^m = \frac{C_0}{\sqrt{g}} + K_1\left(\mathbf{Ri}_* \beta\right)^m \tag{2}$$

where $C_{eff}$ = the effective Chézy coefficient, $C_0$ is the Chézy coefficient under neutral conditions, and $\mathbf{Ri}_*$ and $\beta$ are the bulk Richardson number and the Rouse number, respectively, as defined in Equation (2). The coefficients $K_1$ and $m$ are determined from a large number of numerical experiments with a 1DV model, which accounts for sediment-induced buoyancy effects on the turbulent flow properties. Initially, we have used the standard Prandtl-Schmidt number, i.e., $\sigma_T$ = 0.7. Figure 1 shows some results of these experiments. On the basis of these results we found that $m \approx 1$–$1.3$ and $K_1 \approx 0.7h^{1.5}$. The larger values for $m$ are found at larger water depth. The dependence of $K_1$ on $h$ seems to be a consequence of the effects of the free water surface, which are not included in the original Monin-Obokhov length scale. Our numerical findings imply that drag reduction by sediment-induced buoyancy destruction can explain only about 5–10% of the observed effects.

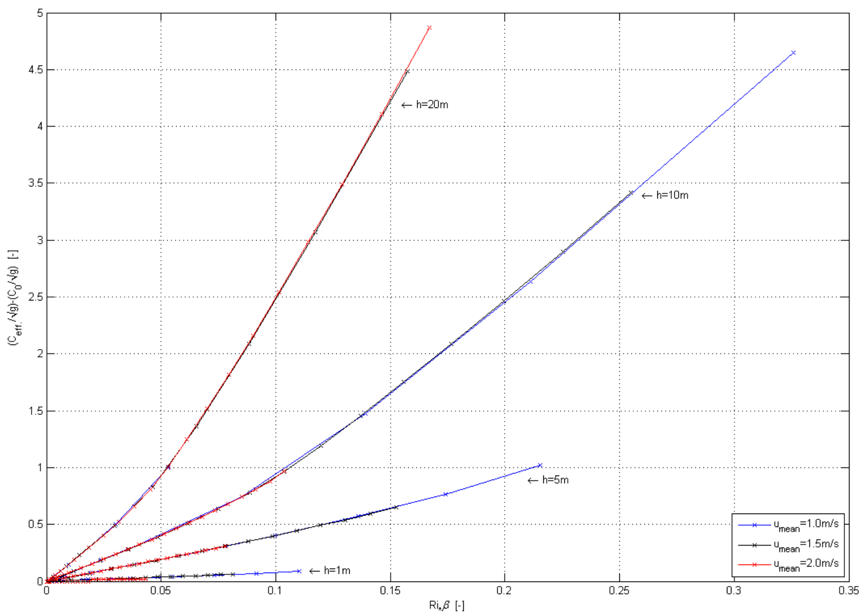


Figure 1. Variation of normalized effective Chézy coefficient (i.e., $(C_{eff} - C_0)/\sqrt{g}$) with $\mathbf{Ri}_*\beta$ at various water depths.

Therefore, we repeated our analysis, but now for $\sigma_T = 2.0$, a much larger value suggested by an analysis of laboratory data by Cellino and Graf (1999), as discussed in Winterwerp (2006). We note that a larger $\sigma_T$ implies a smaller eddy diffusivity, hence larger concentration gradients and more drag reduction. It is stressed that we do have physical evidence that the Prandtl-Schmidt number should be so large; however, with this value in our 1DV-model various field and laboratory observations could be reproduced properly (e.g., Winterwerp, 2006). With is larger coefficient, the effects of buoyancy destruction become appreciable at larger water depth, i.e., up to 30%. For other cases, these buoyancy effects cannot explain the reported reductions in hydraulic drag properly. Therefore, we conclude that the effects of a reduction in bed forms and/or a thickening of the viscous sub-layer should contribute to the observed reductions in hydraulic drag.

## References

Barenblatt, G.F. (1953), On the motion of suspended particles in a turbulent stream, Prikladnaja Matematika i Mekhanika, 17, 261–274. (English translation.)

Beardsley, R.C., Candela, J., Limeburner, R., Geyer, W.R., Lentz, S.J., Castro, B.M., Cacchione, D., Carneiro, N. (1995), The $M_2$ tide on the Amazon shelf, *Journal of Geophysical Research*, 100, 2283–2319.

Cellino, M., Graf, W.H. (1999), Sediment-laden flow in open channels under non-capacity and capacity conditions, ASCE, Journal of Hydraulic Engineering, 125(5), 456–462.

Dong, L., Wolanski, E., Li, Y. (1997), Field and modelling studies of fine sediment dynamics in the extremely turbid Jiaojianng River estuary, China, *Journal of Coastal Research*, 13(4), 995–1003.

Dyer, K.R. (1997), *Estuaries. a physical introduction*. Chichester, England. John Wiley and Sons.

Gust, G. (1976), Observations on turbulent-drag reduction in a dilute suspension of clay in sea water, *Journal of Fluid Mechanics*, 75(1), 29–47.

Guan, W.B., Wolanski, E., Dong, L.X. (1998), Cohesive sediment transport in the Jiaojiang River Estuary, China, *Estuarine, Coastal and Shelf Science*, 46, 861–871.

Le Hir, P. (1994), *Mathematical modeling of cohesive sediment and particulate contaminants transport in the Loire Estuary*. In: Thouvenin, Bolsen &Olsen, Fredensborg, Denmark, pp71–78.

Le Hir, P., Cayocca, F. (2002), *3D application of the continuous modelling concept to mud slides in open seas*. In: J.C. Winterwerp and C. Kranenburg, Fine Sediment Dynamics in the Marine Environment, Elsevier, Proceedings in Marine Sciences, Vol 5, pp545–562.

Lumley, J.L. (1969), *Drag reduction by additives*. In: Annual Review of Fluid Mechanics, Vol 1, Sears, W.R., van Dyke, M. (Eds.), pp367–383.

Odd, N.V.M., Cooper, A.J. (1988), A two-dimensional model of the movement of fluid mud in a high energy, INTERCOH-1988. In: Mehta, A.J., Hayter, E.J. (Eds.) 1989. High Concentration Cohesive Sediment Transport, *Journal of Coastal Research, Special Issue No. 5*, Summer 1989, 185–194.

Soulsby, R.L., Wainwright, B.L.S.A. (1987), A criterion for the effect of suspended sediment on near-bottom velocity profiles, *Journal of Hydraulic Research*, 25(3), 341–356.

van Rijn, L.C. (1993), *Principles of sediment transport in rivers, estuaries and coastal seas*, AQUA Publications, The Netherlands.

Wang, Z.Y., Larsen, P., Nestmann, F., Dittrich, A. (1998), Resistance and drag reduction of flows of clay suspensions, ASCE, *Journal of Hydraulic Engineering*, 124(1), 41–49.

Weilbeer, H. (2005), *Numerical simulation and analysis of sediment transport processes in the Ems-Dollard estuary with a three-dimensional model*. In: Sediment and Ecohydraulics, INTERCOH 2005, Elsevier, Proceedings in Marine Science, Kusuda, T., Yamanishi, H., Spearman, J., Gailani, J.Z. (Eds.), pp447–462.

Winterwerp, J.C. (2006), Stratification effects by fine suspended sediment at low, medium and very high concentrations, *Journal of Geophysical Research*, 111(C05012), doi:10.1029/2005JC003019.

# Advection and diffusion versus mussel filtration in a tidal channel

JOHN H. SIMPSON, BARBARA BERX

School of Ocean Sciences, College of Natural Science, Bangor University,
Menai Bridge, Anglesey LL59 5AB UK
email: j.h.simpson@bangor.ac.uk, ospe45@bangor.ac.uk

*Keywords: phytoplankton, chlorophyll, mussels, analytical model; Menai Strait, UK*

## ABSTRACT

In a previous study (Tweddle et al., 2005) we reported on an initial investigation of the factors affecting the food supply to benthic filter feeders in the Menai Strait, a tidally energetic channel with a strong non-tidal residual flow which is host to a large managed population of mussels (*Mytilus edulis* L.). Measurements of the cycle of phytoplankton (via chlorophyll concentration, Chl) at fixed locations over the mussel bed and at a control site led to the formulation of simple conceptual and analytical models of the interaction of flow, turbulent stirring and filtration in the channel. In this contribution, we present new and more extensive observations of the temporal variation and distribution of Chl and compare the results with new numerical versions of the basic conceptual model which explain the principal features of our observations.

### The Menai Strait physical regime

The Menai Strait (Figure 1) is a narrow channel, ~30 km long, situated between the Isle of Anglesey and the mainland of Wales. It connects Caernarfon Bay in the south to Liverpool Bay in the Northern Irish Sea. Because of large difference in the tidal range between the two ends, it experiences strong tidal flows, with speeds of up to 2.5 m $s^{-1}$ during spring tides in the central shallow area (the Swellies) and also at the South West entrance (Rippeth et al., 2002). This large tidal flow, coupled with the shallow water depths, results in rectification of the tidal currents and a net through flow from north-east to south-west. The magnitude of the flow varies between 330 and 800 $m^3$ $s^{-1}$ at neaps and spring tides respectively (Simpson et al., 1971; Campbell et al., 1998). The large tidal flows induce high levels of turbulence and Reynolds stress, which follow a semidiurnal pattern (Rippeth et al., 2002) with greater stresses during ebb (to SW) flow (~3 Pa) than flood (~2 Pa) in the central section of the strait. The associated high levels of vertical mixing ensure that the water column is generally well-mixed and vertically homogeneous in temperature and salinity.

The strong residual transport (mean ~530 $m^3$ $s^{-1}$), which is equivalent to a major river flowing through the channel, advects water properties, dissolved and suspended, from the northern Irish Sea into the strait. This persistent import of material is a major feature of the local ecosystem and distinguishes the channel system from, for example, estuaries where there is no net through-flow apart from the volume transport associated with river inflow. The transport of plankton into the Menai Strait is of particular importance to the large, commercial mussel beds of *M. edulis* which are located in the north-eastern end of the strait.

### Mussel filtration versus supply by advection and diffusion

Generally, mussels consume phytoplankton as their primary source of nutrition (Prins et al.,1991) and this food source may be produced either locally in the overlying waters or imported. In the case of the Menai Strait, the strong net through-flow implies limited residence times for water in the strait (~2–3 days), which is too short for local production to contribute significantly. The inference is that a high proportion of the food supply to the mussels is carried into the Menai Strait by the net transport from the Irish Sea which exhibits high plankton concentrations, particularly during spring bloom conditions (Gowen et al., 1999). This ready supply of imported plankton was postulated by Tweddle et al. (2005) to be the critical factor facilitating the high production of the commercial mussel beds (~10,000 tonnes per annum). It may also be the reason for the existence of large wild mussel beds in the strait prior to the development of the present commercial farming of mussels.

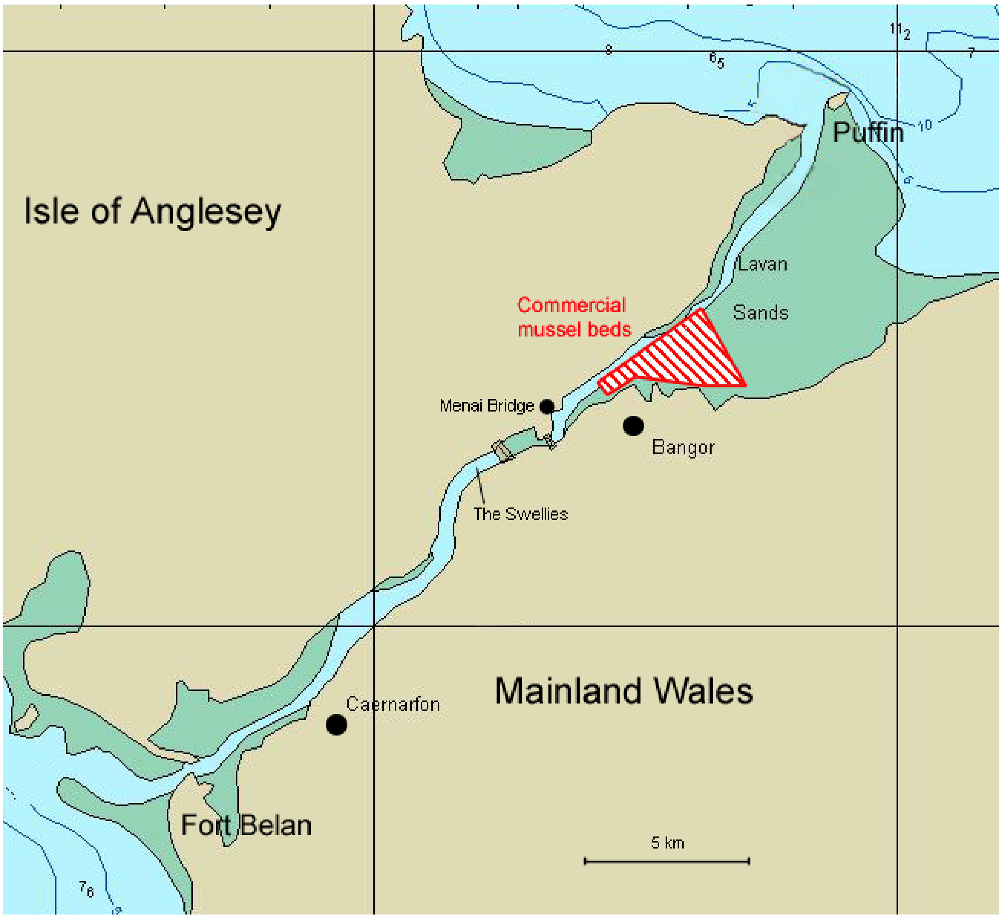


Figure 1. The Menai Strait, showing the location of the mussel beds.

The measurements of Tweddle et al. (2005) indicated two key features of the system which supported the advection hypothesis, namely (i) the presence of a pronounced gradient in Chl between the north-eastern entrance and the centre of the channel (Menai Bridge in Figure 1), (ii) regular semi-diurnal oscillations of Chl by a factor of ~2 over the mussel bed which were clearly related to the current regime. The conceptual model that emerged (see Figure 3) is one in which phytoplankton filtration over the mussel beds reduces water column concentrations and creates horizontal and vertical gradients in concentration. The reduction of plankton concentration is opposed by advection due to the mean flow which acts on the concentration gradient to re-supply the water column downstream. Advection of the gradient by the tidal currents results in the large oscillations of concentration observed. Intensive mussel filtration may also lead to significant depletion of Chl in the lower part of the water column but given the intensity of tidal mixing in the Menai Strait, downward diffusion of plankton should prevent depletions for most of the tidal cycle.

## Observational results

New observations of the tidal cycle of Chl and flow were undertaken during the periods 10–12 September 2004, 23–25April 2005 and 11–15 August 2005. During the latter period, the longitudinal gradient of Chl was also determined. These measurements were designed to assess whether or not the earlier measurements in April 2002 were representative of conditions over the mussel beds. The observational procedure was based on regular profiling and water sampling from the R.V. Prince Madog which was moored fore and aft to maintain a closely consistent position over the mussel beds. In parallel with the shipboard observations, measurements of the velocity field were made by a bottom mounted RDI 1.2 MHz Workhorse ADCP located close to the moored vessel.

An example of the time series data for Chl, depth mean flow velocity and tidal height is shown in Figures 2. Note the pronounced semidiurnal oscillation in the Chlorophyll concentration which varies by at least a factor of 2 over the tidal cycle.

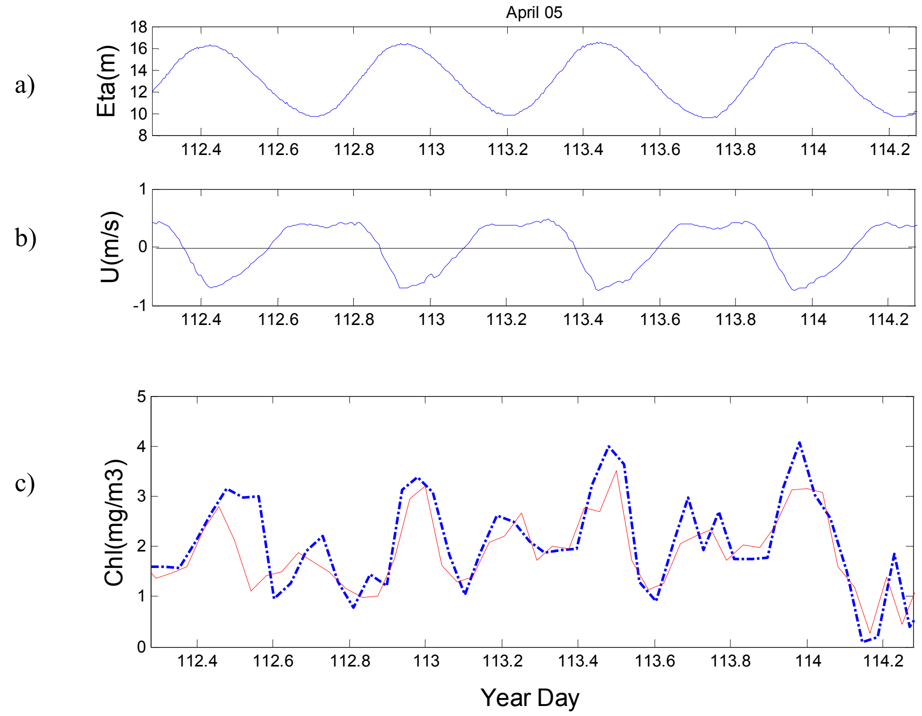


Figure 2. 48-hour time series at position 53°14.619′N, 4°07.360′W on 23–25 April 2005: (a) Tidal elevation, (b) Depth mean velocity $U$(m s$^{-1}$), (c) Chl (mg m$^{-3}$): dash-dot = near bed; continuous = near surface.

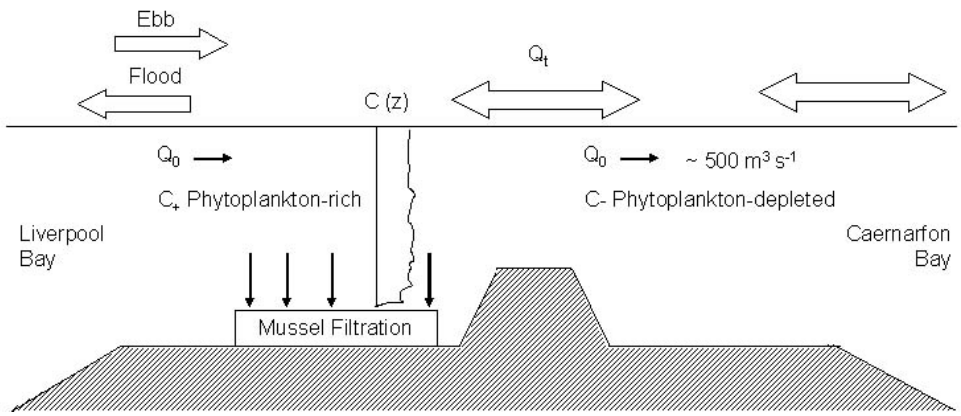


Figure 3. Conceptual model of flow and food supply to mussels. Rectification of the strong tidal flow $Q_t$ generates a residual flow $Q_0$ from NE to SW which imports phytoplankton into the straits and over the mussel beds where concentrations are reduced by mussel grazing establishing a strong gradient along the channel.

In this case, there is also a significant quarter diurnal ($M_4$) variation, involving a second weak maximum, apparent in the tidal cycle. In addition to the time series observations, the along-channel variation of Chl has been observed by continuous measurement using the flow-through system on the R.V. Prince Madog in August 2005. These results demonstrate the existence of strong gradients in the strait, with the Chl concentration decreasing by a factor of ~1.5 between the north-east entrance and Menai Bridge.

## Model development

In order to demonstrate the operation of the essential processes (shown in the schematic of Figure 3) and with the aim of explaining the principal features of the observations, we have developed a combination of models starting from a 1-D model of tidal and residual flow in the strait. The output of this model is used in the same 1-D framework to explore the interaction between the transport of plankton by the flow and the filtration by mussels. The physical model is forced only by tidal elevations at the ends of the channel while the source of plankton is simulated by maintaining a uniform concentration at the north-east end of the channel. In a further development, this model is extended to two dimensions over the mussel beds in order to simulate the effects of vertical diffusion in controlling the supply of plankton to the near bed layers and to determine the conditions that may lead to depletion.

## Model results

The tidal and residual flows of the 1-D model transport the phytoplankton over the mussel bed where the intensive filtration results in the creation of the phytoplankton gradient whose magnitude is comparable to that observed. The model also convincingly simulates the form, magnitude and phase of the tidal oscillations in Chl concentration observed over the mussel bed including the large $M_4$ component which is associated with the tendency for the cycle to include a double maximum. The model reveals that the occurrence of this latter feature is associated with a minimum in the along channel Chl profile which develops under spring tide conditions due to variations in the transit time of water particles over the mussel bed. This effect is less apparent at neap tides when velocities are weaker and filtration tends to establish a more uniform spatial gradient. The weaker residual flow at neap tides also involve longer transit times through the strait with the consequence that extraction rates are greater than at spring tides.

## References


Campbell, A.R., Simpson, J.H., Allen, G.L., (1998), The dynamical balance of flow in the Menai Strait, *Estuarine, Coastal and Shelf Science*, 46(3), 449–455, doi:10.1006/ecss.1997.0244.

Gowen, R.J., Stewart, B.M., Mills, D.K., Elliott, P. (1995), Regional differences in stratification and its effect on phytoplankton production and biomass in the north western Irish Sea, *Journal of Plankton Research*, 17, 753–769.

Prins, T.C., Smaal, A.C., Pouwer, A.J., (1991), Selective ingestion of phytoplankton by the bivalves *Mytilus edulis* L. and *Cerastoderma edule* (L.), *Hydrobiological Bulletin*, 25, 93–100.

Rippeth T.P., Williams, E., Simpson, J.H. (2002), Reynolds stress and turbulent energy production in a tidal channel, *Journal of Physical Oceanography*, 32, 1242–1251.

Simpson, J.H., Forbes, A.M.G., Gould, W.J. (1971), Electromagnetic observations of water flow in the Menai Straits, *Geophysical Journal of the Royal Astronomy Society*, 24, 245–253.

Tweddle, J.F., Simpson, J.H., Janzen, C.D. (2005), Physical controls of food supply to benthic filter feeders in the Menai Strait, U.K., *Marine Ecology Progress Series*, 289, 79–88.

# The Columbia River plume in the U.S. Pacific Northwest upwelling system: cross-shelf dispersion and export of primary production

NEIL S. BANAS[1], EVELYN J. LESSARD[1], RAPHAEL M. KUDELA[2], PARKER MACCREADY[1]

1. School of Oceanography, University of Washington, P.O. Box 355351, Seattle WA 98195-5351, USA
   email: neil@ocean.washington.edu, elessard@u.washington.edu, parker@ocean.washington.edu

2. Ocean Sciences Department, University of California, Santa Cruz, 1156 High Street, Santa Cruz CA 95064-1077, USA
   email: kudela@ucsc.edu

*Keywords: river plumes, primary production, dispersion, ecosystem modeling, upwelling*

## ABSTRACT

Along the U.S. Pacific Northwest coast, a highly productive upwelling system interacts with a range of mesoscale features: topographic eddies, canyons, macrotidal estuaries, and multiple strong freshwater inputs. A biophysical model of the region was developed to examine the effect of the Columbia River plume (Figure 1) on the fate of upwelling-derived primary production, as part of the NSF-sponsored River Influences on Shelf Ecosystems (RISE) program. Results suggest that the plume may act as a cross-shelf exporter and semi-permeable along-coast barrier to biological production, through intermittent, dispersive interactions with the coastal circulation.

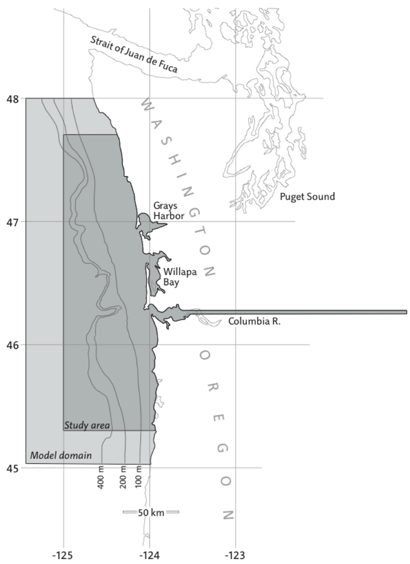


Figure 1. Model domain and study area.

## Plume effects on coastal circulation

Upwelling on the Northwest coast is highly time-dependent. Events in which the large-scale winds not only relax but actively reverse are common throughout the year. Under northward wind (downwelling favorable) conditions, the Columbia River plume tends northward and onshore along the Washington coast, but within 1-2 days of a return to upwelling-favorable conditions, the plume rapidly advects offshore. Hickey et al. (2005) have shown that because of these wind reversals, there is almost always some amount of plume water off Washington year-round: the summertime Columbia plume should be thought of as bidirectional. In other words, the most typical summer conditions in this region are not 'upwelling-favorable' per se, but rather 'upwelling-favorable with a downwelling event a few days in the past'.

The circulation model (MacCready et al., 2008: Figure 1) is implemented using ROMS (Regional Ocean Modeling System, Rutgers version 2.2). Horizontal resolution is ~500 m at the mouth of the Columbia, telescoping out to ~7 km at the northwestern and southwestern corners. The Columbia River beyond a point 50 km upstream of the mouth is replaced by a straight 3 km-wide, 3 m-deep channel, to allow tidal energy to propagate freely past the estuary. A three-month hindcast of Jun–Aug 2004 was performed, using time-varying atmospheric forcing, variable riverflow, and tides. Hourly wind and atmospheric forcing is taken from the 4 km Northwest Modeling Consortium MM5 regional forcecast model. Boundary conditions for tracers, subtidal velocity, and subtidal surface height come from the NCOM CCS model (Navy Coastal Ocean Model, California Current System: Kara et al., 2006). Overall model skill (combining measures for sainity, sea level, and currents, both near-surface and deep, for the Columbia estuary, plume, and oceanic far field) is 0.65 (Liu et al., in prep).

An intensive Lagrangian particle-tracking analysis of this hindcast was conducted, in a pair of model cases with and without the Columbia River included, in order to isolate the effect of the plume on the coastal circulation. The summary answer is that the plume disperses water that upwells off Washington over a very broad area (Figure 2).

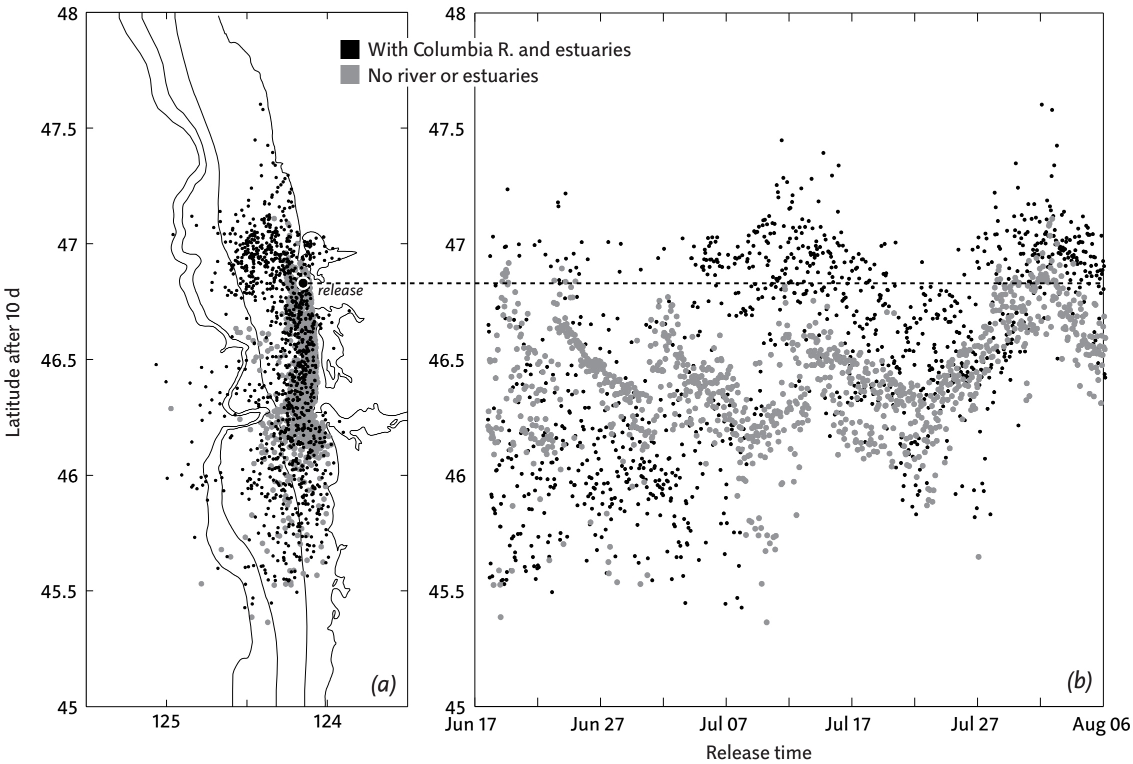


Figure 2. Location after 10 d of transport of particles released continuously at 46.83°N, in plan view (a) and arrayed by release time (b). The Columbia River increases both cross-shelf dispersion and alongcoast dispersion, as well as amplifying differences between wind events on the 2–10 d scale.

The bidirectionality of the Columbia River plume is an essential part of this process: even weak remnants of downwelling plumes can still have important effects on the fate of coastal water on the Washington shelf. Overall, over 20 d, ~25% more water is exported laterally from the Washington nearshore past the 100 m isobath when the Columbia River plume is included in the model. This lateral export causes a net diversion of Washington coastal production away from the inner shelf south of the river mouth. Thus we expect that the northern Oregon upwelling system 'resets' much the way that upwelling centers in the lee of small headlands do.

## Plume effects on primary production

But are these plume-related, transient circulation patterns biologically significant? How do the relevant physical timescales compare with the key biological timescales in this upwelling system: the phytoplankton community growth rate and the zooplankton community grazing rate? Quantitatively, how much does the presence of the Columbia River plume affect summer patterns of biomass and primary production? To answer these questions, we added planktonic nutrient cycling to the circulation model, with particular attention to phytoplankton and zooplankton community rates. The biological model is a custom nitrogen budget which tracks nutrients, phytoplankton, zooplankton, and detritus (NPZD) in every grid cell (Figure 3): it is implemented using a modified version of the ROMS `fasham.h` module. Crucially, zooplankton ingestion rate, mortality rate, and most other model parameters were determined empirically rather than by tuning, by evaluating equilibrium versions of the model equations using a rich biological dataset obtained during RISE cruises in summers 2004 and 2005. We believe this is the first time that a simple NPZ-type model has been validated against simultaneous field measurements of phytoplankton biomass (Figure 4), zooplankton biomass, community growth, and community grazing.

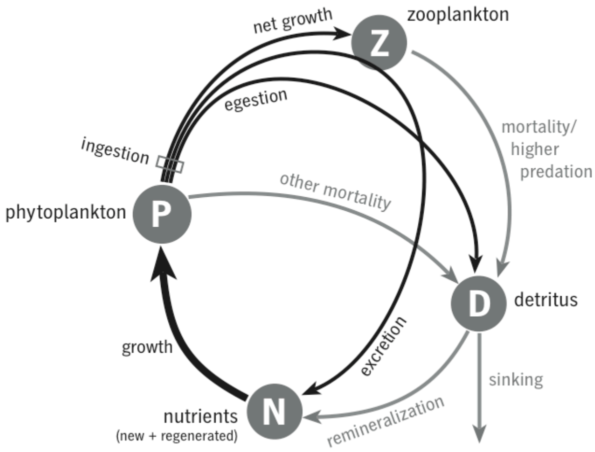


Figure 3. Schematic of the ecosystem model.

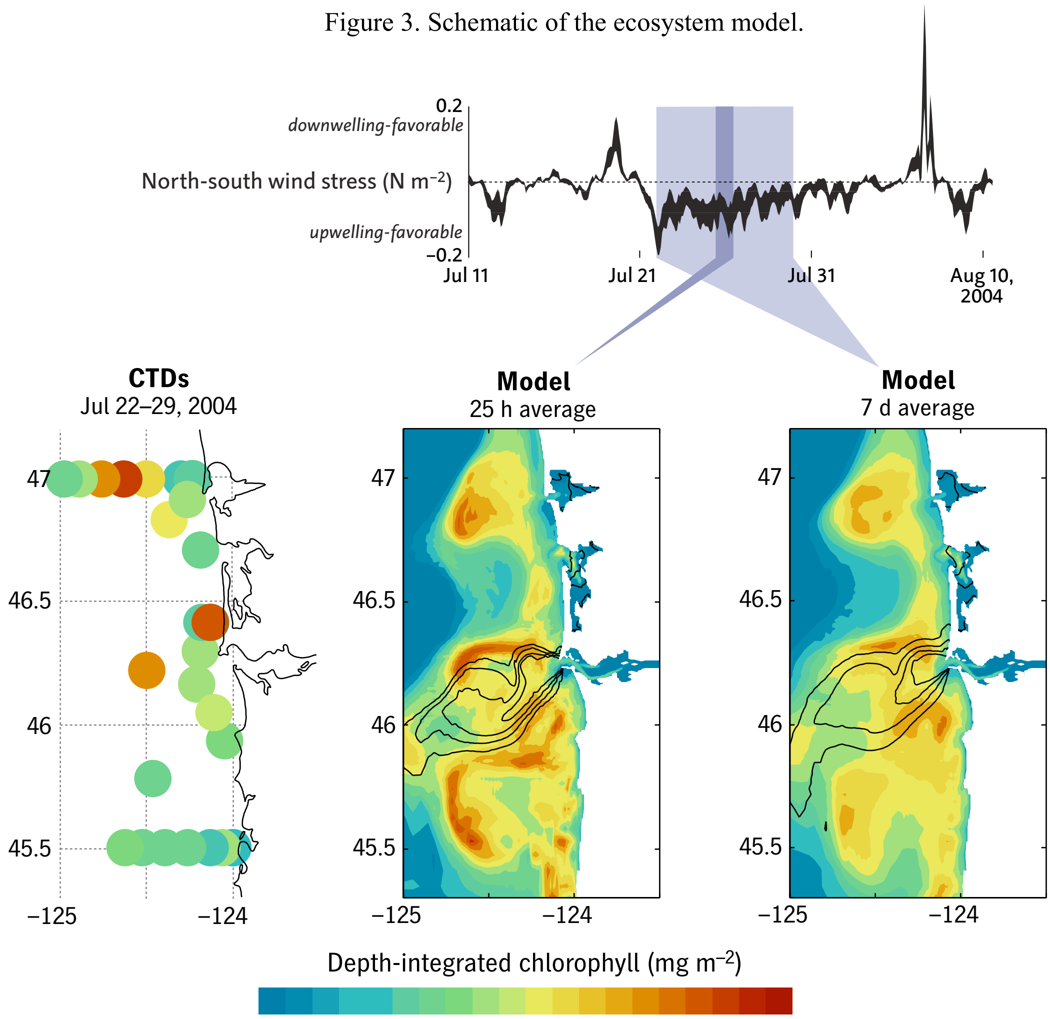


Figure 4. Vertically integrated chlorophyll biomass from CTD observations and the model, during a sustained upwelling event in late July 2004.

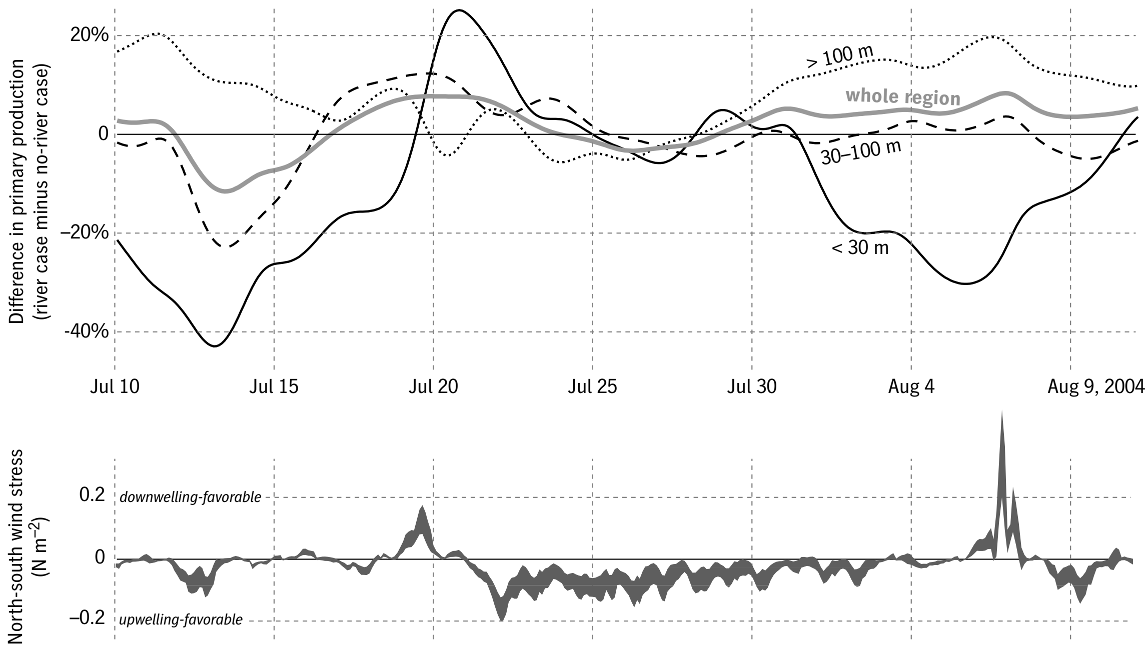


Figure 5. Relative difference in primary production (by depth range, over time) between model cases with and without the Columbia River. A positive difference means increased primary production in the presence of the plume.

Time series of integrated primary production were calculated for the entire region between 45.5 and 47°N (see Figure 1), subdivided into three depth ranges: the inner shelf (water depths <30 m), mid shelf (30–100 m), and the outer shelf and slope. Comparing results for the model cases with and without the Columbia River (Figure 5) confirms that the cross-shelf export (in a hydrodynamic sense) identified by Lagrangian analysis is indeed reflected in patterns of primary production. In the presence of the plume, ~20% less primary production occurs over the inner shelf, and ≤20% more occurs over the outer shelf and slope. This effect is strongest under weak and variable upwelling-favorable winds.

## References

Hickey, B.M., Geier, S., Kachel, N., MacFadyen, A. (2005), A bi-directional river plume: The Columbia in summer, *Continental Shelf Research*, 25, 1631–1656.

Kara, A.B., Barron, C.N., Martin, P.J., Smedstad, L.F., Rhodes, R.C. (2006), Validation of interannual simulations from the 1/8 degree global Navy Coastal Ocean Model (NCOM), *Ocean Modelling*, 11, 376–398.

MacCready, P., Banas, N.S., Hickey, B.M., Dever, E.P. (2008), A model study of tide- and wind-induced mixing in the Columbia River estuary and plume, *Continental Shelf Research*. (In press.)

# Estuarine mechanical energy: reservoirs and fluxes

PARKER MACCREADY[1], W. ROCKWELL GEYER[2]

1. School of Oceanography, University of Washington, P.O. Box 355351,
Seattle WA 98195-5351, USA
email: parker@ocean.washington.edu

2. Woods Hole Oceanographic Institute, 266 Woods Hole Road,
Woods Hole MA 02543-1050, USA
email: rgeyer@whoi.edu

*Keywords: energy, buoyancy flux, mixing, tides, exchange flow*

## ABSTRACT

Subtidal estuarine mechanical energy budgets are considered, using theory and an idealized model. Attention is given to the effects of tidal averaging, fluxes through the river and ocean open boundaries, and the definition of the zero available potential energy (APE) state. For a typical partially-mixed estuary the APE is dominated by the length of the salt intrusion, and is by far the largest storage ('reservoir') term. It may even be much greater than the instantaneous values of tidal kinetic or potential energy. Mixing efficiency is typically ~5%, much lower than the assumed maximum theoretical efficiency of 20%. A theoretical expression relating the net buoyancy flux to the strength of the overturning circulation is developed.

### Introduction

The estuarine overturning circulation involves the length of the salt intrusion, the stratification, vertical density advection, and vertical mixing of the stratification. These are all parts of the potential energy budget, so we are motivated to try to understand such budgets more fully (or at all). A global overview of ocean energy is given in Wunsch and Ferrari (2004). Considering tidal energy at the global scale (Munk, 1997; Munk and Wunsch, 1998) is it estimated that about 3.5 TW of energy is input to the tides by the sun and moon. The majority of this, 2.6 TW, is dissipated in the shallow coastal ocean. Those authors estimate that only about 4% of this, 0.1 TW, goes into 'perforations' such as bays, inlets, fjords and estuaries. A maximum of ~20% of this is thought to be available for irreversible mixing of the stratification (buoyancy flux). In studies of fjord energetics, Stigebtrandt and Aure (1989) have estimated this efficiently to be closer to 5%, presumably because much of the dissipation occurs in unstratified regions.

Changes in vertically-integrated potential energy have long been used (Simpson et al., 1990) as a way of understanding estuarine function. A number of studies have calculated barotropic tidal energy flux in real estuaries, and calculated net dissipation as either the divergence of this flux (Lavelle et al., 1988), or directly from numerically simulated shears (Zhong and Li, 2006, which also contains an excellent introduction to the literature). An important step taken by Weisberg and Zheng (2003) was to compute all terms in the volume integrated energy budget, in their case for a numerical model of Charlotte Harbor. They used this method to explore how mixing affects the tidally-averaged exchange flow. Here we re-examine the estuarine energy budget.

### Energy budget

The tidally-averaged, volume integrated mechanical energy equation in a volume with open ends can be written as

$$
\begin{aligned}
&\underbrace{\frac{d}{dt}\int_V \frac{1}{2}\rho_0\langle\mathbf{u}\rangle\cdot\langle\mathbf{u}\rangle dV}_{\text{Mean KE Storage}} + \underbrace{\frac{d}{dt}\int_{A_0} \frac{1}{2}\rho_0 g\langle\eta\rangle^2 dA}_{\text{Mean PE}_0\text{ Storage}} + \underbrace{\frac{d}{dt}\int_V gz\langle\rho_1\rangle dV}_{\text{Mean PE}_1\text{ Storage}} \\
&+\underbrace{\frac{d}{dt}\int_V \frac{1}{2}\rho_0\langle\mathbf{u}''\cdot\mathbf{u}''\rangle dV}_{\text{Tidal KE Storage}} + \underbrace{\frac{d}{dt}\int_{A_0} \frac{1}{2}\rho_0 g\langle\eta''^2\rangle dA}_{\text{Tidal PE}_0\text{ Storage}} \\
&= \underbrace{-\int_{A_{OPEN}} \langle u_n\rangle\left(\frac{1}{2}\rho_0\langle\mathbf{u}\rangle\cdot\langle\mathbf{u}\rangle + gz\langle\rho_1\rangle\right)dA}_{\text{Mean KE and PE}_1\text{ Advection}} \underbrace{-\int_{A_{OPEN}} gz\left\langle\rho_1''u_n''\right\rangle dA}_{\text{Tidal PE}_1\text{ Advection}} \\
&\underbrace{-\int_{A_{OPEN}} \left(\langle p_1\rangle\langle u_n\rangle + \left\langle\rho_0 g\eta''u_n''\right\rangle\right)dA}_{\text{Mean and Tidal Pressure Work on }A_{OPEN}} \\
&\underbrace{-\int_V \left(\rho_0 K_M\langle u_z\rangle^2 + gK_S\langle\rho_z\rangle\right)dA}_{\text{Mean Dissipation and Buoyancy Flux}} \underbrace{-\int_V \rho_0\left\langle K_M''u_z''u_z''\right\rangle dA}_{\text{Tidal Dissipation}}
\end{aligned}
\tag{1}
$$

A formal derivation of this (excluding the separation into tidal and tidal-mean parts) is given in MacCready et al. (2009) for example. Here the volume of integration, $V$, extends from the bottom to the free surface, and has open ends with area $A_{OPEN}$ and outward normal velocity, $u_n$. The presence of open boundaries, required for estuaries, is a problem for energy budgets because the net mass in the system can change. Although we don't go into the details here, this net mass change shows up in the energy budget in the sum of pressure work and PE advection terms integrated on the open boundaries. The velocity, $\mathbf{u}$, free surface, $\eta$, and density $\rho = \rho_0 + \rho_1(x, y, z, t)$ are divided into tidal mean (angle brackets) and tidally-varying (double prime) parts before the whole equation is volume integrated and tidally-averaged.

The energy budget naturally splits into two parts, one that pertains to mainly tidally-varying properties (e.g., 'Tidal KE Storage') and another that expresses the energy pathways of mainly tidally-averaged (e.g., 'Mean PE Storage' or 'Buoyancy Flux'). We may use the 'ETA2D' tidally-averaged numerical model (Figure 1)

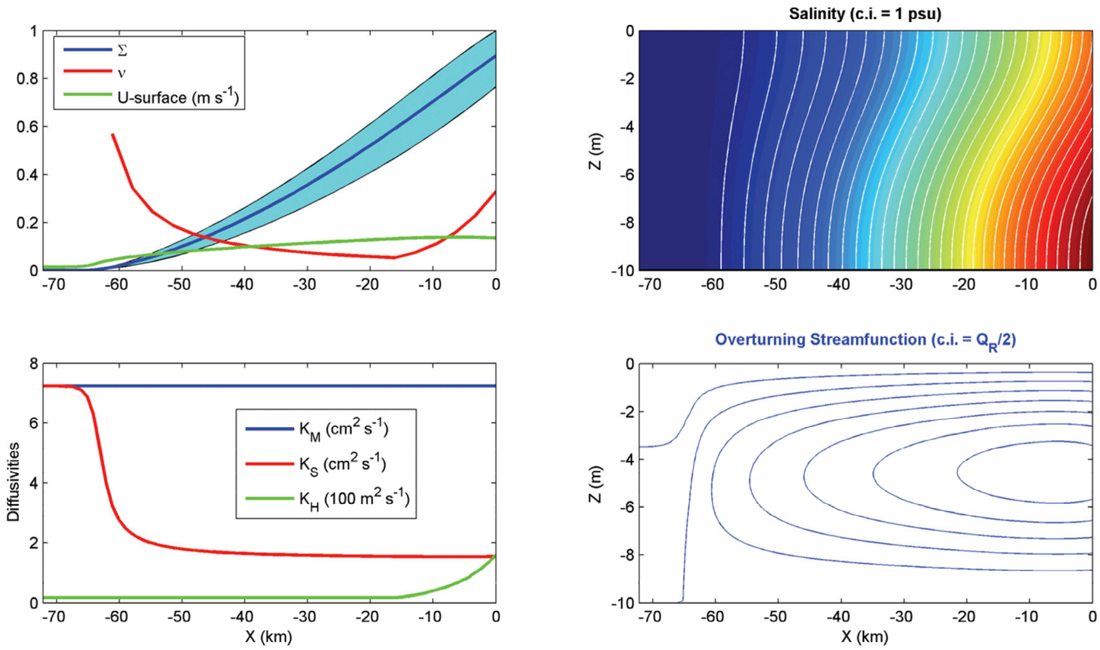


Figure 1. Estuary fields from the ETA2D model. (upper left) Along-channel distribution of salinity (Σ is the depth-averaged salinity normalized by oceanic salinity, and the light-blue band around it represents the vertical stratification). Also shown are the along-channel surface velocity and, $v$, the up-estuary fraction of diffusive salt flux. (upper right) A salinity section. (lower left) Distribution of the effective vertical eddy viscosity, $K_M$, eddy diffusivity, $K_S$, and the horizontal diffusivity, $K_H$. (lower right) Overturning stream function normalized by the river flow.

developed in MacCready (2004, 2007) to evaluate the tidally average terms. The results are shown in Figure 2. The terms in the tidal budget (shown in red in Figure 2) are tied to the tidal-mean budget mainly through the vertical eddy diffusivity, which derives all of its energy from the tidal currents.

There are several notable aspects to the budget shown in Figure 2. The first is that the stored APE (Available Potential Energy) is huge, being even ten times greater than the average KE or PE of the tides. The background state used to define what is 'Available' is one in which the river and tides are turned off, so the free surface is flat and the estuary (up to the limit of the salt intrusion shown in Figure 1) is filled with salt water. Further analysis shows that (i) very little of the APE is stored in the mean surface height deformation, and more surprisingly (ii) most of the APE is stored in the horizontal salt gradient, *not* in the vertical stratification. This large APE reservoir contained in the length of the salt intrusion thus may function as a powerful control on estuarine dynamics – you have to do a lot of work to change it much, and the system has a substantial memory. Another interesting point to emerge in Figure 2 is that the net buoyancy flux is only about 4% of the net tidal dissipation (one might have expected more like 20% if the estuary was mixing at maximum efficiency). However result should depend on the details of the mixing parameterizations used, and these are highly simplified in this case, so we probably should not look to a model like ETA2D to tell us about actual mixing efficiencies, although it may be useful for exploring the variation of mixing efficiency across different systems. Also evident in Figure 2 are the two points of connection between the PE and KE budgets, the Uplift term (volume integral of $\rho_1 gw$), and the open boundary pair (Mean Pressure Work and Mean PE Advection). Notably, the two open boundary terms are almost identical (meaning they would vanish in the full PE + KE budget). One may show that this is exactly true for the parts of these terms arising from the local depth-averaged density at the location of the open boundary.

## Conclusions

While it is useful to be able to calculate such budgets, they only become meaningful when we can form simple parameterizations of the various terms, or use scaling to eliminate terms. One such parameterization, used in calculating the Tidal Dissipation term in Figure 2, is to equate:

$$-\int_V \rho_0 \left\langle K_M{}'' u_z{}'' u_z{}'' \right\rangle dA \approx -\frac{4}{3\pi}\rho_0 C_D \int_{A_0} U_T{}^3 dA \tag{2}$$

where $U_T$ is the amplitude of the depth averaged tidal velocity, and $C_D$ is a drag coefficient. Of greater interest is a relation between the tidally-averaged estuarine exchange flow and the Buoyancy Flux. Assuming that the depth-averaged salinity decreases linearly along the length of the estuary, and that the buoyancy flux is evenly distributed along the system, one may show that

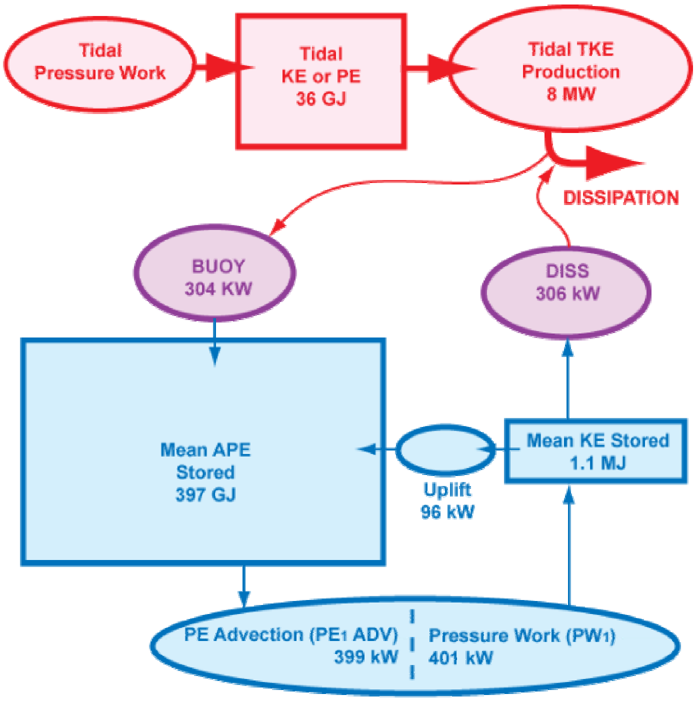


Figure 2. Terms in the energy budget for the estuary shown in Figure 1. Terms in boxes represent net energy (Joules) and ovals give values of the flux terms (Watts). The terms in red/pink are estimated from known properties of the tidal currents, while the terms in blue and purple come from ETA2D model fields. The terms in ovals correspond to terms in Equation (1), while terms in boxes, the reservoirs, represent mean values of the storage terms in (1) prior to taking the time derivative.

$$-\int_V gK_S \langle \rho_z \rangle dA \approx \frac{gH}{4} Q_2 \rho_{1ocn} \qquad (3)$$

where $H$ is the estuary depth, $Q_2$ is the volume flux of the deep inflow of the estuarine circulation, and $\rho_{1ocn}$ is the oceanic value of the density anomaly. Under steady circumstances this may be rewritten in terms of the riverflow using the Knudsen relation. The final expression demonstrates the strong link between the exchange flow and the buoyancy flux.

## References


Lavelle, J.W., Mofjeld ,H.O., Lempriere-Doggett, E., Cannon, G.A., Pashinski, D.J., Cokelet, E.D., Lytle, L., Gill, S. (1988), *A multiply-connected channel model of tides and tidal currents in Puget Sound, Washington and a comparison with updated observations*. NOAA Tech. Memo. ERL PMEL-84 (PB89-162515), 103pp.

MacCready, P. (2004), Toward a unified theory of tidally-averaged estuarine salinity structure, Estuaries, 27, 561–570.

MacCready, P. (2007), Estuarine adjustment, *Journal of Physical Oceanography*, 37, 2133–2145.

MacCready, P., Banas, N.S., Hickey, B.M., Dever, E.P. (2009), A model study of tide- and wind-induced mixing in the Columbia River estuary and plume, *Continental Shelf Research*. (In press.)

Munk W. (1997), Once again: once again – tidal friction source, *Progress in Oceanography*, 40(1), 7–35.

Munk, W., Wunsch, C. (1998), Abyssal recipes II: energetics of tidal and wind mixing, *Deep Sea Research Part I: Oceanographic Research Papers*, 45(12), 1977–2010.

Simpson. J.H., Brown, J. Matthews, J., Allen, G. (1990), Tidal straining, density currents, stirring in the control of estuarine stratification, *Estuaries*, 26, 1579–1590.

Stigebrandt, A., Aure, J. (1989), Vertical mixing in the basin waters of fjords, *Journal of Physical Oceanography*, 19, 917–926.

Weisberg, R.H., Zheng, L. (2003), How estuaries work: a Charlotte Harbor example, *Journal of Marine Research*, 61, 635–657.

Wunsch, C., Ferrari, R. (2004), Vertical mixing, energy, and the general circulation of the oceans, *Annual Review of Fluid Mechanics*, 36, 281–314.

Zhong, L., Li, M. (2006), Tidal energy fluxes and dissipation in the Chesapeake Bay, *Continental Shelf Research*, 26, 752–770.

# Relative importance of advective processes and eddy viscosity parameterisation in modeling estuarine flow

TJERK J. ZITMAN[1], HENK M. SCHUTTELAARS[2], SUSAN A. ELSTON[3]

1. Hydraulic and Offshore Engineering Section,
Faculty of Civil Engineering and Geosciences, Delft University of Technology,
P.O. Box 5048, 2600 GA Delft, Netherlands
email: t.j.zitman@tudelft.nl

2. Delft Institute of Applied Mathematics, Delft University of Technology, Mekelweg 4,
2624 CD Delft, Netherlands
email: h.m.schuttelaars@tudelft.nl

3. Department of Spatial Information Science and Engineering, University of Maine,
Orono ME 04469-5711, USA
email: saelston@ieee.org

*Keywords: tidal estuaries, advective momentum transfer, diagnostic modeling*

## ABSTRACT

For a proper understanding of flow patterns in curved tidal channels, quantification of contributions from individual physical mechanisms is essential. To achieve this, we present a numerical model based on the three-dimensional shallow water equations. It describes the time-dependent flow in curved channels with an (almost) arbitrary cross-channel bottom profile. In longitudinal direction uniformity is assumed with respect to both geometry and flow. Special feature of our diagnostic model is that assumptions regarding the relative importance of particular physical mechanisms can be incorporated in the computations by switching corresponding terms in the model equations on or off. We present two model applications and compare the results with those obtained in two recent studies, both based on an analytical model. For the channel geometries considered in the comparisons, it is found that advection-related forcing of the flow in transverse direction is small relative to that in along-channel direction. The distribution of this forcing over the channel cross-section seems to depend on the applied type of turbulence closure formulation. To investigate this further, a sensitivity analysis of model results to various eddy viscosity formulations is foreseen for the near future. Complementary to the mentioned recent studies, it is shown from model computations that under low flow conditions, cross-channel bottom steepness has a negligible effect on the role of tide-residual advective forcing of the flow.

## Introduction

To acquire insight into the physical processes underlying flow in cross-sections of tidal rivers and estuaries, various analytical models have been developed that have proved to be successful in reproducing and explaining many observed cross-sectional flow patterns. These models solve the shallow water equations assuming a rigid lid and uniformity in along channel direction. The water motion is forced by river discharge, tides, wind and both transverse and longitudinal pressure gradients, resulting from spatial density variations and surface slope. Furthermore, eddy viscosity is time and space invariant and advective momentum transfer in the cross-section is assumed to be of minor importance. Depending on the estuary at hand, this may be too restrictive an approach. Therefore, we present a diagnostic model that includes advection and in which eddy viscosity is assumed to be parabolically distributed over the vertical. Its magnitude depends on the flow itself and may vary with time and in transverse direction. An additional feature of the model is that individual terms in the basic model equations, each representing a specific physical mechanism, can be switched on or off. This facilitates quantification of the contributions of these mechanisms to the flow pattern.

In the present abstract, we deploy this feature to assess the role of advective momentum transfer in mildly curved tidal channels. From Huijts et al. (2007) it is evident (their figure 2) that in high flow conditions, the importance of advection increases with the steepness of the transverse bottom profile. This finding is based on an analytical model in which advection is neglected in zero order approximation. For low flow condition, Schramkowski et al. (2007) find that advection is small compared to flow driving forces related to density gradients and longitudinal surface slope. This holds for a mildly sloping bottom. To assess whether under low flow conditions the importance of advection varies also with bottom steepness, we consider a schematized transverse bottom profile with a relatively steep part in the centre. For this profile, we run our model twice. In one of the runs advection is included, whereas it is presumed negligible in the other run. Preliminary results of these diagnostic model applications are given and discussed briefly in the present abstract.

## Model and method

The geometry we use in our model consists of a schematized bathymetry, comprising vertical walls on either side of the channel and a smoothly varying bottom in between. Although parts of this bottom may be steep, vertical jumps cannot be accommodated. The shape of the cross-section and the flow itself are assumed uniform in along-channel direction. This holds also for the radius of curvature. The flow is described by the three-dimensional shallow water equations (including horizontal diffusion) and it is forced by a combination of prescribed transverse and lateral density gradients, a prescribed lateral pressure gradient due to a surface slope, a prescribed wind shear stress and earth's rotation. Instead of the lateral surface slope, a total discharge may be prescribed.

The rigid lid approximation is applied, meaning that spatial and temporal variations of the surface level elevation are neglected, although pressure gradients due to such variations are taken into account. In transverse direction, this pressure gradient is chosen such that the depth-integrated cross-channel flow velocity equals zero at all times. This implies also that water cannot enter or leave the channel across its side walls.

Corresponding boundary conditions comprise zero velocities at the two side walls and at the bottom (no-slip conditions). Consistent with the rigid lid approximation, the vertical velocity at the surface is set to zero. Furthermore, vertical gradients of the two horizontal velocity components at the water surface are associated to wind shear stress.

The vertical eddy viscosity is assumed to vary parabolically over the water column. One of the zero-crossings of this parabola is located slightly below the level where the no-slip condition is applied. The distance between the two is chosen in correspondence with the bottom roughness. This approach is similar to Prandtl's mixing length concept applied to plane shear flow. To avoid singularities in the model computations, the other zero-crossing is chosen just above the surface level. The corresponding viscosity scale (depth-averaged value) depends on the flow itself and may vary in transverse direction.

Flow velocity components are solved numerically using a collocation method based on Chebyshev polynomials (see e.g., Boyd, 2000). In the physical domain, we use a non-orthogonal curvilinear grid with a relatively high resolution near the bottom and the side walls to achieve proper representation of boundary layers. The physical domain is mapped onto a rectangular computational domain. This is performed such that seen in both directions, grid points in the computational domain coincide with collocation points. For integration in the time domain, a fully implicit finite difference approximation is applied. This is achieved by performing a Newton-Raphson iteration in each time step.

## Preliminary results and discussion

Two diagnostic model applications are presented in this abstract. The first one is meant to introduce our model and also as a preliminary model validation. It concerns a channel with a smoothly varying transverse bottom profile. This resembles a situation addressed by Huijts et al. (2007). In particular, we look at a mildly curved channel (radius of curvature of the channels axis is 41.5 km) with a width of 3 km. In transverse direction, the bottom profile is cosine shaped. The water depth amounts to 3 m at the sides of the channel and to 15 m at the centre. The flow is forced by an along-channel density gradient of $4 \times 10^{-4}$ kg m$^{-4}$, a cross-channel density gradient of $3 \times 10^{-4}$ kg m$^{-4}$ and also by earth's rotation (Coriolis parameter equal to $1.2 \times 10^{-4}$ s$^{-1}$). In addition, an along-channel pressure gradient due to a tide-induced surface slope is imposed. It varies cyclically with an amplitude of $10^{-5}$ and a frequency equal to that of the $M_2$ tidal constituent. Wind is not considered in this application. The scale of vertical eddy viscosity is fixed at 0.03 m$^2$ s$^{-1}$.

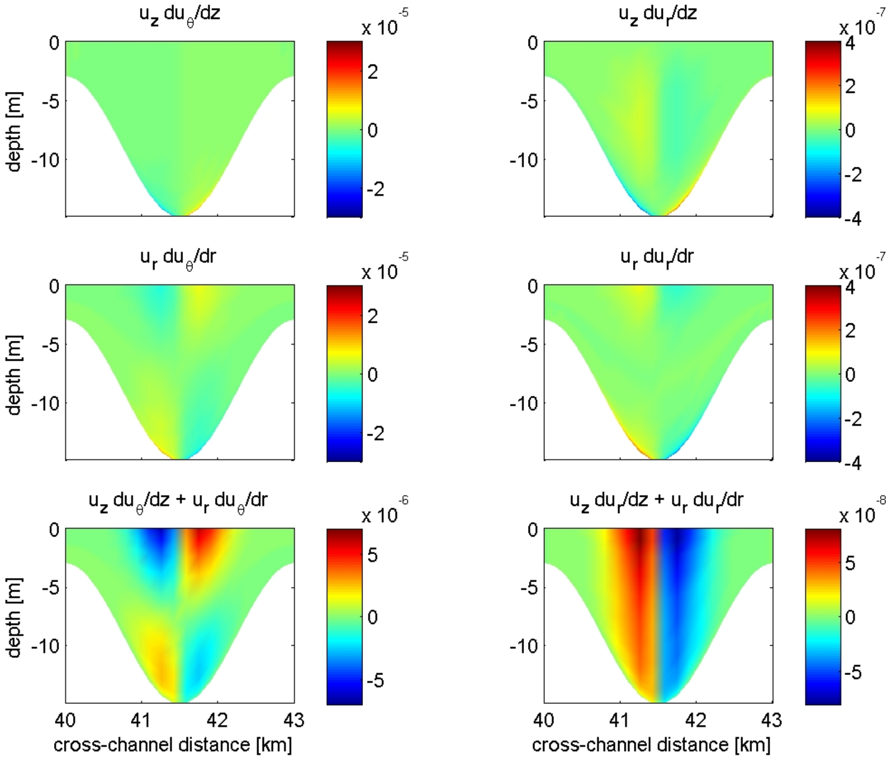


Figure 1. Computed tide-residual advective transfer of momentum (subscripts in the titles of the panels refer to the direction of the concerned flow velocity component: z = vertical, r = transverse, θ = longitudinal).

Although not shown in this abstract, flow patterns obtained with our model are generally similar to those of Huijts et al. (2007). A detailed comparison, including tidal velocity components, is scheduled for the near future. From a rough assessment, however, it appears that there are some notable differences with respect to the importance of advection. Tide-residual advective transfer of momentum as derived from model results (see Figure 1) appears to be most relevant in the central, relatively deep part of the channel. Within that region, the four considered advective terms of the momentum equations reach maximum values in the vicinity of the bottom (upper four panels in Figure 1). This has to do with the comparatively large near-bottom velocity gradients. Huijts et al. (2007) do not encounter such a phenomenon. Most likely, this can be explained by the difference in turbulence closure formulations. Huijts et al. (2007) use a uniformly distributed vertical eddy viscosity, whereas we assume a parabolic variation over the water column. Near the bottom, the eddy viscosity is smaller for the parabolic distribution than in the case of a uniform one.

The total tide-residual advective forcing of the along-channel flow (lower left panel in Figure 1) contains four cells, indicating that $u_r \partial u_\theta / \partial r$ has a stronger effect than $u_z \partial u_\theta / \partial r$. Huijts et al. (2007) report only two cells, indicating just the opposite. This probably has to do also with the difference in turbulence closure formulations. However, further investigation is required to identify involved relevant mechanisms.

The results presented in Figure 1 show also that in a tide-residual sense, advection-related forcing of the flow in transverse direction is, at least in the considered case, some two orders of magnitude smaller than that in lateral direction. This supports the assumption made by Huijts et al. (2007) that for geometries considered here, transverse forcing is small compared to lateral forcing in first order approximation.

The aim of the second diagnostic application is to assess the extent to which the importance of advective momentum transfer is affected by variations in the steepness of the transverse bottom profile. The motivation for this application is given in the introduction. We consider a channel of which this profile contains a relatively steep part in the centre. To focus on the importance of the bottom slope, the flow is driven by a tide-related pressure gradient and earth's rotation only. With the prescribed magnitude of the pressure gradient, a tide-residual along-channel flow velocity of less than 0.01 m $s^{-1}$ is found. Hence, this application concerns low flow conditions, as intended. For this case, we run our model once including advection and once with the presumption that advection is negligible. Tide-residual advective forcing computed from results obtained with both model runs hardly differ (see Figure 2). Complementary to the aforementioned finding of Schramkowski et al. (2007), this indicates that under low flow conditions, advection is relatively unimportant even in the case of a steep bottom.

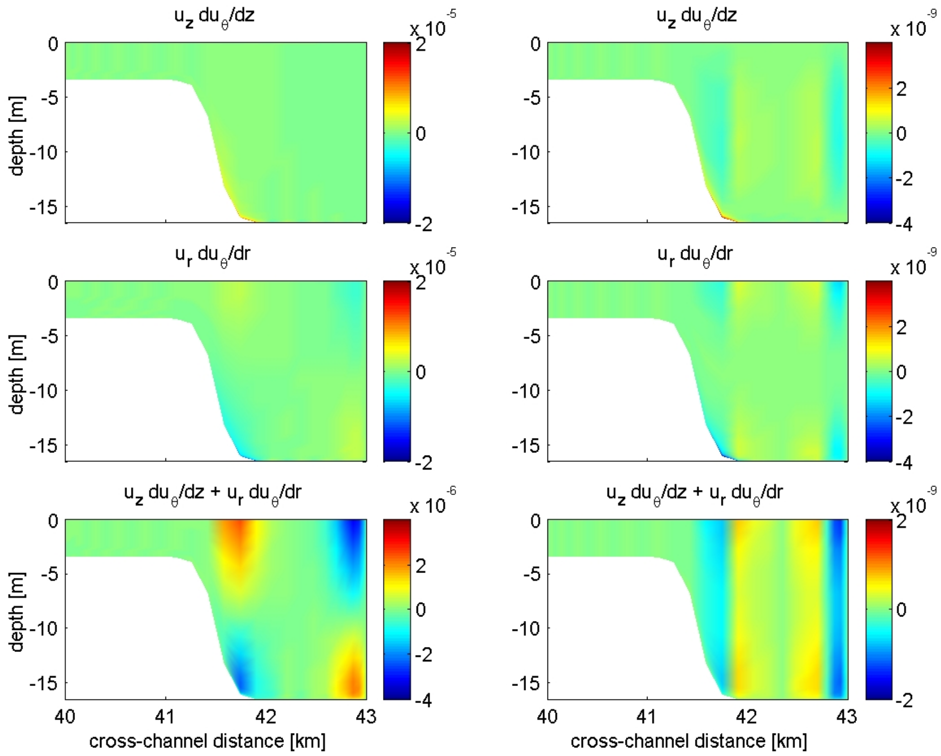


Figure 2. Tide-residual advective transfer of momentum derived from model computations including advection (left hand panels) and corresponding deviations resulting from presuming that advection is negligible in the model computations (right hand panels).

## Envisaged future developments

In this abstract, two diagnostic model applications are outlined as an illustration of our research aim and the potential of the tool we are developing in support of that. Subjects foreseen for the final paper include validation of the model against flow velocities observed in cross-sections of the Satilla River. In addition, observed flow patterns will be analyzed to identify the relative importance of individual physical mechanisms. In this respect, extensive use will be made of field data collected, described and analyzed by Elston (2005). Further research includes also a sensitivity analysis of model results to various eddy viscosity formulations as well as an assessment of the relation between the relative importance of advective momentum transfer on the flow on the one hand and flow conditions and channel geometry on the other.

## References


Boyd, J.P. (2000), *Chebyshev and Fourier spectral methods*. Dover Publications.

Elston, S.A. (2005) *Secondary circulation in a sinuous coastal plane estuary*. Ph.D. Thesis, Georgia Institute of Technology.

Huijts, K.M.H, Schuttelaars, H.M., de Swart, H.E., Friedrichs, C.T. (2007), Analytical study of the transverse distribution of along-channel and transverse residual flows in tidal estuaries, *Continental Shelf Research*, doi:10.1016/j.csr.2007.09.007. (In press.)

Schramkowski, G.P., Huijts, K.M.H, de Swart, H.E., Schuttelaars, H.M. (2007), *A model comparison of flow and lateral sediment trapping in estuaries*. In: River, Coastal and Estuarine Morphodynamics RCEM 2007 (conference proceedings).